Laboratory for Turbulence Research in Aerospace and Combustion

ABS Infill Structures for Enhancing the Performance of Paraffin Fuel Grains in Hybrid Rocket Engines

Keith Lai, Julio Soria, Callum Atkinson

Technical Report: LTRAC-TR 2022.1

Laboratory for Turbulence Research in Aerospace and Combustion
Department of Mechanical and Aerospace Engineering
Monash University
Melbourne, VIC 3800

ABS Infill Structures for Enhancing the Performance of Paraffin Fuel Grains in Hybrid Rocket Engines

Copyright ©2022

by

Keith Lai, Julio Soria, Callum Atkinson

Abstract

An experimental investigation of Hybrid Rocket Engine fuel grains is undertaken to study the impact of ABS gyroid infill structures on the performance of liquefying fuel grains, in particular; chamber pressure, thrust, regression rate, specific impulse, combustion efficiency and thrust coefficients. To facilitate part of this investigation, a new hybrid rocket engine test facility is designed and constructed.

The design of the new facility commences with a system level analysis of the combustion chamber operation conditions, followed by the development of the pneumatics system for the oxidiser feed, ignition system to kick-start the combustion process, control systems for the actuation of valves and instrumentation to measure thrust, chamber pressure, oxidiser mass flow rate and optical imaging of the exhaust plume. With the experimental facility in a functional condition, the focus of this study shifts to the experimental campaign to test the performance of a novel fuel grain design utilising 3D printing technology.

With knowledge of the Kelvin-Helmholtz Instability in the liquid layer inducing discrete wavelengths based on the supplied oxidiser mass flow rate, a unique 3D printed ABS-paraffin fuel grain is developed. At particular oxidiser mass flow rates, the liquid layer wave-like structures produced in paraffin fuel grains exhibit a corresponding wavelengths. The hypothesis behind this design is to amplify the wave-like structures to promote further droplet break-up by matching these wavelengths with the gyroid topology on the surface of the fuel grain. Baseline ABS and paraffin wax fuel grains were tested and the results were then compared against literature and past experiments to both verify the performance of the engine as well as establishing a benchmark to better compare the novel gyroid fuel grain. It was confirmed that paraffin wax exhibits regression rates up to 200% greater than ABS, however consequently, the efficiency fell short of the ABS at lower oxidiser mass fluxes.

The performance of the gyroid fuel grain consistently beat the baseline paraffin wax and demonstrated the highest efficiencies of the three fuel formulations evaluated in this study, achieving 80% combustion efficiency and 240 s of specific impulse. The predicted thrust coefficients also imply that the efficacy of the gyroid fuel grain might theoretically be nearly 1.5 times greater than the values obtained in this study. A closer examination of the gyroid fuel grains after hot fire reveals structures of the paraffin wax at the surface that are similar to wave-like structures in Kelvin-Helmholtz Instabilities (KHIs). The wavelengths are observed to follow the topology of the gyroid structure, with tiny break-up waves at each peak. This was an intriguing result, and the ramifications could imply that the better performance found in the data could be linked to the gyroid structure's improved entrainment and break-up of droplets from the liquid layer. A final observation from solidified paraffin samples after firing showed uniform deposits of carbon, implying passive carbon impregnation, which might potentially replace the need for carbon infusion into the paraffin mixture.

Contents

Copyright Notice **i**

Abstract **iii**

Declaration **v**

Acknowledgements **vii**

List of Figures **xxi**

List of Tables **xxi**

Nomenclature **xxi**

1 Introduction **1**

2 Background **5**

- 2.1 Regression Rate Theory . . . 5
- 2.2 Liquefying Hybrid Theory . . . 7
  - 2.2.1 Entrainment Rate Model . . . 8
  - 2.2.2 Liquid Layer Stability Models . . . 9
  - 2.2.3 Kelvin Helmholtz Instability in liquefying fuels . . . 15
- 2.3 Previous works on paraffin based performance enhancement . . . 17
  - 2.3.1 Paraffin Fuel Mixtures . . . 17
  - 2.3.2 Additively Manufactured Fuel Grains . . . 19
- 2.4 Hybrid Rocket Test Facilities . . . 21
  - 2.4.1 Ignition Systems . . . 21
  - 2.4.2 Thrust Measurements . . . 22
  - 2.4.3 Pressure Measurements . . . 24
  - 2.4.4 Regression Rate Measurement and Inference . . . 24
- 2.5 Chapter Summary . . . 26
  - 2.5.1 Organisation of Present Work . . . 26

3 Design and Development of Hybrid Rocket Engine Test Facility **29**

- 3.1 Design Parameters and Requirements . . . 30
- 3.2 Combustion Chamber . . . 33

3.3 Hybrid Rocket Engine Platform . . . 35
3.4 Ignition System . . . 36
3.5 Pneumatics System . . . 37
3.6 Instrumentation . . . 38
3.7 Data Acquisition . . . 40
3.8 Control Systems . . . 40
3.9 Exhaust Plume Stability . . . 42

4 Methodology **45**
4.1 3D Printed ABS - Paraffin Fuel Grains . . . 45
4.1.1 3D Printed ABS Gyroid Infill Structure . . . 46
4.1.2 Fuel Grain Paraffin Casting . . . 47
4.2 Experimental Campaign . . . 47
4.3 Chemical Equilibrium Analysis: CEA . . . 49
4.3.1 CEA Parameters . . . 49
4.3.1.1 Conservation Equations . . . 49
4.3.1.2 Specific Impulse . . . 49
4.3.1.3 Characteristic Velocity . . . 50
4.3.1.4 Thrust Coefficient . . . 50
4.4 Regression Rate Inference . . . 50
4.5 Performance Parameter Analysis . . . 52
4.5.1 Combustion Efficiency . . . 52
4.5.2 Thrust Coefficient . . . 52

5 Results and Discussion **55**
5.1 Presentation of Results . . . 55
5.1.1 Preliminary CEA Analysis . . . 55
5.1.2 Repeatability of Fuel Grain Manufacture . . . 56
5.2 Repeatability of Hot Fire Tests . . . 57
5.3 Comparison of Measured Performance Metrics . . . 58
5.3.1 Combustion Chamber Pressure . . . 58
5.3.2 Engine Thrust . . . 64
5.3.3 Regression Rate . . . 64
5.4 Comparison of Calculated Performance Metrics . . . 67
5.4.1 Combustion Efficiency . . . 67
5.4.2 Thrust Coefficient . . . 70
5.4.3 Specific Impulse . . . 70
5.5 Post-Hot Fire Fuel Grain Analysis . . . 73
5.6 Summary . . . 76

6 Conclusions **79**

Bibliography **81**

A Alicat Flow Meter Process Overview **81**

B Paraffin Wax Fuel Grain Manufacture Work Instructions **83**

C Fuel Grain Manufacture Data Tables **87**

List of Figures

1.1 Schematic of a typical Hybrid Rocket Engine system. 2
1.2 Boundary layer combustion process diagram (Kanzaki et al., 2015) 3
1.3 Schematic of the liquid layer dynamics on the surface of a liquefying solid fuel grain. (Jens et al., 2014) 4

2.1 Simplified diagram of the variations in regression rate with oxidiser mass flux 7
2.2 Schematic used for the melt layer thickness above liquefying hybrid estimation fuels. Adapted from (Jens et al., 2014) 8
2.3 Various mechanisms for the inception of entrainment. Adapted from (Ishii and Grolmes, 1975) 11
2.4 Amplification rate of a surface disturbance vs. wave number; 0.3 mm thick water film with film Reynolds number of 50, Froude number of 9.458, and regression rate parameter of zero. Here, b equalling to 0 represents the absence of gravity forces. (Karabeyoglu et al., 2002) 13
2.5 Amplification rate of a surface disturbance vs the wave number for different fuels over various film Reynolds numbers. Here, b equalling to 0 represents the absence of gravity forces. (Karabeyoglu et al., 2002) 14
2.6 Schematic of Kelvin-Helmholtz Instability on the surface of a liquefying fuel with a thin liquid layer. As adapted from (Pelletier, 2009) 15
2.7 The influence of fuel viscosity and oxidiser mass flow on KHI frequencies. (Petrarolo et al., 2018) 16
2.8 Longitudinal wavelengths on fuel viscosity and oxidiser mass flow rate.(Petrarolo et al., 2018) 16
2.9 Plain HTPB, plain paraffin, and a 50/50 fuel blend burning in GOX at 1000 psia (6.9 MPa) with equilibrium composition, as assessed by NASA's CEA. (Thomas et al., 2017) . . . 18
2.10 Schematic of paraffin spheres embedded as a non-homogeneous mixture with HTPB. As adapted from (Boronowksy, 2011) 19
2.11 Example of what a fuel grain could look like when 3D printing is employed together with paraffin wax. 20
2.12 Load cell configuration schematic. (a) The perpendicular layout as seen in Brown and Lyndon (2005) and Heydari and Ghadiri (2017) facilities and (b) parallel layout as seen in Bouziane et al. (2018) facility. 23

3.1 Simplified flowchart of the design process of the hybrid rocket engine test facility. Details of each step are provided in the text. Here, I_{sp}, c* and C_F refer to the specific impulse, characteristic velocity and thrust coefficient respectively. CEA refers to Chemical Equilibrium with Applications (McBride, 1994). 31
3.2 Schematic of the Hybrid Rocket Engine Test Facility located in the LTRAC Combustion Lab. 33
3.3 Cross sectional view of the converging graphite nozzle used in the Hybrid Rocket test facility. 35
3.4 Photographed image of the linear bearing platform. Also captured in this image are the radial bearing mounts. 36
3.5 Electric match igniting bundle of steel wool. Depicting the development of the ignition flame that takes place within the port of the fuel grain. 37
3.6 Image taken of the pneumatic system installed on top of the optical table. Pictured (from left to right) is the Alicat Flow Meter, oxidiser solenoid valve, nitrogen purge solenoid valve and accompanying check valves. 38
3.7 Schematic of injector side of the combustion chamber. Housing the injector port, inlet pressure transducer and load cell. 39
3.8 DAQExpress (National Instruments) Virtual Instrument coding diagram. The diagram outlines the process conducted for each test fire in this study. Beginning with ignition, a small delay, oxidiser solenoid actuation and then purge solenoid actuation. 41
3.9 Schematic of the exhaust plume structure depicting the three regions: near field, transition region and far field (Dash and Wolf, 1984) 43
3.10 Exhaust plume structure overlay over exhaust plume image captured in this study. . . . 43
3.11 Exhaust plume frame captures of baseline a ABS fuel grain at $\dot{m}_{ox}$ = 15.3 g/s from t = 7 seconds relative to ignition start at t = 0 seconds. Basic white balance corrections were applied from sample testings prior to static test fire. 44

4.1 (Left): Single gyroid unit cell. (Right): 3D printed gyroid samples at different infill percentages. 46
4.2 Conceptual schematic of the effect of the ABS gyroid infill structure to amplify liquid layer instabilities. 48
4.3 Gyroid wavelengths over a range of infill percentages. 48
4.4 Regression rate vs oxidiser mass flux data for paraffin based fuels. (Karabeyoglu et al., 2003) 51

5.1 Using CEA: (Left) Performance Characteristics vs ABS infill percentage. (Right): Combustion Chamber Properties vs ABS infill percentage. 56
5.2 CT scan of ABS-paraffin fuel grain cross section normal to the axis of the fuel port. The ABS gyroid structure can be seen as lighter compared to the paraffin wax. 57
5.3 Preliminary measurement data of (a) chamber pressure and (b) engine thrust at 15.3 g/cm^2s (@ 7bar oxidiser inlet pressure) and 10.7 g/cm^2s (@ 10bar oxidiser inlet pressure) oxidiser mass fluxes. Note that the pressure fluctuations in the chamber have been windowed to make the variance in the pressure profiles more visible. 59

5.4 Chamber Pressure and Thrust profiles for baseline ABS, Paraffin and Gyroid fuel grains over t_{burn}=10s, where ignition occurs at t=0s. (a) 7.7g/cm^2s @ 5bar oxidiser inlet pressure (b) 10.7g/cm^2s @ 7bar oxidiser inlet pressure (c) 15.3g/cm^2s @ 10bar oxidiser inlet pressure 60
5.5 A single sample from the experimental campaign of a baseline ABS fuel grain pressure and thrust profile at 15.3 g/cm^2s oxidiser mass flux. Highlighting key features present in a large majority of the fuel grains. 61
5.6 Theoretical Prandtl number over varying O/F ratios for a paraffin based fuel. (Eilers and Whitmore, 2008) 62
5.7 Measured average regression rates for baseline ABS, paraffin and gyroid fuel grains over various oxidiser mass fluxes tested. Curve fit expressions for the gyroid fuel grain results in a Marxman regression rate expression of $\dot{r} = 0.488\ {G_0}^{0.69}$. For comparison, regression rate data for ABS (Whitmore et al. (2016) and paraffin wax (Karabeyoglu et al. 2002) are plotted. 65
5.8 Calculated average combustion efficiency for baseline ABS, paraffin wax and gyroid fuel grains across varying oxidiser mass fluxes tested. 67
5.9 Various combustion efficiencies recorded in past literature for paraffin wax, HTPB, HDPE and a selection of enhanced fuel grains over a range of oxidiser mass fluxes (Zilliac et al., 2020) 68
5.10 Calculated average thrust coefficient, for baseline ABS, paraffin wax and gyroid fuel grains across varying oxidiser mass fluxes tested. 70
5.11 Calculated average specific impulse (Isp), for baseline ABS, paraffin wax and gyroid fuel grains across varying oxidiser mass fluxes tested. Referenced against theoretical values obtained through CEA. 71
5.12 Simplified schematic of the flow path of the oxidiser at the aft end for (a) typical fuel grain and (b) the fuel grain shell geometry used in this study. 72
5.13 Cross section cuts of gyroid fuel grains post fire at (a) 7.7 g/cm^2s , (b) 10.7 g/cm^2s and (c) 15.3 g/cm^2s oxidiser mass flux. The images are orientated such that the oxidiser flow is from left to right. 74
5.14 Close up capture of a 28% gyroid fuel grain after a 10 second, 10.7 g/cm^2s oxidiser mass flux hot fire. Outlined in yellow is a simplified sketch of the paraffin profile. The blackened paraffin layer and the break-up at the wave peak are also highlighted in the figure. 75
5.15 Hardened paraffin wax sample post gyroid fuel grain hot fire. 75

B.1 Image taken of the break-down of paraffin wax slabs in process to achieve smaller more easier to melt portions of wax. 83
B.2 Water bath preheating stage. The equipment is started prior to use up to 80 degrees Celsius. An important note is to ensure the lid remains enclosed to speed up the rate of heating. 84
B.3 CAD render of the overflow jig used to accommodate paraffin settlement and shrinkage during the casting and cooling process respectively. 85
B.4 Image of the paraffin wax heating process. The step utilised the water bath to reach the set temperature needed to melt paraffin. Depicted is the paraffin in its molten state. . . 85

B.5 The cardboard box provides a barrier to shield the fuel grains from the surrounding elements as they cool. The slots on the top of the box is used to help keep the fuel grains standing vertical as they cool. 86

List of Tables

2.1 Regression rate parameters for various oxygen and fuel combinations, with listed references . . . 6

3.1 Regression rate parameters for various oxygen and fuel combinations, with listed references . . . 30

5.1 Table of fuel grain manufacturing data comprising a sample of each fuel grain tested to show initial mass measured and the deviation from the average for that fuel grain formulation. A complete table of data can be found in Appendix C. . . . 57

C.1 Complete register of initial and final mass and fuel mass flow rate data for all tested experimental campaign fuel grains. . . . 87

Nomenclature

Abbreviations

CEA	Chemical Equilibrium with Applications
HRE	Hybrid Rocket Engine
LRE	Liquid Rocket Engine
O/F	Oxidiser to Fuel ratio
SRM	Solid Rocket

Greek symbols

δ	Boundary Layer Thickness
η	Efficiency
κ	Diffusivity
μ	Viscosity
ρ	Density
σ	Surface Tension

Roman symbols

$\dot{m}$	Mass Flow Rate
$\dot{Q}$	Heat Transfer Rate
$\dot{r}$	Regression Rate
A	Area
B	Blocking Factor
C	Specific Heat
$c*$	Characteristic Velocity
C_F	Thrust Coefficient
C_f	Skin Friction Coefficient
C_H	Stanton Number
D	Diameter
e	Emissivity
F	Thrust
G	Mass Flux
H	Liquid Layer Thickness
h	Enthalpy
h_v	Latent Heat of Combustion
I_{sp}	Specific Impulse

L	Length
M	Mach Number
P	Pressure
Re	Reynolds Number
T	Temperature
u	Streamwise Velocity
v	Vertical Velocity
x	Local Axial Position

Subscripts

c	Convection
e	Boundary Layer Edge
ent	Entrainment
l	Liquid
r	Radiation
s	Solid
t	Throat
v	Vaporisation
w	Wall Surface

Chapter 1

Introduction

In this thesis, we will be exploring the impact of ABS gyroid infill strucutres on the performance of liquefying fuels in Hybrid Rocket Engine's (HREs) through the use of additive manufacturing technologies. Chemical propulsion systems, which are typically Liquid Rocket Engines (LREs), Solid Rocket Motors (SRMs) and the earlier mentioned Hybrid Rocket Engine, typically operate under the same principles - where stored propellants convert their chemical energy into thermal energy within a combustion chamber, which in turn is converted to kinetic energy as the heated products from combustion are expelled through a nozzle to accelerate the gas.

Solid rocket engines use a mixture of tightly packed solid fuels and oxidisers stored inside their combustion chamber. The combustion process is governed by the pressure and temperature produced by the two reacting propellants, once ignited, the flame burned continuously and is difficult to extinguish mid-burn. Solid rocket engines can typically not be throttled; however, they boast mechanical simplicity to achieve a single maneuver to a required ΔV since they do not require any auxiliary systems, such as turbo-machinery, to deliver the propellant or the oxidiser - the only system required is ignition. They have high density but have lower combustion efficiencies and require more oxidiser and fuel to match the performance seen with LREs and HREs. Typically, these engines act as boosters or, in some cases, the upper stage if a sizeable single burn is required.

The other notable class of chemical propulsion systems are liquid rocket engines. Liquid rocket engines separately store the fuel and oxidiser in their liquid state. They are stored in tanks and then compressed via gas compressors or are pressure fed by a high pressure inert gas, such as Nitrogen (N_2), vaporising the propellant before entering the combustion chamber. This method allows for higher chamber pressures to be reached and ultimately allowing for greater performance, however, at the cost of complexity, cost and safety since there are more components running at high pressures and increasing the risk if a failure was to occur. Since the propellants are fed separately into the combustion chamber, the mass flow of propellants can be throttled and re-started. It is not uncommon to see in-space missions which require multiple re-starts.

Monopropellant thrusters use catalyst beds to decompose a single propellant, such as hydrazine. Most monopropellant thrusters comprise a fuel tank with a container (or device to manage surface

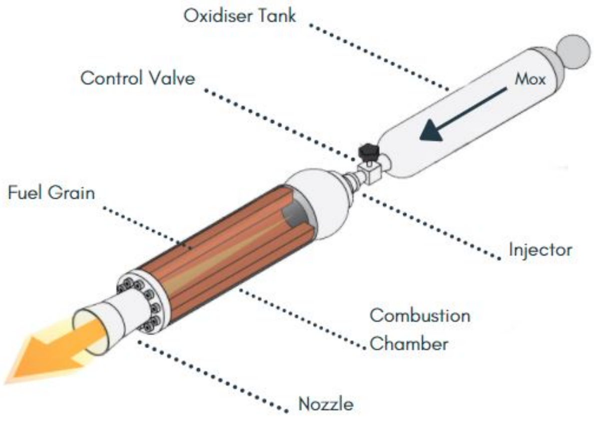

Figure 1.1: Schematic of a typical Hybrid Rocket Engine system.

tension) filled with fuel. The fuel is led into the decomposition chamber and controlled via a poppet valve. This class of propulsion system can be seen mainly in satellite or payloads for small maneuvers and attitude control. Despite performing below the other systems mentioned earlier and thus not typically suitable for large rocket boosters, they have a significant legacy for being easily stored and reliable for in-space propulsion (De Luca et al., 2017) .

Hybrid rocket engines contain features of both LREs and SRMs - where the fuel and oxidiser are in different phases and stored separately, like that of a LRE, but the fuel is of solid state, like that of a SRM. The standard hybrid rocket engine utilises a solid fuel grain installed within the combustion chamber with either a liquid or gaseous oxidiser stored in a tank upstream (figure 1.1). The oxidiser's configuration depends on the type of chemical used; some engines utilise self pressurising oxidisers, such as nitrous oxide (N_20), eliminating the need for an external pressurisation system (Dyer et al., 2007) , whereas others may require a pressurised inert gas to help inject the oxidiser at sufficient pressures. The combustion process itself is what sets the hybrid apart from liquids, solids and mono-propellants - commonly known as boundary layer combustion. The mechanism will be discussed in greater detail later in this chapter, but in essence, it can be described as a diffusive flame developed inside the boundary layer generated from the flow of gaseous oxidiser over the burning solid fuel surface (figure 1.2). Heat is delivered from the flame zone to the free stream and to the fuel grain surface through convection and radiation. Convection will be the primary mode of heat transmission and the heat generated vaporises and convects back to the flame zone. At the same time, turbulent diffusion transports oxidizer from the free stream to the flame zone. The rate of reaction, chamber pressure, and chamber temperature all play a role in determining the thickness of the flame area and its placement in the boundary layer. Unfortunately, this boundary layer combustion characteristic is what is currently limiting the performance of hybrid rocket engines - since, in many configurations, the mixing of reactants through the diffusion flame is unable to match the performance seen with LREs.

In hybrid rocket engines, the mass flow of fuel ($\dot{m}_f$), is determined by the rate at which the surface of the solid fuel transfers its mass into the core oxidiser flow to be combusted. This transfer of mass regresses the surface of the fuel and in turn, increasing the diameter of the fuel port. This rate of regression, commonly referred to as the regression rate ($\dot{r}$), is paramount to the performance of a HRE.

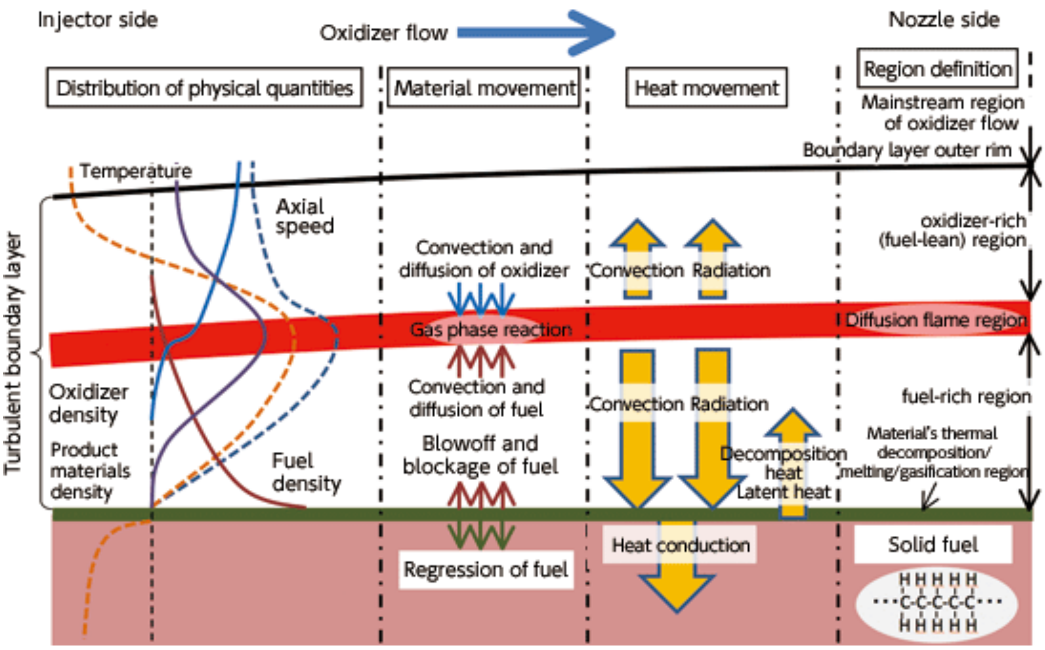
Injector side
Oxidizer flow
Nozzle side
Distribution of physical quantities
Material movement
Heat movement
Region definition
Mainstream region of oxidizer flow
Boundary layer outer rim
Temperature
Axial speed
Convection and diffusion of oxidizer
Convection
Radiation
oxidizer-rich (fuel-lean) region
Turbulent boundary layer
Gas phase reaction
Diffusion flame region
Oxidizer density
Convection and diffusion of fuel
Convection
Radiation
fuel-rich region
Product materials density
Fuel density
Blowoff and blockage of fuel
Decomposition heat
Latent heat
Material's thermal decomposition/ melting/gasification region
Heat conduction
Regression of fuel
Solid fuel
H H H H H
···C-C-C-C-C···
H H H H H

Figure 1.2: Boundary layer combustion process diagram (Kanzaki et al., 2015)

Performance difficulties resulting from slow-burning, low regression rate fuels have hampered the adoption of hybrid motors for applications demanding substantial thrust. When the surface of the fuel ablates, such that there exists a vertical flow from the surface that expands the boundary layer, it increases the thickness of boundary layer and as a result, reduces the shear stress and heat flux to the surface. This effect is known as the blowing effect, and it restricts and inhibits the combustion of traditional hybrid fuels (this will be explored in greater detail later in this thesis). Fortunately, there is a family of fuels that have been shown to achieve high regression rates using normal alkane hydrocarbons, such as paraffin wax (Karabeyoglu et al., 2001) . These fuels, also known as liquefying fuels, have demonstrated regression rates of approximately 3-4 times that of more conventional solid fuel grains via the presence of a thin liquid layer at the surface of the burning fuel grain - exhibiting an entrainment effect of droplets through the diffusion flame (figure 1.3).

The introduction of liquefying fuels have opened up a new area of research for HREs, however, in doing so, raises more questions to fully understand the entrainment mechanism, as we have yet to see a reliable liquefying fuel based hybrid rocket engine used in commercial space. This can largely be attributed to the discovery still being in its relative infancy, when compared to the length of research dedicated to the more traditional HRE solid fuels. Although the entrainment of droplets can sufficiently increase the regression rate, it is also important to ensure that the droplets are fully vaporised and adding energy into the system, otherwise, the fuel is simply leaving the nozzle before it reacts. So a key area of focus for liquefying fuels is to improve our understanding and how we can ensure complete vaporisation of the droplets. This has resulted in researchers conducting visualisation experiments (Jens et al., 2014) and establishing a connection between the mass flow of oxidiser and the wave-like dynamics of the liquid layer to the Kelvin-Helmholtz Instability (KHI) (Petrarolo et al., 2018) . Given than the liquid layer can be characterised by particular wavelengths at specific oxidiser mass flow rates, it is hypothesized that by exciting these wavelengths, we can see an increase to the rate of droplet entrainment, but also improving the vaporisation by breaking them down into smaller drops.

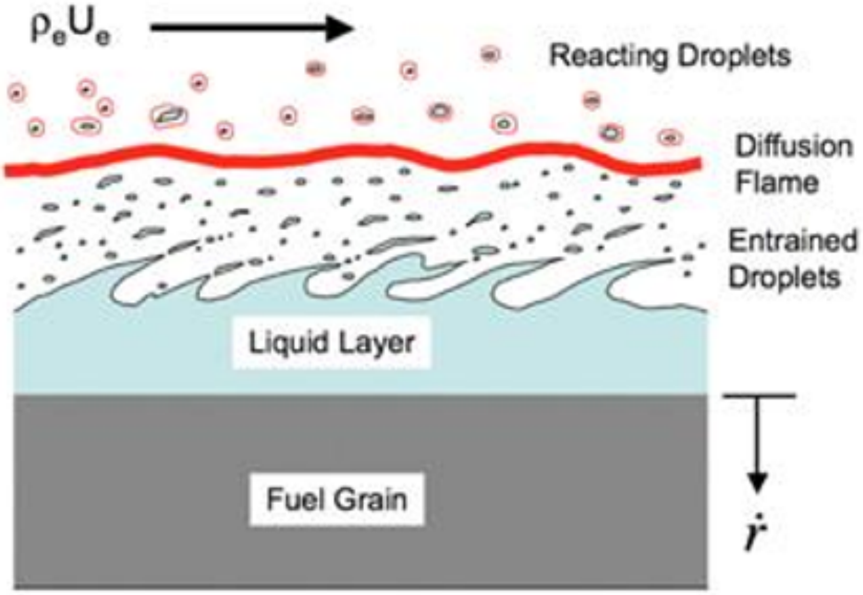

Figure 1.3: Schematic of the liquid layer dynamics on the surface of a liquefying solid fuel grain. (Jens et al., 2014)

A possible method to achieve this, could be via the surface topology of the fuel grain itself.

This thesis presents an experimental investigation of hybrid rocket engine fuels, with an aim to examine the performance of liquefying fuel grains with the introduction of surface topology via the use of embedded structures in the fuel grain. The first half of this thesis provides a more detailed discussion of the relevant elements of hybrid rocket combustion theory, liquefying fuel and entrainment models is presented in the next chapter (Chapter 2), along with an introduction to lab scale hybrid rocket engine design. Chapter 3 then discusses the design and commission of a hybrid rocket engine test facility in which the experimental campaign of this study is conducted. Given the time and financial expenditure on this sort of facility, the design considers the use of the test facility to include future use cases as well. Chapter 3 outlines the operational requirements of the test facility, including the range of operational oxidiser pressures and system level designs for control, pneumatics, ignition and instrumentation. Once the system is established, the commission and validation of the hybrid rocket engine test facility are discussed at various points throughout Chapter 3.

With the facility complete, an experimental campaign is conducted to investigate the performance of baseline non-liquefying and liquefying fuel grains. This establishes a benchmark to examine the relative performance of the novel, 3D printed fuel grain, designed and developed in this study. The experimental conditions along with the measurement and analytical techniques used in this study are then outlined in Chapter 4. The results from the experimental campaign are then presented and discussed in Chapter 5, focusing on the results of baseline fuels and how it compares to existing literature, before delving deeper into their comparison to the novel fuel grain. The novel fuel grain is then analysed post hot fire by cross sectional cuts to gain more insight into how the surface topology affected the liquid layer.

Chapter 2

Background

This chapter explores the theoretical foundations behind the boundary layer combustion process present in hybrid rocket propulsion systems. The previous chapter eluded to the primary limitation of hybrid rocket engines: the low fuel regression rates - limiting the potential for higher thrust levels necessary for large-scale commercial space applications. Here, we will build upon why this limitation is present in traditional hybrid rocket fuels and how discovering liquefying fuels has significantly improved regression rates. Liquefying fuels exhibit higher regression rates through the entrainment of droplets from the liquid layer; however, it is the instability of this liquid layer that leads to entrainment. Models have been developed to explain this, however limitations are still present. This chapter will explain the basis of these models and explore the areas that remain poorly understood.

2.1 Regression Rate Theory

Regression rate is a vital parameter when it comes to designing and characterising a hybrid rocket engine. Hybrid rocket fuels burn via a combustion process that results in the vaporisation, sublimation and pyrolisation of the fuel. This takes place at the turbulent diffusion flame, as mentioned in Chapter 1, within the boundary layer produced by the gaseous oxidiser flowing over the solid fuel surface. The boundary layer is divided into two zones: one above the flame, where the temperature and velocity gradients are in opposite directions, and one below the flame, where they are in the same direction. The boundary layer for momentum transfer is formed by both zones working together to transmit heat to the wall. The rate in which the solid fuel (or solid oxidiser) is transported from the solid surface and into the core flow, typically known as the regression rate, is proportional to the heat flow from the flame to the solid surface wall (Chiaverini, 2007) . The formulation of a hybrid combustion theory needs consideration of the process of heat transfer from the flame to the wall and the mass flow from the fuel to the flame.

We begin by describing the model for boundary layer combustion, to which our understanding of liquefying fuel grains is built from as well as our understanding of what limits high regression rates in traditional hybrid rocket systems. Quasi-steady conditions and negligible heat flux through radiation and conduction, i.e. assuming pure convection, are core assumptions that pertains to the basic model for hybrid rocket fuel regression rates. The most commonly used expression to model the regression rate for typical hybrid rocket fuels is can be found in Equation 2.1 (Marxman, 1965).

$$\dot{r} = aG_{ox}{}^{n} \tag{2.1}$$

Here, the regression rate ($\dot{r}$) is expressed as a function of oxidiser mass flux (G_{ox}), where the coefficients a and n are typically evaluated experimentally through combustion tests. The coefficients a and n are used to simplify the more complex expression, taking into account the density of fuel (ρ_f), the viscosity of the fuel (μ_f), the blowing effect (B) and averaged across the length of the fuel grain (this includes the assumption that the regression rate is uniform along the solid grain length). The blowing effect, sometimes also referred to as the "blocking effect", is a phenomena originating from the continuous addition of fuel mass from the solid fuel surface under vaporisation. Blowing changes the velocity profile and shear stresses in the vertical flow from the surface, expanding the boundary layer and increasing its thickness (Humble and Altman, 1995) . As a result, this reduces the velocity gradients in the boundary layer, and further reduces shear stress and heat flux to the fuel surface. The blowing parameter B is introduced to characterise the flow across a blowing surface, and such is the case for a regressing fuel grain surface undergoing diffusion. The consideration of the blocking effect is one of the most significant factors hindering the regression rate for typical solid fuels. Table 2.1 lists the Marxman model coefficients found from experimental tests for various solid fuel grains.

Fuel	a_0	n	Ref.
Paraffin	1.17*10^{-4}	0.62	(Karabeyoglu et al., 2001)
PE Wax	4.31*10^{-5}	0.71	(Karabeyoglu et al., 2005)
HTPB	3.04*10^{-5}	0.68	(Karabeyoglu et al., 2001)
HDPE	2.34*10^{-5}	0.62	(Karabeyoglu et al., 2001)
PMMA	2.11*10^{-5}	0.62	(Zilliac and Karabeyoglu, 2006)
ABS	5.05*10^{-5}	0.22	(Whitmore and Merkley, 2019)

Table 2.1: Regression rate parameters for various oxygen and fuel combinations, with listed references

For most practical applications, the regression rate is considered to not depended on pressure, as the chemical reaction rate of the propellants during combustion is significantly greater than the mixing rate of the reactants in the turbulent flame (Petrarolo et al., 2019). However, the Marxman model begins to diverge from experimental results at lower and higher mass fluxes, where a dependency of regression rate on the chamber pressure has been observed (Jens et al., 2014). At the lower end of mass fluxes, the influence of radiative heat flux increases because the turbulent convection component of the total heat flux to the wall is minimal, meaning heat flux due to radiation cannot be neglected, therefore violating the assumptions pertaining to Marxman's regression rate model. In this mass flux regime, the regression rate is seen to decrease as chamber pressure decreases. At the higher end of mass fluxes, the effect of chemical kinetics becomes more important since the residence time of the gases is reduced, where in the case of hybrid combustion, the residence time is the average time it takes for the propellant molecules to vaporise. In this regime, the regression rate is seen to increase at higher

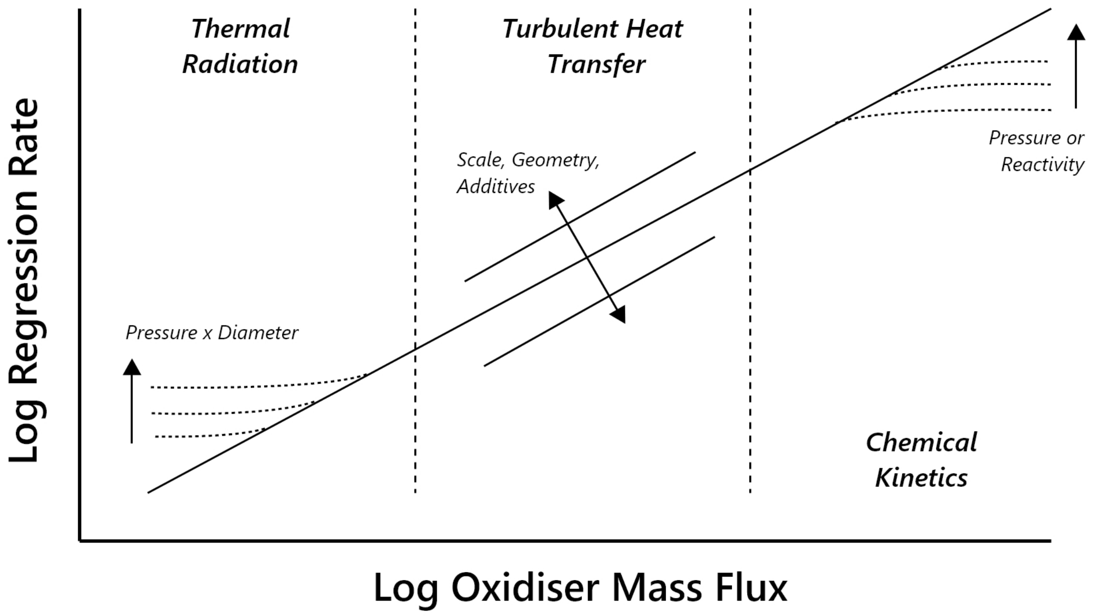

Figure 2.1: Simplified diagram of the variations in regression rate with oxidiser mass flux

chamber pressures. At the intermediate mass flux regime, the regression rate is dominated by turbulent heat flux and shows a power dependence on the oxidiser mass flux as predicted by Marxman's model (Equation 2.1), here radiation nor chemical kinetics significantly influences the behaviour of regression rate with respect to oxidiser mass flux. Figure 2.1 graphically summarises the dependency of the regression rate on the parameters discussed at each mass flux regime.

2.2 Liquefying Hybrid Theory

The accuracy of Marxman's model begins to fall for fuels other than polymeric fuels such as HTPB. From previous studies, these types of fuels show low regressions rates due to the characteristic of the diffusion flame and the presence of the blowing effect (Whitmore et al., 2016). In order to increase the regression rate for hybrid propulsion systems, one particularly effective method was through the use of liquefying fuel grains. These fuel grains are characterised by their trait of melting prior to vaporisation and when in its liquid state, it exhibits low viscosity and low surface tension. When these fuels are used as fuels in HREs, they form a thin liquid layer at the surface of the fuel (Karabeyoglu et al., 2002). This thin liquid layer becomes unstable within the boundary layer from the flow oxidiser over the solid surface. When unstable, liquid droplets are sheared off the liquid layer and these droplets are then entrained into the core oxidiser flow and through the diffusion flame where it vaporises and adds energy into the system, the rate at which the fuel grain transfers these droplets is known as the entrainment rate. This mechanism can often be described as a spray injection of fuel along the axial port length of the fuel grain, increasing the effective burning area and reducing the effect of blocking on the regression rate (Karabeyoglu et al., 2002). A schematic of this has been presented in Figure 1.3 in Chapter 1.

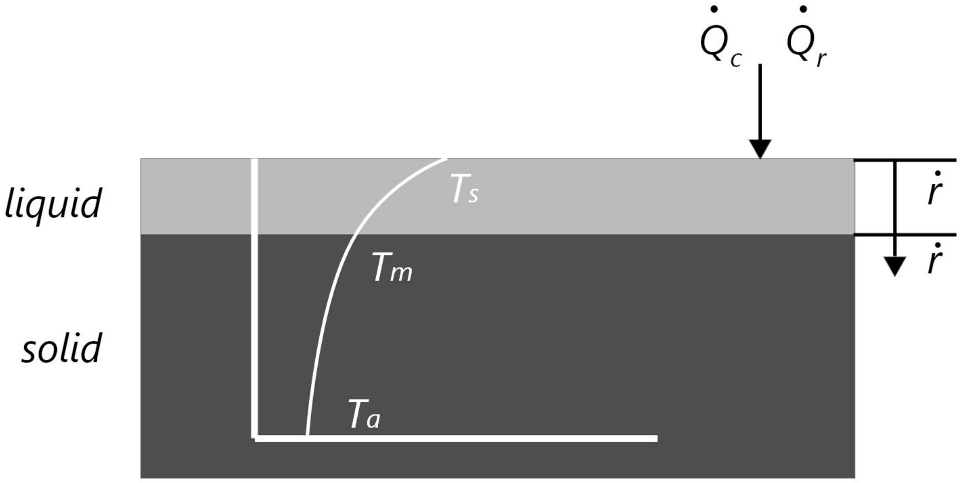

Figure 2.2: Schematic used for the melt layer thickness above liquefying hybrid estimation fuels. Adapted from (Jens et al., 2014)

Typically, fuels that exhibit this type of behaviour under combustion are non-polymerised substances that melt and liquefy when heated. Fuels that fit this category comprise of solid cryogenic fuels, such as frozen pentane, and waxes, such as paraffin and PE wax. The use of frozen liquefying fuels typically require considerable effort and add complications in the design of the HRE and is less used for most practical applications. Wax based fuels, however, have demonstrated the same type of behaviour, while boasting ease of manufacture, storability and have shown high entrainment rates from experimental studies (Karabeyoglu et al., 2001). In this thesis, we will be focusing on the application of paraffin wax as the baseline liquefying fuel for analysis and comparison.

2.2.1 Entrainment Rate Model

The model for the entrainment rate is conceived as an extension of Marxman's theory for classic non-liquefying fuel grains. Karebeyoglu et al. (2002) consider the convective and radiative heat transfer from the solid and liquid phases together in their model (Figure 2.2).

In their model, steady state regression of the fuel is assumed. The velocity profile of the solid-liquid and gas-liquid interfaces are assumed to be constant and equal - leading to the assumption of uniform and constant liquid layer thickness. The effect of convection is ignored in the liquid layer, as the layer thickness is considered to be small, with large temperature gradients and low Reynolds numbers. The fuel in both the liquid and solid states are assumed to act as grey bodies, where the coefficient of absorption is independent of the impinging radiation frequency. The thermo-physical properties of the liquefying fuel is assumed to be uniform in both liquid and solid states. Karabeyoglu et al. (2002) delve deeper into the derivation of their model and taking into account the results from experiments and theory, they have suggested the following expression (Equation 2.2) for the entrainment rate in relevant terms to the properties of interest in a HRE.

$$\dot{m}_{ent} \approx \left(\frac{{P_d}^{\delta} h^{\theta}}{{\mu_l}^{\gamma} \sigma^{\pi}} \right) \tag{2.2}$$

Where P_d is the dynamic pressure within the chamber, h is the liquid layer thickness, μ_l is the viscosity of the liquid layer and σ is the surface tension.

Subscripts $\delta, \theta, \gamma, \pi$ are all experimental parameters.

The expression shows that the rate of entrainment increases with lower viscosity and surface tension. The higher the chamber pressure and the greater the liquid layer thickness will also see an increase in the mass flow rate of fuel from entrainment. The expression aids in understanding what effects the entrainment rate and to help determine potential candidates for the selection of liquefying fuel grains.

It is important to note that the total regression rate for liquefying fuels does not only comprise of the entrainment rate. Gater and L'Ecuyer (1970) have experimentally determined that the total regression rate of a liquid layer over a solid surface can be written as the sum of the rate of entrainment $\dot{r}_{ent}$, which is generated from the physical mass transfer of fuel from the liquid layer to the core oxidiser flow, and the vaporisation rate $\dot{r}_v$, which is caused by the vaporisation of the liquid through the diffusion flame (Equation 2.3).

$$\dot{r} = \dot{r}_v + \dot{r}_{ent} \tag{2.3}$$

Gater and L'Ecuyer (1970) determined that the regression rate of a liquid layer over a solid surface is dominated by the entrainment rate, where higher total regression rates were seen when the rate of droplet entrainment was greater. In their investigation, it was discovered that the surface of the liquid layer exhibited ripples which increased its effective surface roughness. Increasing levels of surface roughness was seen to correlate with increase vaporisation regression rates. It was suggested that when the vaporisation of the fuel is of importance, then increasing surface roughness should be the focus. Ultimately, for the use case in HREs, both vaporisation and entrainment should be considered (Gater and L'Ecuyer, 1970).

2.2.2 Liquid Layer Stability Models

As mentioned at the beginning of this chapter, the primary mechanism behind the improvement in regression rate with liquefying fuels is the instability and consequent entrainment of droplets. Prior to investigations in the stability of the liquid layer for liquefying hybrid fuels, there have been several studies (Gater and L'Ecuyer, 1970; Ishii and Grolmes, 1975; Craik, 1966; Tanner, 1980) that focused on thin liquid films over a solid surface, primarily with regards to film cooling applications. Ishii and Grolmes (1975) and Gater and L'Ecuyer (1970) have focused on droplet entrainment - where findings for to essential parameters to the regression rate of a liquefying fuel - the inception of entrainment (Ishii and Grolmes, 1975) and the correlation between entrainment and vaporisation (Gater ad L'Ecuyer, 1970) .

Ishii and Gromles (1975) conducted a series of experiments to observe the onset of entrainment visually, whereby a gas flow was imparted onto a thin liquid layer to produce a wavy liquid film - where it was found to entrain in various ways. The motion and deformation of wave crests are governed by hydrodynamic and surface tension forces. These forces cause significant distortion at the gas-liquid interface under certain conditions, resulting in the fragmentation of a section of the liquid wave into numerous droplets. The forces acting on the wave crests are determined by both the flow pattern and the form of the interface. According to the Bernoulli theorem, higher gas velocity results in lower pressure at the wave crest, while lower gas velocity results in higher gas pressure at the wave trough. When the film is unstable, the dominating waves that arise have the highest growth factor. The waves become irregular and three-dimensional as the relative velocity increases (van Rossum, 1959; Hanratty and Hershman, 1961). At sufficiently high wave amplitude and gas velocity, these dynamic capillary waves can transform into large-amplitude kinematic waves that propagate in only one direction (Lighthill and Whitham, 1955). The manner in which these larger waves then break-up into smaller droplets can be governed by five fundamental types of entrainment processes (Ishii and Grolmes, 1975) indicated in figure 2.3 are:

1. Roll Waves. The tops of big amplitude roll waves are sheared off from the wave crests, which has been observed in experiments (Brodkey, 1967; van Rossum, 1959) . Against the holding force of the liquid surface tension, the drag force acting on the wave tops deforms the interface to produce droplets.

2. Wave Undercut. This occurs when a gas flow undercuts the liquid film. Although the inception of this particular type of entrainment is still not fully understood - based on visual observations, it occurs when the kinematic waves cause sharp undercuts to the wave in front, elongating a neck in the wave to a point where it breaks up into small droplets (Hewitt and Hall-Taylor, 1970).

3. Bubble Burst. This type is typically associated with gas bubbles exploding. Newitt et al. (1954) demonstrated that a bubble rising to the surface of a liquid can generate drops. A thin liquid layer forms at the top of the bubble when it reaches the interface, separating it from the gas flow. The film finally ruptures in multiple locations as the liquid is drained from it, resulting in entrained small droplets. The action of the surrounding liquid filling the crater produced by the bursting of bubbles can produce even larger drops. A spike-like filament rises from the crater's core and disintegrates into droplets. Gas injection, turbulent wavy motions, or nucleation can cause bubbles to form in a liquid film.

4. Liquid Impingement. This mechanism may produce tiny droplets when roll-wave fronts advance as a result of the impingement of larger liquid droplets or mass to the film interface.

5. Liquid Bulge Disintegration. The final category to address is the entrainment that occurs as a result of flooding. When the counter-current flow approaches the flooding state, large-amplitude waves can be separated from the film, forming a bulge or a liquid bridge between the walls due to film instability. Hinze (1955), Sevik and Park (1973) and Sleicher (1972) compared the production of liquid mass in a high-velocity gas core flow to the experimental situation of droplet disintegration in a gas stream. As a result of the mechanics explained by Hinze, it is envisaged that these liquid bulges and bridges will eventually dissolve into many droplets (Hinze, 1955) .

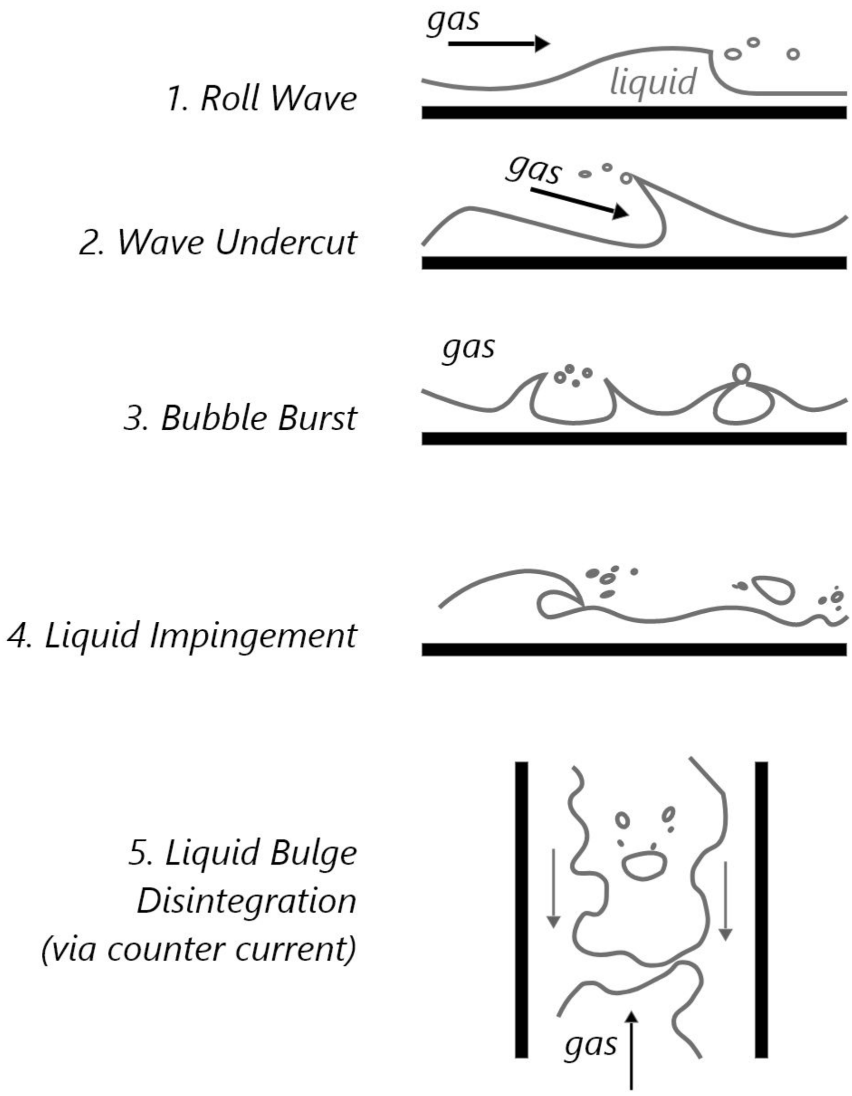
gas
liquid
1. Roll Wave
gas
2. Wave Undercut
gas
3. Bubble Burst
4. Liquid Impingement
5. Liquid Bulge
Disintegration
(via counter current)
gas

Figure 2.3: Various mechanisms for the inception of entrainment. Adapted from (Ishii and Grolmes, 1975)

Summarising Ishii and Grolmes findings, it was observed that in rough turbulent Reynolds number regimes, the onset of entrainment criterion is given by one based on the roll-wave mechanism and can be applied irrespective of flow direction. In the transitional roughness regime of Reynolds numbers, the criteria can be expressed by the shearing off of roll-wave crests. At the lower end of the Reynolds numbers, the mechanism for entrainment shifts to one that exhibits wave-undercutting. We can use these observations to understand the types of entrainment mechanisms we might see under particular Reynolds numbers.

During the same period of time, Gater and L'Ecuyer (1970) conducted an experimental investigation on the phenomena that characterise liquid film cooling - here, they describe the nature of mass transfer from a liquid layer as having both an entrainment and evaporation component as described in equation 2.31.

A series of experiments were conducted, and the behaviour of thin-film layers over a surface was captured visually over a range of different pressures via the injection of liquid onto the wall of the test section. The primary conclusions made in this study that aid in our understanding of entrainment for liquefying fuels are:

- The amplitude of interfacial waves is determined by the gas flow's dynamic pressure, P, with the scale of waves decreasing as the dynamic pressure rises.
- Entrainment accounts for the bulk of mass transfer in the case where the liquid layer is thin relative to the area of the core flow.
- The entrainment rate is a function of liquid injection (which in the case of hybrids, can be related to the thickness of the liquid layer), the dynamic pressure, and the surface tension, σ. Where the regression rate is proportional to the pressure over the surface tension of the liquid, i.e. as pressure increases and surface tension is minimised, we can observe greater regression rates.
- In cases where evaporation is important, the interface surface area of the liquid film was seen to increase the evaporative mass transfer rate considerably.

Now, to apply this to hybrid systems, part two of Karabeyoglu's liquefying propellant theory describes a model for the stability of the liquid film layer. The primary assumption here is that for hybrid applications, the Reynolds number of the liquid layer (equation 2.12) is defined with respect to the liquid layer thickness being estimated to be less than 300. Therefore, it is assumed that the liquid layer flow is laminar in nature and that fluid properties across the thickness of the layer do not vary. A hybrid engine's film stability model must account for liquid generation and injection at the solid interface and liquid removal at the gas interface. The removal rate must equal the injection rate during a steady-state operation with a constant film thickness. The liquid layer equations with respect to the rocket frame of reference do not have a steady-state component even in this simple state of operation. The problem must be formulated in a frame of reference that is fixed to the moving interfaces, which are translated at a constant speed with respect to the rocket frame, in order to simplify the analysis. The complete derivation can be found in part two of Karabeyoglu's liquefying propellant theory (Karabeyoglu et al., 2002) .

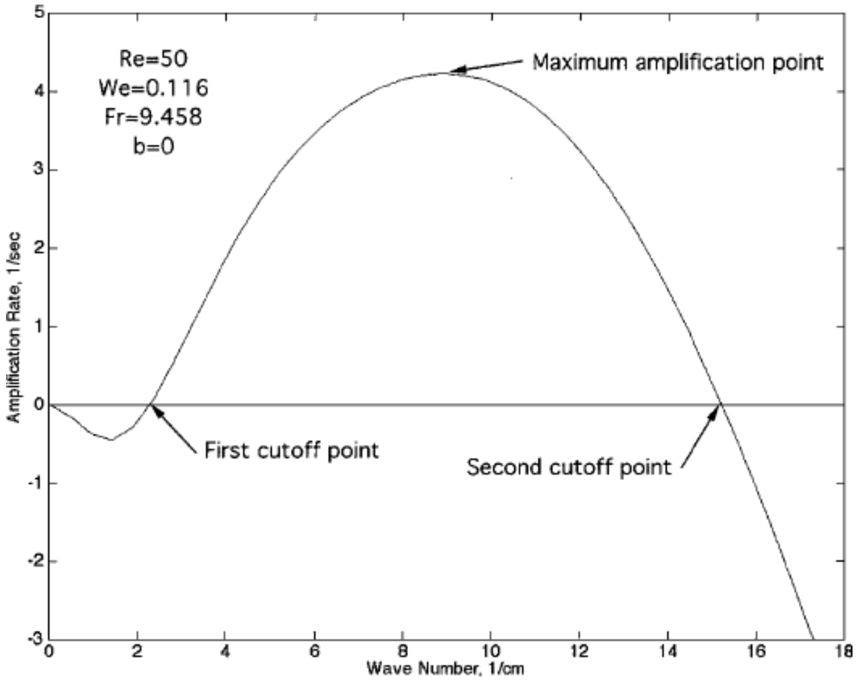

Figure 2.4: Amplification rate of a surface disturbance vs. wave number; 0.3 mm thick water film with film Reynolds number of 50, Froude number of 9.458, and regression rate parameter of zero. Here, b equalling to 0 represents the absence of gravity forces. (Karabeyoglu et al., 2002)

One of the findings from the literature that is particularly relevant to this study is that there is a finite range of amplified wave numbers for thin film thicknesses, implying that the layer is unstable over a finite range of wave numbers. The amplification rate can be expressed in the terms of a non-dimensional amplification rate:

$$-Im(\beta_d) = -Im(c\alpha Re)\left(\frac{\mu_l}{h^2\rho_l}\right) \tag{2.4}$$

In this expression, β_d is the non-dimensional amplification parameter, α is the non-dimensional wave number, c is used to express β/α, h is the melt layer thickness, μ_l is the viscosity of the liquid layer, and ρ_l is the density of the liquid layer.

Between these two cut-off wave numbers seen in Figure 2.4, the amplification reaches its greatest value. The matching wavelength is assumed to be the observed size of the disturbance in the actual flow system, as this is the most amplified wave number. The initial cut-off point approaches zero as the body force decreases. Craik (1966) was one of the first to find instabilities of this type in thin water films in a wind tunnel and distinguished them as slow waves. The interplay of gas-phase shear stresses acting on the liquid surface with the slope of the liquid layer surface produces these. Figure 2.5 depicts a typical form of the interface disturbance's dimensional amplification rate, -$Im(\beta_d)$, as a function of the dimensional wave number k determined for a thin film of water.

Intuitively, the amplification rate of the disturbances is an essential parameter that ties the linear

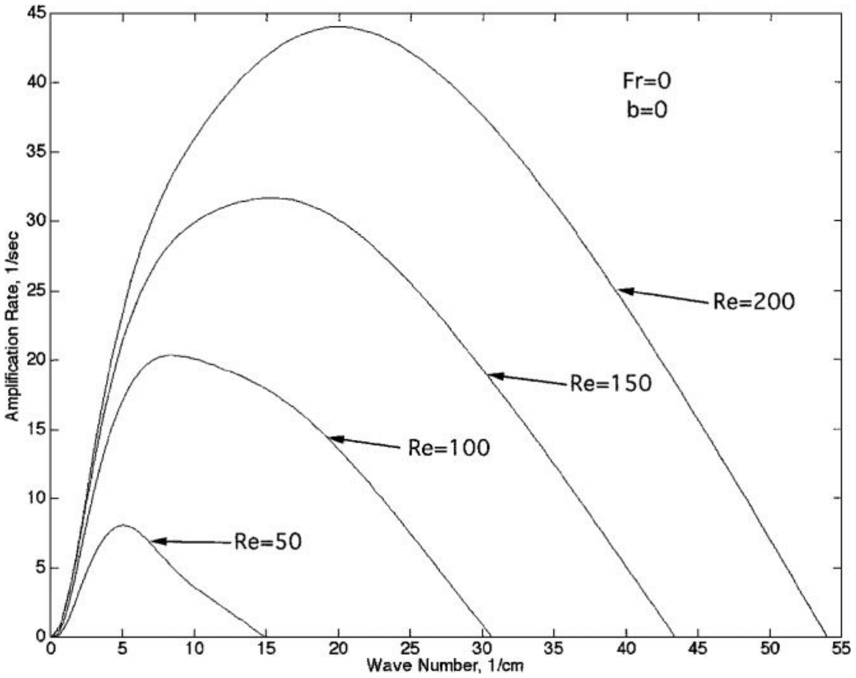

Figure 2.5: Amplification rate of a surface disturbance vs the wave number for different fuels over various film Reynolds numbers. Here, b equalling to 0 represents the absence of gravity forces. (Karabeyoglu et al., 2002)

stability results to the entrainment rate of the liquid from the surface. The influence of the liquid Reynolds number on the amplification curves are seen in Figure 2.5. Changing the port mass flux adjusts the liquid Reynolds number. The force due to gravity is assumed to be zero, and the regression rate parameter is 0.55. The amplification rate increases as the liquid Reynold number (directly proportional to the gas-stream dynamic pressure) rises. The Reynolds number also raises the most amplified wave number, implying that the predicted wavelengths of the instabilities are lower at greater gas flow velocities. This latter result agrees well with experimental data regarding the magnitude of waves created on a thin film's surface (Gater and L'Ecuyer, 1970) .

Another noteworthy finding in the stability study is that both the liquid's surface tension and viscosity have a stabilising influence on the liquid film. This property of thin-film instabilities turns out to be critical in selecting which propellant is most likely to sustain instabilities and entrain droplets into the gas stream. The amplification curves for various liquids at a given film thickness of 0.15mm are shown in figure 2.5 to demonstrate the effect of material parameters on stability. This further suggests the appeal of using paraffin wax as the 'go-to' readily available liquefying fuel for hybrid propulsion systems as it exhibits low surface tensions and low viscosity.

In actuality, the liquid film's linear instability is a necessary but not sufficient condition for entrainment to occur (Karabeyoglu et al., 2002) . Furthermore, the level of entrainment cannot be calculated easily using linear stability analysis. A fully non-linear analysis is required for a thorough understanding of the entrainment problem. The study avoided the problem by assuming that the linear theory's anticipated scaling of the amplification rate delivers a direct measure of entrainment scaling. Despite this, this critical piece of literature set the foundation for further research and leads nicely into the next

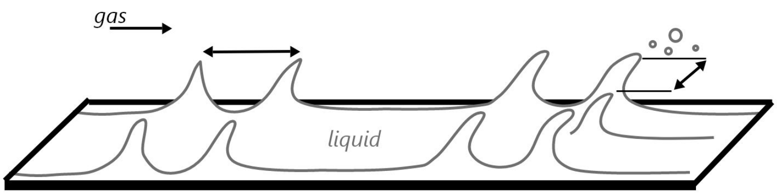

Figure 2.6: Schematic of Kelvin-Helmholtz Instability on the surface of a liquefying fuel with a thin liquid layer. As adapted from (Pelletier, 2009)

section of this chapter - how the oxidiser mass flux can affect the Kelvin-Helmholtz instability in the liquid layer.

2.2.3 Kelvin Helmholtz Instability in liquefying fuels

The inception of entrainment as discussed in Section 2.2.2, and is a key factor in the formation of droplets from liquid layer into the core oxidiser flow. Hydrodynamic forces, together with surface tension forces, govern the deformation of the liquid layer into wave crests. When these forces are applied, the deformation results in the formation of axial waves at the gas-liquid interface (Funada and Joseph, 2001). This is known as the Kelvin-Helmholtz Instability. When excited, these waves give rise to liquid ligaments at a particular distance that is equal to the wavelength. These ligaments are subjected to torsional and shear stresses due to the turbulent and rotational nature of the oxidiser flow over the liquid layer (Nayfeh and Saric, 1971). The results in the formation of droplets breaking from the unstable liquid layer by the Plataeu-Rayleigh Instability (Vandome et al., 2012). The development of liquid layer instability occurs when the surface tension force in the waves is outweighed by the hear forces at the gas-liquid interface. Droplets are accelerated by the oxidiser flow and are further broken down into smaller sized droplets that vaporise more readily (Kuo and Houim, 2011).A visual representation of the KHI in the liquid layer for a liquefying fuel grain can be seen in Figure 2.6.

Petrarolo et al. (2018) focused their research on observing the mechanics of the Kelvin Helmholtz Instability (KHI) in the wave-like structures exhibited by the liquid layer produced in liquefying fuels. In their study, they considered the liquid layer as stationary, whereas the combustion products gas flow moves at a constant speed and that the gravitational force is the only external force that is taken into account. Both the liquid and gas within the immediate vicinity of the interface are considered homogeneous and irrotational, and the influence of viscosity on shear stress is ignored. Linearisation and sinusoidal solutions are used to solve the equations (Kobald et al., 2015) .

The findings from the experimental results reveal that wave-like structures dominate combustion and that the most excited frequencies and wavelengths that characterise the liquid melt layer are affected by fuel viscosity and oxidiser mass flow 2.7. As a result, the liquid viscosity influences the amplified frequency and wavelength values associated with the KHI (figure 2.8), as predicted by the entrainment theories (Karabeyoglu et al., 2002) . The frequency values fall, and the longitudinal wavelengths increase as the viscosity increases. Not surprisingly, the greater viscosity a liquid layer has, the more

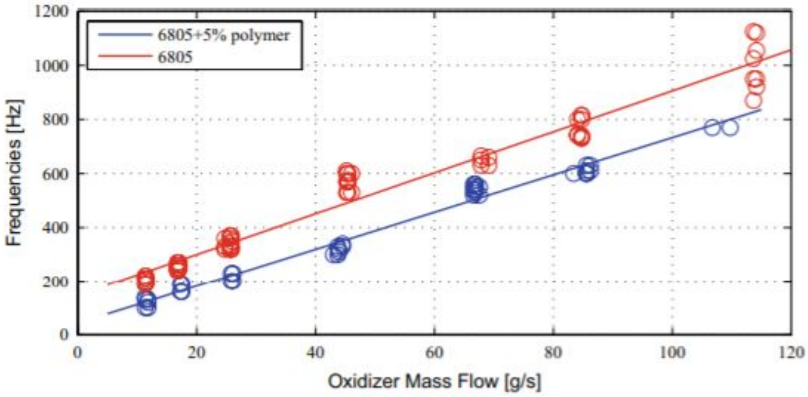

Figure 2.7: The influence of fuel viscosity and oxidiser mass flow on KHI frequencies. (Petrarolo et al., 2018)

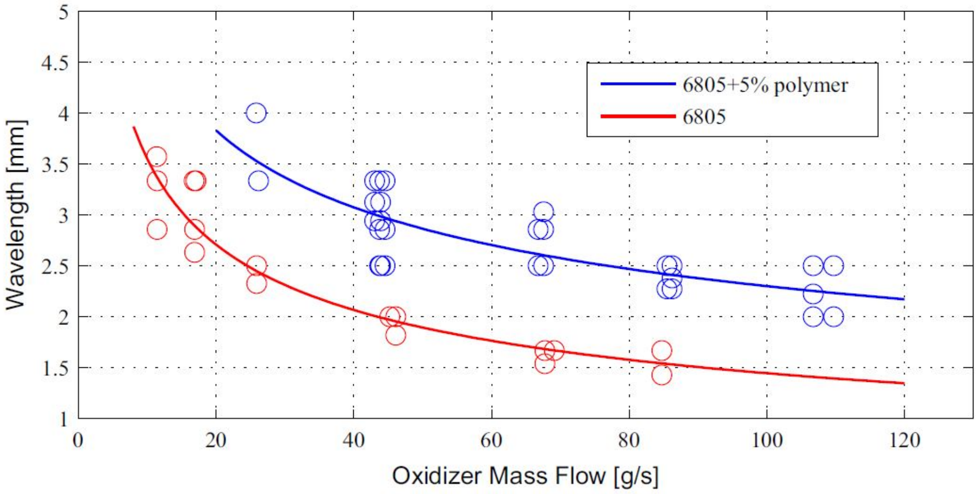

Figure 2.8: Longitudinal wavelengths on fuel viscosity and oxidiser mass flow rate.(Petrarolo et al., 2018)

stable it is. As a result, there are fewer droplets released and leads to lower regression rates. When it comes to oxidiser mass flow, the excited frequencies increase as the oxidiser mass flow increases, while the excited longitudinal wavelengths become smaller.

Petrarolo et al's (2019) study also examined the visualisation of the flame sheet over the fuel surface under combustion. It was also found that as the oxidiser mass flow increases, the flame sheet thickens. This is due to the increased heat exchange rate between the fuel and the gas flow due to enhanced convection and turbulence in the boundary layer. As a result, the liquid layer's melting and evaporation rates rise, increasing the blowing of fuel vapours from the fuel surface to the flame. As a result, the thickness of the boundary layer increases, as does the instability of the liquid layer.

The results from this work were able to validate the KHI frequencies with the liquefying fuel thin film stability theory discussed in Section 2.2.1. Furthermore, for every investigated liquid fuel viscosity and oxidiser mass flow, a direct dependency of the droplets entrainment rate on the liquid layer instability mechanism has been discovered. This means that exact frequencies and wavelengths of the liquid layer could potentially be used to control the fuel regression rate directly.

2.3 Previous works on paraffin based performance enhancement

2.3.1 Paraffin Fuel Mixtures

When it comes to experimentation and application of liquefying fuels, literature thus far has gravitated towards paraffin wax being the ideal fuel due to its abundant availability and relative safe handling. Mixed fuel systems, which are made up of two or more fuel components, could be a way to increase hybrid rocket performance. However, in a comprehensive survey of energetic materials (De Luca et al., 2017) , the use of performance additives (such as metals, boron compounds or metal hydrides) was seen to be an unproductive venture when combined with non-liquefying fuels; suggesting that the lack of oxidiser and combustion beneath the flame limits the effectiveness of metal combustion.

So, heterogeneous fuel systems are being explored, with a large majority focusing on combining HTPB with paraffin to give qualities of each component, such as HTPB's good mechanical properties and paraffin's high regression rates. Furthermore, mixed binder systems may provide one-of-a-kind tools for customising the performance of hybrid rocket propulsion systems to a specific design by varying the fuel composition. Figure 2.9, shows that the effect on performance metrics such as the specific impulse (I_{sp}), only have an effect at low O/F ratios, marginally affecting the peak performance at optimal O/F ratios and then homogenising after the peak.

On a lab-scale hybrid motor, Lee and Tsia (2009) investigated the combustion of HTPB homogeneously mixed with 50%, 70%, and 90% paraffin wax. Oxidiser mass fluxes and chamber pressures were changed in the ranges of 1.4-3.5 MPa and 50-500 kg/m^{2}s, respectively. Curing operations followed normal HTPB curing practises, and mixed fuel samples were made by mixing molten paraffin with heated HTPB at a temperature of 80 °C. According to the researchers, the mixed fuel grains loaded with 70% and 90% paraffin were not physically robust, resulting in considerable unburned fuel ejection

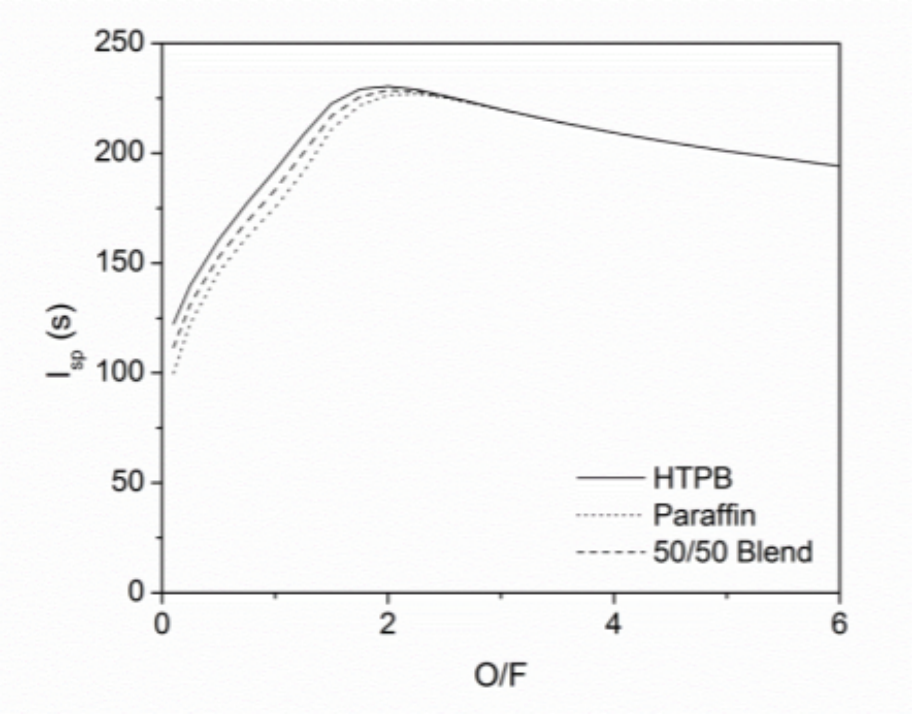

Figure 2.9: Plain HTPB, plain paraffin, and a 50/50 fuel blend burning in GOX at 1000 psia (6.9 MPa) with equilibrium composition, as assessed by NASA's CEA. (Thomas et al., 2017)

through the nozzle and unstable combustion at higher oxygen mass fluxes (Lee and Tsai, 2008) much like what was seen in early experiments with pure paraffin wax (Karabeyoglu et al., 2003) . Under non-swirling GOX flow at a mass flux of 250 kg/m^{2}s, the addition of 50% and 90% paraffin to plain HTPB resulted in approximate regression rate improvements of 10% and 150% over baseline measures from pure paraffin wax fuel grains, respectively.

Pure paraffin, pure PMMA, and HTPB/paraffin were burned by Weinstein and Gany (2011) and Sisi and Gany (2015) . Applying the Marxman (1964) equation for regression rate, the mixed fuel system was similar to that of the pure fuels, with an oxidiser mass flux exponent of 0.59 for the mixed fuel system, compared to 0.67 for pure paraffin. In testing with pure paraffin fuel, residual fuel mass was found in the post-combustion chamber and larger exhaust plumes caused by unburned fuel ejection, but these effects were not observed in the mixed fuel system. This change in burning behaviour was attributed to differences in the mechanical properties of the fuel systems, where the mixed fuel formulation acts as a reinforcing lattice (Sisi and Gany, 2015) and minimising the 'sloshing' effect (Whitemore et al, 2016), but it could also be linked to the lack of a melt layer on the fuel surface due to inconsistencies in the mixture of the fuel grain throughout the fuel port during combustion.

Boronowsky's looked at employing spherical paraffin in a non-homogeneous fuel mixture (figure 2.10) rather than liquid paraffin in a homogeneous fuel mixture to 1) simplify the HTPB fuel curing process and 2) achieve paraffin's regression rate benefits without jeopardising the structural integrity of the fuel grain (Boronowsky, 2011) . Due to a lack of bonding between the paraffin and the HTPB, the fuel formulation containing 30% paraffin spheres displayed mechanical weakness. At higher oxidiser mass fluxes, the addition of 15% and 30% paraffin spheres to HTPB resulted in 25% and 40% increases

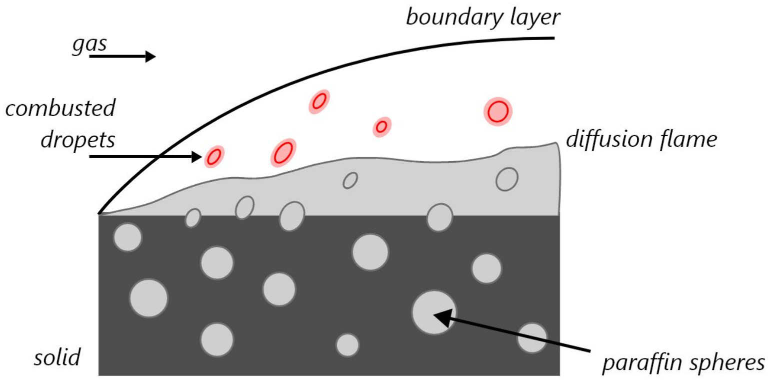

Figure 2.10: Schematic of paraffin spheres embedded as a non-homogeneous mixture with HTPB. As adapted from (Boronowksy, 2011)

in regression rate, respectively (Boronowsky, 2011) .

The effects of paraffin incorporation in HTPB on the combustion behaviour and regression rate improvement are not well understood. According to Lee and Tsai's (2008) combustion studies, when paraffin is incorporated as a molten liquid, a substantial loading is required for significant regression rate enhancement, inconsistent with Boronkowsky's findings - where it was discovered that only spherical particle inclusion results to regression rate improvements at low mass loadings (less than 30%) (Boronowsky, 2011) . The causes of these variances are unknown; however, they could be due to differences in motor scale or operating conditions.

2.3.2 Additively Manufactured Fuel Grains

Another method of augmenting paraffin wax fuel grains is through the use of additive manufacturing. Additive manufacturing, a rapid prototyping technology, provides an effective medium for producing complicated geometries that would be difficult to make using standard manufacturing procedures such as casting. In general, the approach entails layer-by-layer deposition or fusing of materials onto a surface using a computer-controlled algorithm. This manufacturing approach has shown great applicability with various materials, including polymers, ceramics, bio materials, and metals. Its additive nature generates little to no waste and eliminates the need for post-processing or retooling, where conventional methods fall short and necessitate these processes/tools to achieve the desired result.

The use of 3D printing in hybrid rocket research is still recent, with only a few notable investigations of its utilisation with liquefying fuels. At the time of writing, the primary 3D printing material used in hybrid engines is Acrylonitrile Butadiene Styrene, commonly called ABS. The usage of acrylonitrile butadiene styrene (ABS) thermoplastic as a hybrid rocket fuel source was recently examined by Whitmore et al. (2013) . The thermodynamic equivalency of ABS and HTPB when burned with nitrous oxide was one of the most important findings of this study (N_2O). According to a set of comparison studies, the combustion flame temperature for N_2O (ABS) is slightly colder than N_2O (HTPB), but the combustion products have a lower molecular weight. ABS produces approximately comparable

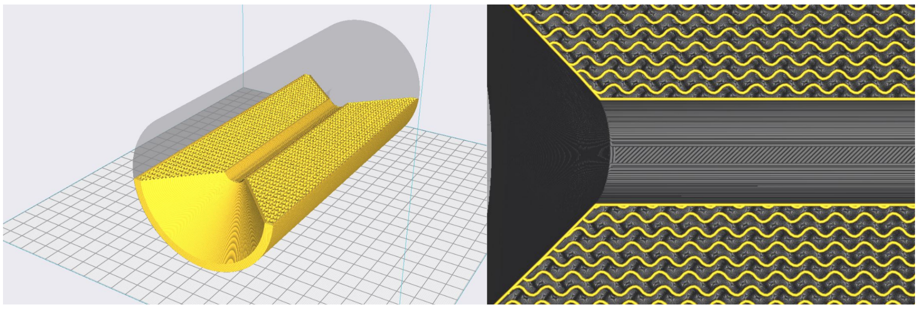

Figure 2.11: Example of what a fuel grain could look like when 3D printing is employed together with paraffin wax.

specific impulse I_{sp} and characteristic velocity (c*) as HTPB. For cylindrical fuel ports, ABS and HTPB fuel regression rates were shown to be statistically equal. Figure 2.11 displays the type of fuel grain capable of being produced with 3d printing ABS and paraffin wax.

ABS has unique material qualities that make it particularly appealing as a hybrid rocket fuel compared to HTPB. ABS is an amorphous material having a noncrystalline structure. As a result, ABS does not have a true melting point and instead vaporises in a highly softened semi-fluid condition. This intermediate fluid state can occur at temperatures ranging from 120 to 140°C (Blom et al., 2006), depending on the exact material formulation. ABS is the material of choice for modern forms of additive manufacturing because of this feature.

The use of 3d printing ABS for hybrid rocket engine fuel grains has been used in various ways, seeking to improve regression rate and performance (Whitmore et al., 2015; Connell et al., 2019) . However, very few have employed additively manufacturing ABS with liquefying fuels. There are two pieces of literature to note when looking at ABS-paraffin systems, one that looked at improving the mechanical properties of paraffin fuel grains utilising ABS reinforcement (Bisin et al., 2019) , and the other a masters thesis exploring a constant-mixture ratio ABS grain filled with paraffin (McCulley, 2012) . Of these two, McCulley's investigation was the only one that looked at performance metrics.

In McCulley's (2012) study, FDM 3D printers were employed to print "hollow" sections, which were then filled with paraffin. The concept behind this fuel grain design was to open voids in the grain to allow for greater mass flow through the ABS structure. Of particular interest from the results of this study was the observation of un-combusted paraffin ejected from the engine for the composite ABS-paraffin fuel grains - suggesting that inefficient combustion of the paraffin wax is still present here.

More recently has been Wang et al's (2020) , where they look at a nested helical structure fuel grain with paraffin wax. The primary idea was to use the differences in ABS and paraffin-based fuel regression rates to keep the structure intact throughout the combustion process. This part of the fuel grain functioned as a mechanical support for the paraffin-based fuel as well as a source of extra fuel. So far, research has been focused on improving the performance of liquefying fuel grains via mechanical modifications or by effecting the oxidiser flow path on a larger scale. However, no one has looked at taking advantage of the liquid layer instabilities close to the fuel surface, where by the inception of droplet entrainment (Ishii and Grolmes, 1975) or the Kelvin-Helmholtz instability (Petrarolo et al.,

2018) have yet to be fully capitalised in a fuel grain design.

2.4 Hybrid Rocket Test Facilities

The primary purpose of a hybrid rocket engine test facility is to sustain continuous combustion through ignition and subsequent oxidiser supply flow at a specific set of conditions (oxidiser pressure and mass flow rate) and at a sufficient quality (stable combustion profiles) for a long enough and often enough to allow for desired measurements to be achieved within these conditions. Most facilities follow similar schematics for static fire testing - typically comprising a combustion chamber, ignition system, oxidiser tanks, feed systems, control valves, sensors and data acquisition systems. Mentioned earlier in this chapter (see Section 2.2), the effects of buoyancy aren't important, thus horizontal test platforms are prevalent in hybrid rocket applications, and they were adapted from solid propellant rockets because the engine mounting is simple, and the configuration is well suited for research purposes with several mounting positions for instrumentation (Barrere, 1960) .

When focusing on collecting performance data from the engine during a test fire, the main feature is what instruments they use and where they install them to achieve the aim of the study. For hybrid rocket engines, the primary parameters of interest are typically thrust (F), characteristic velocity (c^*), thrust coefficient (C_F), mass flow rate ($\dot{m}$), regression rate ($\dot{r}$), specific impulse (I_{sp}) and combustion efficiency (η_b). To study these parameters, the test facility will need to allow for measurement of pressure, thrust and flow rates. Furthermore, since hybrid rocket engines contain high temperatures, vibrations and the fact that it can be a hazard if they malfunction, all of this will need to be conducted with safety precautions.

2.4.1 Ignition Systems

Ignition systems for hybrid rocketry tend to be known as a 'black-art' amongst the rocketry community, with multiple different types of ignition systems all providing enough energy to begin combustion. Most notably are the pyrotechnic-based and gaseous fuel-based ignition systems.

Bouziane et al. (2018) requirements for their test facility was for the ignition system to be reliable, low cost and quick to manufacture. They utilised a pyrotechnic cartridge, where the cartridge is cylindrical in nature with an external port of 21.5 mm and an inner port of 8 mm. The cartridge is designed to sit inside a PVC tube. An industrial-grade ignitor is used to ignite the pyrotechnic and activated remotely via software—the pyrotechnic consists of mainly 75% ammonium perchlorate, 15% Kraton polymer, and 10% aluminium powder. The mixture is then extruded and results in a cartridge resembling a solid rocket motor. Brown and Lydon (2005) employed a similar mechanism to ignite the fuel.

In gaseous fuel-based ignition systems, there are no expendable pieces of hardware. Mechetel and Cantwell (2018) use an oxygen/methane torch ignitor. The ignition system comprises oxygen, injected at low pressures, and a gaseous methane supply and the same pressure. A spark plug is used to ignite the gaseous mixture, and the torch is then run for at least 800ms for a more reliable ignition. The advantage of using this type of ignition is the ability to re-ignite the engine at any point without setting an ignition charge, as would be required for pyrotechnic-based ignitors. However, it comes at a cost to safety as flash-backs can occur as a result of insufficient upstream pressure compared to chamber pressures. To compensate, check valves are added for a layer of safety and calculations are required to ensure adequate mass flow rates.

Despite these two more popular choices of ignition, researchers continue to look to innovative ways to ignite the fuel grain. Whitmore et al. (2015) have explored using arc ignition embedded into the fuel grain to avoid the need for pyrotechnics. It is said that the system allows for multiple consecutive re-starts with no need for hardware change over. However, the reliability of such a system has yet to be fully demonstrated.

2.4.2 Thrust Measurements

Typically, a load cell or strain gauge is used when measuring thrust for most propulsion systems. The most common type of load cell utilised in industrial settings is the strain gauge load cell. A load cell is made out of a metal body with strain gauges attached to it. The body is commonly constructed of aluminium, alloy steel, or stainless steel, making it both strong and flexible. The name "spring element" refers to the load cell's body because of its elasticity. When a force is applied to the load cell, the spring element is slightly distorted, but it always returns to its normal shape unless it is overloaded. The strain gauges change shape when the spring element deforms. The voltage arising from the change in resistance in the strain gauges can be monitored. Because the amount of force delivered to the cell is proportional to the change in voltage, the force may be estimated from the voltage change.

For hybrid applications, where the force is acting in a single direction, Single Point load cells are generally employed for smaller, lab-scaled platforms. The load cell orientation differs by test facility and the mounting mechanism used. In most cases, the load cell is orientated in line with the centre axis of the combustion chamber. Brown and Lydon (2005) and Heydari and Ghadiri (2017) both employed the centre axis orientation for the load cell upstream of the injector. Brown and Lydon mounted the load cell on a 'rail and wagon' mechanism (seen in figure 2.12 (a)). In their facility, the oxidiser inlets are connected perpendicular with the direction of axial thrust, so a T-junction was employed to serve as an interface between the junction and the load cell (mounted on a truss-like structure connected to the engines platform). There seemed to be no issues with the current design; however, a brief investigation could suggest a possible failure at the injector connection point being a stress concentration point if loads were significant.

In the Bouziane et al. (2018) developed lab-scale test facility, the load cell was offset from the centre axis, as seen in figure 2.12 (b), utilising an interface at the face of the injector flange. When single point load cells are used, the geometric design, with an inner aperture (a precise cut-out of its mechanical body), controls the thickness across the load cell body, is key to its ability to accommodate off-centre loading (PCB-Group, 2014) .

With all of these examples, in order for the load cell to measure thrust, the combustion chamber is required to be free moving in the axial direction such to impart displacement onto the load cell.

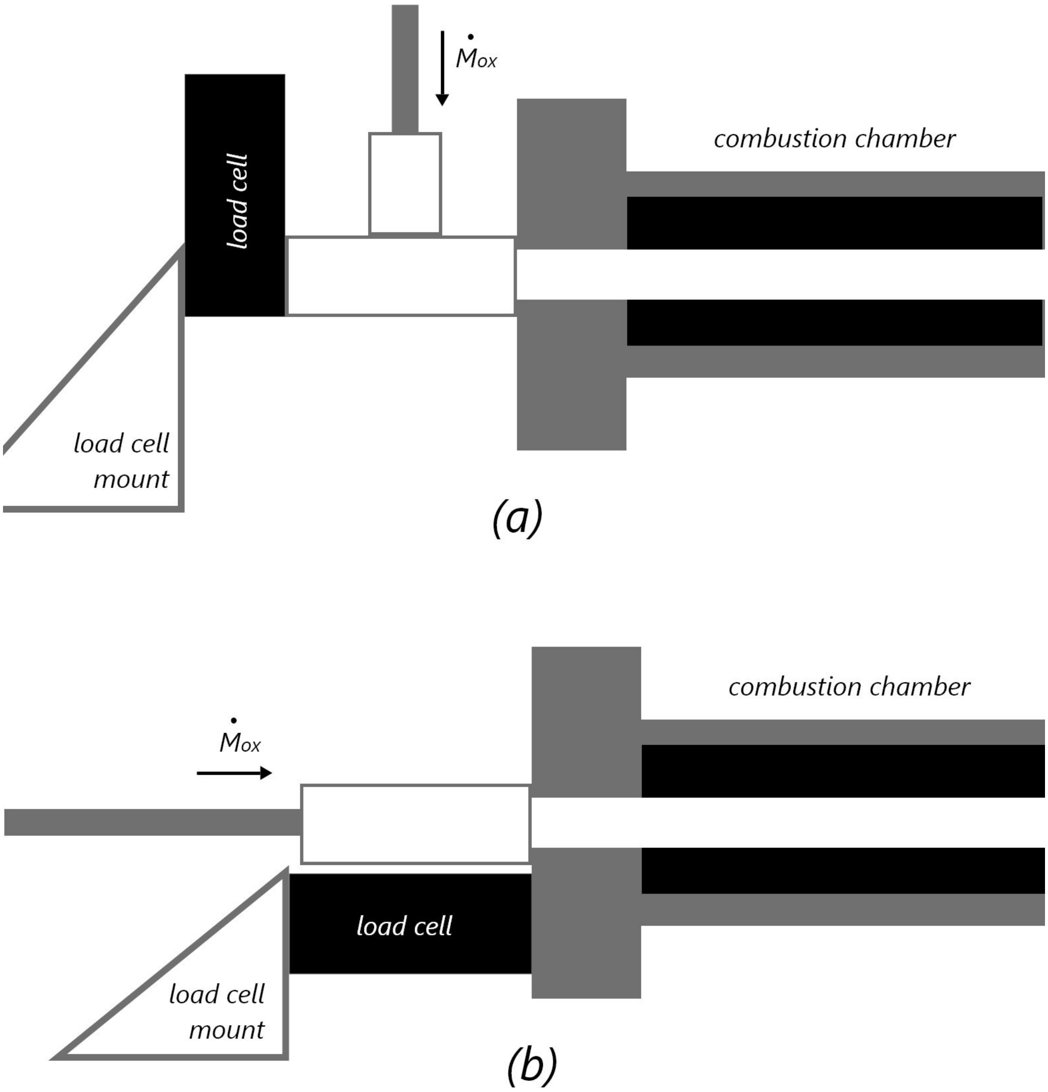
Ṁox
combustion chamber
load cell
load cell
mount
(a)
combustion chamber
Ṁox
load cell
load cell
mount
(b)

Figure 2.12: Load cell configuration schematic. (a) The perpendicular layout as seen in Brown and Lyndon (2005) and Heydari and Ghadiri (2017) facilities and (b) parallel layout as seen in Bouziane et al. (2018) facility.

In the studies mentioned, a rail type mechanism is employed (Heydari and Ghadiri, 2017; Brown and Lydon, 2005) . So it suggests that the orientation of the load cell is dependent on the particular experimental platform, and with single point load cells available, there is flexibility in the position of the load cell to measure the thrust produced from the engine.

2.4.3 Pressure Measurements

Measuring the pressure throughout the engine is one of the key measures necessary to investigate the engine's performance. This is typically accomplished by using pressure sensors/transducers/-transmitters installed at key locations, such as oxidiser feed lines, pre-combustion chambers and post-combustion chambers.

Depending on how the pressure sensor is installed, it can measure either the static pressure, dynamic pressure or stagnation pressure of a flowing liquid. Static pressure, measuring the change in pressure over time, typically requires the sensor diaphragm to be flush at the wall perpendicular to the flow. Brown and Lydon (2005) installed sensors at the combustion chamber and prior to and after a cavitating venturi (necessary when using nitrous oxide as the oxidiser). Bouziane et al. (2018) , and Heydari and Ghadiri (2017) dotted multiple sensors throughout their facility, at the outlet of gas cylinders, upstream of the injector, at the pre-combustion chamber and the post-combustion chamber.

In general, measuring the gas flow pressure is straightforward; however, it becomes more complicated when trying to measure the static pressure within the combustion chamber, where the temperatures can be upwards of 1500K. In these environments, most lower-end pressure transducers cannot handle those temperatures. So there are typically two well-established ways to measure the pressure of extremely hot gases: using high-temperature pressure transducers rated to a sufficient temperature or offsetting the pressure transducer via a tube of known length (Hurst and Van de Weert, 2013) . The former is typically quite expensive and difficult to acquire; although more cost-efficient, the latter requires precise calculations and some degree of simulation to know the exact pressure when referred back into the combustion chamber. The latter was used in Bouziane et al. (2018) and in both Brown and Lydon (1974) , and Heydari and Ghadiri (2017) experimental facilities, the combustion chamber pressure measurement technique was not specified.

Depsite the challenges in both cost and/or implementation, combustion chamber pressure measurements are paramount to truly understanding and calculating the performance of a hybrid rocket engine. These measurements can also prove helpful as references for theoretical models and simulations.

2.4.4 Regression Rate Measurement and Inference

Measuring the regression rate is a crucial to obtaining the performance of a hybrid rocket engine, however, researchers have yet to conclude on the most optimal method to measure the regression rate. The primary issue to contend with is the combustion itself - limiting the type of instrumentation that could be used due to high temperatures, significant radiation and by the nonlinear fuel combustion with increasing burn time. Researchers have used a variety of methodologies to measure the regression rate of hybrid rocket fuel in hopes to overcome these challenges, including ultrasonic techniques to measure the regression rate in real-time, as well as spectroscopic techniques and weight difference methods to obtain the average regression rate over the burn. The methods mentioned here typically output data in the form of a mass flow of fuel, i.e. in g/s or as surface regression in mm/sec. The latter takes into account differences in combustion chamber scale and allows for comparison between difference fuels and engine designs. The former is typically beneficial for application in the calculation of performance metrics where the total mass flow exiting the chamber is needed.

Sorge and Carmicino (2002) experimented with a non intrusive method of measuring regression rate via UV. To obtain the total regression rate using an ultrasonic approach, an array of transducers was required. The procedure entailed transmitting ultrasonic waves into the solid grain with a piezoelectric transducer and measuring the time it takes to cross the fuel thickness. An ultrasonic transducer is a device that can generate high frequency mechanical vibrations when its piezoelectric plate is subjected to variable electrical tension, as well as generate electrical tension when subjected to vibrations. The ultrasonic waves generated in this manner propagate through the material on which the transducer is positioned. They are then reflected back to the transducer at the interface between the internal grain surface and heated gases. The crystalline element is deformed once more, resulting in an electrical impulse that can be recorded. Signals emitted by the transducer are received by a receiver unit, monitored on an oscilloscope, and then elaborated using an oscilloscope dedicated function. This can determine the time delay between the trigger event (broadcast wave) and the zero crossing point of the back-wall echo in real time (reflected wave). Despite this technique being novel and possessing a non-intrusive method of measuring real time regression rates, the measurements from the study still harboured discrepancies, and it was suggested that there was an insufficient number of tests for accurate predictions.

McDougall et al (2019) explored regression rate measurement via spectroscopy of the exhaust flame. At two different depths, magnesium oxide is employed to dope the solid paraffin-based fuel. The fuel regresses to the depths of the doped locations during burning, and the magnesium oxide emits radiation at particular spectral regions. A spectrometer detects the radiation in the combustion plume. The time between the first and second emission peaks, which correspond to the first and second doped spots, can be used to determine the rate at which the fuel burns (known as the regression rate). By conducting a test campaign with a lab-scale slab burner facility, the current work establishes proof-of-concept and assesses the method's uncertainty, while comprehensively describing the method's uncertainty. The technique remains non-intrusive and measures the average regression rate during the fire rather than having to completely halt the burn, however, the technique exhibited roughly 20% discrepancies when compared to optical based measurements, such as those used in Jens et al (2014) .

Measuring the weight before and after the burn remains the most widely used technique to record the average regression rate due to its simplicity, and in most cases, relative consistencies. However, there are cases where the regression rate may be skewed with liquefying fuel grains and this will be discussed later in this thesis. In general, the method involves recording the mass of the fuel grain before the burn, and once again after the burn. The difference in mass is then divided by the burn time - giving you the the mass flow of fuel. In order to express the regression in mm/sec, the volume is calculated before and after to determine the change in the fuel port diameter. However, it is important to note that this method typically works best for simple cylindrical port fuel grains. Overall, there are a number of techniques available to measure the regression rate, with many having advantages for particular use cases and research objectives. An optimal method of regression rate measurement has yet to be reached to establish a standard.

2.5 Chapter Summary

With what has been achieved so far in the research of hybrid rocket engines, the reasons behind why these engines have yet to see widespread use in commercial space applications, despite the discovery of high regression rate fuels in the form of liquefying fuels; is their relatively low combustion efficiency, i.e. the ability to convert that high regression rate into usable thrust. To do this, we need to further improve regression rates and the rate and frequency of droplet vaporisation. Moreover, to do this while ensuring the structural integrity of the fuel grain (Boronowsky, 2011; Lee and Tsai, 2009) , avoiding the need for hazardous additives (De Luca et al., 2017) , and applying an understanding of the observed instability behaviour of the liquid layer through the structural design of the fuel grain (Petrarolo et al., 2018) , which this project hopes to accomplish.

From the literature previously discussed, the following research questions were posed to answer the challenges in enhancing the performance of liquefying fuels:

1. How do changes in surface topology affect combustion chamber pressure, engine thrust and combustion efficiency?
2. Can introducing discrete surface disturbances of particular wavelengths (targeting the Kelvin-Helmholtz Instability analysis for hybrid fuels) enhance vaporisation and improve performance at the corresponding oxidiser mass flow rate?

To answer these questions, the following research objectives were proposed:

1. Design, construct and commission a lab scale hybrid rocket engine test facility fit to test an array of different fuel grains and different operating conditions.
2. Experimentally measure the combustion chamber pressure, thrust and combustion efficiency from static test fires.
3. Manufacture fuel grains via the use of different materials (paraffin wax, ABS and ABS-paraffin) and observe their performance at set wavelength disturbances.

2.5.1 Organisation of Present Work

The chapters to follow will outline the progression of work required to answer the research questions posed and to achieve this study's objectives. A new hybrid rocket engine test facility at Monash University was required to obtain engine performance metrics. Chapter 3 outlines the development and design of the test facility, highlighting key features to reliable operate under the various conditions required for this study and future experiments. The validation process used to ensure repeatability and reliability is addressed in Chapter 4.

Following the successful commissioning of the new facility, Chapter 5 discusses the experimental campaign conducted to measure the performance of a novel ABS-paraffin fuel grain against baseline ABS and paraffin grains. The measurements from the campaign are then used for comparison in Chapter 6 - focusing on key performance metrics such as combustion efficiency, thrust and regression rate.

Chapter 3

Design and Development of Hybrid Rocket Engine Test Facility

As mentioned earlier in Chapter 2, to test the performance metrics generated by different fuel grain formulations, a facility is required to operate in similar conditions to hybrid rocket engine and scaled down to be suitable to operate within a laboratory environment with sufficient safety precautions. At the commencement of this project, such a facility did not exist at the Laboratory for Turbulence Research in Aerospace and Combustion (LTRAC) at Monash University. Therefore, the first stage of this project comprises designing, commissioning, and developing a lab-scale hybrid rocket engine capable of capturing thrust, chamber pressure, and oxidiser mass flows for a variety of different fuel grains. These parameters help characterise the performance of the engine with the means to compare and contrast against other experiments and fuel formulations. Each of these parameters will be explored in greater detail in Chapter 4.

The new facility was designed with the intention to establish a capable 'workhorse' to perform large numbers of back-to-back static test fires while capturing performance metrics via instrumentation such as load cells, mass flow meters and pressure transducers. The approach to the development of the facility was based on similar principles to the development of sounding hybrid rockets (via the advice from seasoned rocketeers within the close rocketry community in Victoria, Australia) as well as the concepts presented by Mechentel and Cantwell (2018) and Whitmore et al. (2015) with their approaches to static firing test facilities. A critical initial consideration was the required size of the test facility and the ability to quickly and easily swap fuel grains between each test fire.

This chapter provides an outline of the design process for developing the Hybrid Rocket Engine Test Facility used in the experimental campaign of this study. The first section delves into the design parameters required for this facility. The chapter will then focus on each essential element of the hybrid rocket engine - Combustion Chamber design, Ignition System, Pneumatics System and Control system, respectively. A validation of the test facility will then be discussed, outlining instrumentation, accuracy and initial validation testing.

3.1 Design Parameters and Requirements

All hybrid rocket fuels considered in the design of this test facility are inert hydrocarbons, although their appearance, structural features, performance, and burn rate vary greatly. Five distinct solid hydrocarbon fuel grains were investigated for their use in possible future experimental campaigns: Paraffin Wax, PolyEthylene (PE) wax, Acrylonitrile Butadiene Styrene (ABS), Hydroxyl-Terminated PolyButadiene (HTPB), High-Density PolyEtheylene (HDPE), and Poly-Methyl MethAcrylate (PMMA). These six fuels were considered because they cover a wide range of burn rates and have published regression rate data for the combustion of these fuels with various oxidisers. The first two fuels, paraffin wax and PE wax, are liquefying high regression rate fuels, whereas the last four, ABS, HTPB, HDPE, and PMMA, are traditional hybrid rocket fuels. Table 3.1 shows the thermochemical parameters assumed for these fuels. With these in consideration, The relative densities of the fuels listed are comparable and the the facility is designed to be able to operate with these typical fuel grain formulations.

Fuel	Molecular Formula	Density [kg/m^3]
Paraffin	$C_{32}H_{66}$	925
PE Wax	$[C_nH_4]_n$	940
HTPB	$C_{654}H_{988}N_8O_{20}$	919
HDPE	$[C_2H_4]_n$	960
PMMA	$C_5H_8O_2$	1100
ABS	$(C_8H_8.C_4H_6.C_3H_3N)_n$	1000-1100

Table 3.1: Regression rate parameters for various oxygen and fuel combinations, with listed references

The design process is outlined by the flow chart seen in figure 3.1. We first begin with the selection of fuel and oxidiser. After the propellants have been chosen, a preliminary evaluation of the expected performance with this combination of propellants is then conducted via the use of Chemical Equilibrium with Applications (CEA) (McBride, 1994). The process of and behind CEA will be explored in greater detail in Chapter 4. In essence, the program is capable of calculating preliminary idealised estimates for the performance of the engine based on key inputs such as fuel and oxidiser combination, chamber pressure, nozzle geometry and so on. From here, the chamber pressure, chamber temperature and mass flow rate are chosen to evaluate the performance of this fuel and oxidiser. These numbers, coupled with the thermochemical characteristics of the propellants, are fed into a chemical equilibrium solver, which determines the final composition of the mixture after combustion. The ideal specific impulse for the propellant combination is optimised throughout a variety of oxidiser to fuel mass ratios (O/F), with the O/F corresponding to the maximum ideal specific impulse being used for the remainder of the design. Non-ideal O/F ratios may be advantageous in some cases, such as when volume constraints outweigh performance benefits, but in general, choosing an O/F that maximises specific impulse should be used to best qualify the results from this study for practical utilisation in hybrid rockets (Toson and Karabeyoglu, 2015).

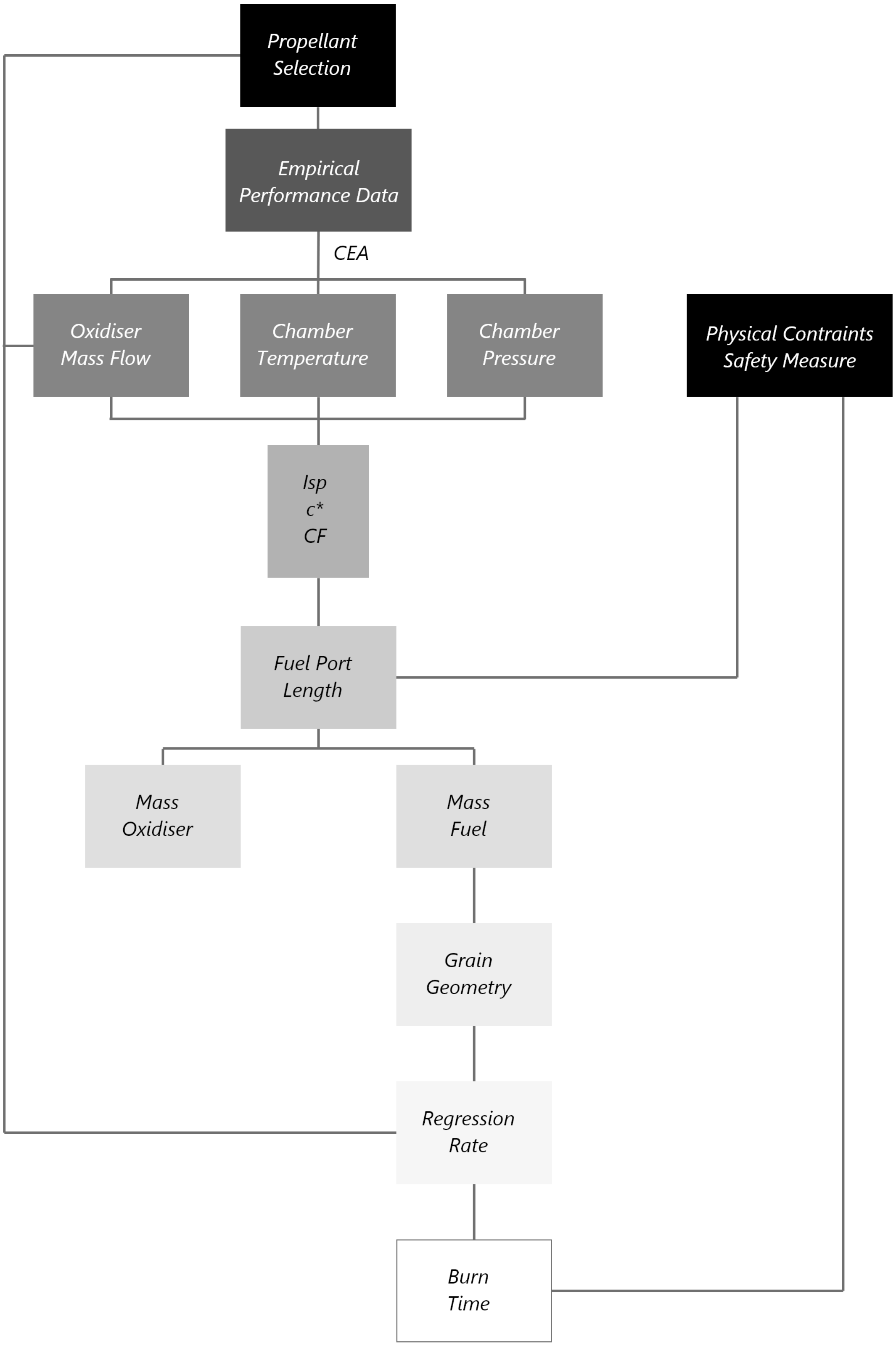
Propellant Selection
Empirical Performance Data
CEA
Oxidiser Mass Flow
Chamber Temperature
Chamber Pressure
Physical Contraints Safety Measure
Isp
c*
CF
Fuel Port Length
Mass Oxidiser
Mass Fuel
Grain Geometry
Regression Rate
Burn Time

Figure 3.1: Simplified flowchart of the design process of the hybrid rocket engine test facility. Details of each step are provided in the text. Here, I_{sp}, c* and C_F refer to the specific impulse, characteristic velocity and thrust coefficient respectively. CEA refers to Chemical Equilibrium with Applications (McBride, 1994).

The burn time must be determined next in the design process - this is the amount of time it takes for the fuel grain and oxidiser to burn. With the current formulation, this is not a free variable in the design because the fuel burn rate is a function of the fuel grain geometry and oxidiser mass flux, which are both fixed if the ideal O/F is to be achieved.

The mass flux in the port is G, the radius of the port is r, and the oxidiser and fuel mass flow rates are $\dot{m}_o$ and $\dot{m}_f$, respectively. For a given fuel/oxidiser combination, the constants a, n, and m are empirically determined parameters. The local mass flux and the local fuel regression rate are coupled as the fuel mass flow rate, m_f which increases with axial distance along the port. The influence of the fuel mass flux and the length dependence of the regression are frequently ignored for simplicity, resulting in the Marxman's regression rate law of the form illustrated in Equation 2.1 (Chapter 2). Although it is usual to employ Equation 3.3 to build a hybrid rocket engine, it can lead to mistakes in the design, notably in the attained O/F ratio. The burn time can then be found based on the estimated regression rate and the assumption of a regulated oxidiser mass flow rate:

$$t_{burn} = \left[\frac{(D_f{}^{2n+1} - D_i{}^{2n+1)pi^n}}{a_o(2n+1)M_{ox}{}^n} \right]^{\frac{1}{1-n}} \tag{3.1}$$

The burn period is t_{burn}, the beginning and final port diameters are D_i and D_f, respectively, and the total oxidiser mass is M_{ox}. The choice of the empirical regression rate constants a_o and n significantly impacts the burn time expression. Because there is a lot of variation and disagreement in the referenced data for these constants, the burn time determined using this method should only be used as a guide. Unfortunately, publishing the oxidiser to fuel ratio at which a specific value of a_o and n was calculated is not standard practice. Consequently, the primary deciding factors to determine the burn time is based on the estimated regression rate as well as taking into account relative safety precautions. As mentioned earlier, the sliver plays an important part in protecting the chamber walls from direct combustion. With this in mind, the high regression rates estimated for pure paraffin wax fuel grains suggested a burn time of 10 seconds being appropriate to provide enough sliver mass to safeguard the combustion chamber casing and lining. As discussed earlier in Chapter 2, the relative length of the burn times seen in previous experimental facilities have ranged from short 3 second burns to other lasting well above 30-60 seconds. Typically the burn time itself is governed by the objective of the experiment, where longer burn times can give profiles that would mimic that of the launch, while shorter burn times can allow for more efficient testing of various fuel grains. With this in mind, 10 seconds of burn time was determined provide enough time for the combustion process to fully develop along the fuel port and regress the fuel a significant amount before reaching the safeguard limit.

Following the burn time calculation (expressed in Equation 3.1), the operational range of oxidiser mass fluxes should be verified throughout the burn to confirm that the mass flux is within a normal working range for hybrid rocket motors. The mass fluxes employed in this study will be based on the mass flow rates used in Petrarolo et al. (2018) Kelvin-Helmholtz's Instabilities paper and a validation exercise employing combustion stability analysis. In Chapter 4, the reasoning behind the mass flow rates chosen will be discussed in greater depth.

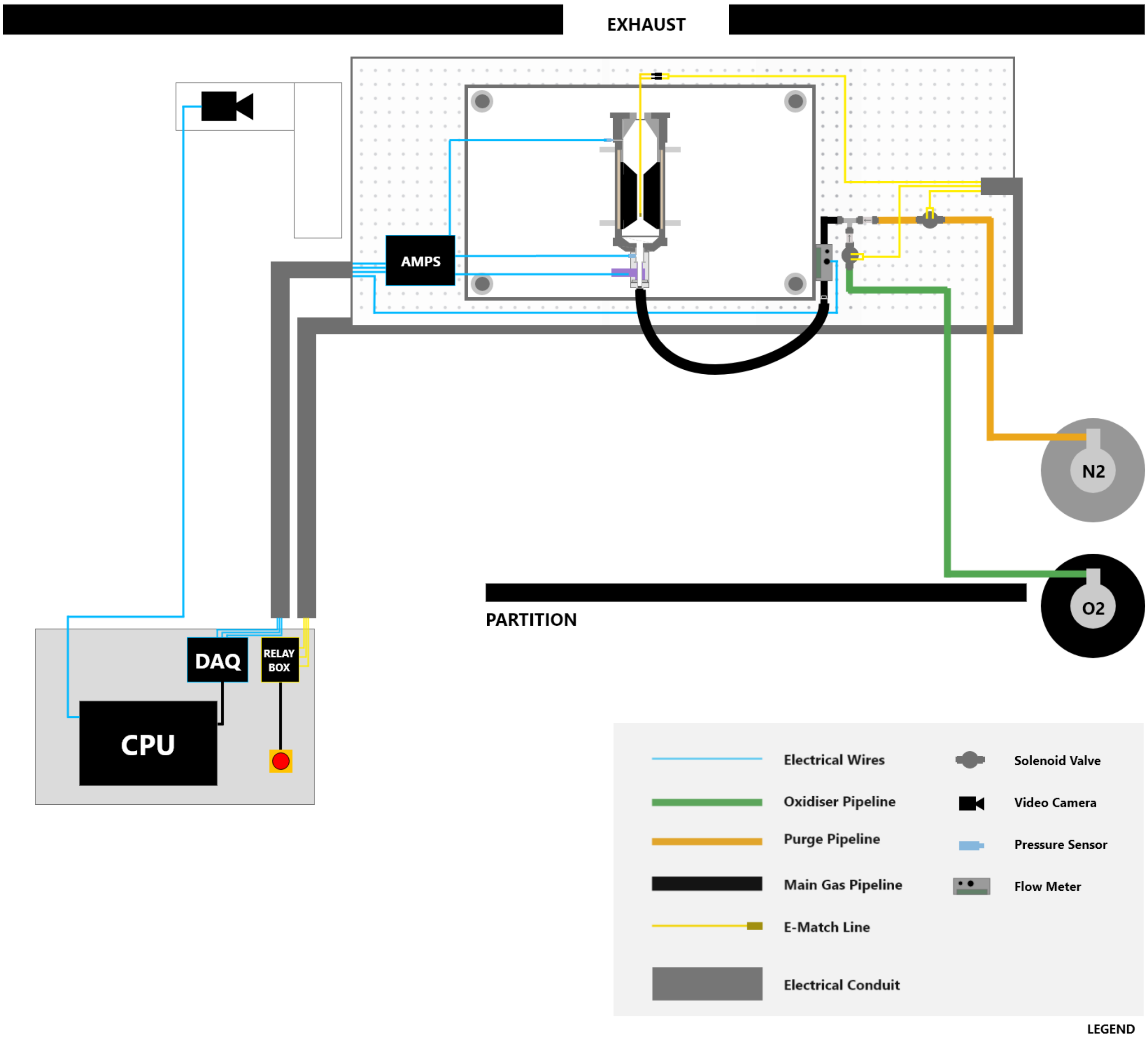
EXHAUST
AMPS
N2
O2
PARTITION
DAQ
RELAY BOX
CPU
Electrical Wires
Oxidiser Pipeline
Purge Pipeline
Main Gas Pipeline
E-Match Line
Electrical Conduit
Solenoid Valve
Video Camera
Pressure Sensor
Flow Meter
LEGEND

Figure 3.2: Schematic of the Hybrid Rocket Engine Test Facility located in the LTRAC Combustion Lab.

After iterating on the process outlined earlier, the hybrid rocket engine test facility has been designed to operate at up to 15bar oxidiser pressures, with inlet mass flows being able to safely reach up to 15.5 g/s. The facility will be able to experiment with a variety of oxidisers, but has been optimised for gaseous oxygen. The design of the nozzle will greatly affect the thrust output of the engine, however, to take into account safety - a maximum thrust output of 200N has been placed on the facility. The appropriate measures to ensure this will be outlined later in this chapter. A schematic of the test facility can be seen in figure 3.2.

3.2 Combustion Chamber

The stainless steel foreclosure accommodates the injector port, which is located upstream of the fuel grain and is designed to enclose the body of a pre-combustion chamber and pressure tested to withstand up to 39bar. The injector for this chamber is a basic port because the device employs gaseous oxygen as its oxidiser. The pre-combustion chamber′s primary function is to keep the flow exiting the injector upstream of the fuel grain port entry stable by dampening oscillations from the injector before combustion occurs (Lee et al., 2020). The necessity of maintaining the inlet oxidiser flow leads to combustion stability and, as a result, the stability of the combusted gases exiting the system. Where analysing the exhaust plume can reveal information about the flow′s stability upstream and this will be explored further later in this chapter.

Most of the time, the total mass of the fuel grain is raised to account for the unburned sliver percentage, which is commonly considered to be 1% of the total mass for hybrid rocket engine ground testing. The use of a commercially available Cesaroni Pro98 engine casing effectively defined the outside diameter of the fuel grain - combined with a preset length of 380mm, the overall mass of the fuel grain was decided mostly by the density of the fuel. To minimise tensile hoop stress in the port, structural considerations for a thick-walled cylinder demand that the ratio of the outer diameter, D_O, to the inner diameter, D_i, of the fuel grain should be around 2-3 - this is especially important for high regression rate fuels like paraffin and PE wax. The length of 380mm is employed to give enough length for mixing, resulting in optimal propellant consumption and assuring port operation across a tolerable range of mass fluxes, G.

The nozzle geometry is established by first calculating the size of the nozzle throat by solving for the throat size required to achieve the specified chamber pressure using the knowledge that the nozzle throat will be choked. In order to guarantee that the Mach number in the port is low, the diameter of the nozzle throat must be compared to the initial diameter of the fuel port. Equation 3.5 and the hydrodynamic characteristics of the combustion products generated by CEA can thus be used to estimate the upstream Mach number.

$$\frac{A_t}{A_{port}} = (\frac{\gamma+1}{2})^{\frac{\gamma+1}{2(\gamma-1)}} \left[M(1+\frac{\gamma-1}{2}M^2)^{\frac{-(\gamma+1)}{2(\gamma-1)}} \right] \tag{3.2}$$

The nozzle throat area is denoted by A_t, A_{port} denotes the initial cross-sectional area of the port, the ratio of specific heats is denoted by γ, and the Mach number at the end of the port is denoted by M. The influence of heat addition from combustion in the post-combustion chamber is ignored in this equation. A reasonable rule of thumb is to make sure the Mach number in the port, computed with Equation 3.5, is less than 0.3 (Chandler et al., 2012), which corresponds to a diameter ratio (D_i/D_{throat}) of at least 1.5. With a port diameter of 15mm, this leads to a nozzle throat diameter of 10mm.

The nozzle was made of high-grade graphite and was heavily influenced by the need for repeatability in this experimental campaign, guaranteeing that it could resistant to extreme temperature gradients. The design of a converging nozzle was limited by the critical back pressure required for the flow to achieve supersonic speeds at the throat, which necessitated a big enough area ratio from the nozzle′s inlet to the throat to accelerate the flow up to this threshold. Using a converging nozzle rather than a converging-diverging nozzle was chosen to eliminate any biases in the thrust levels collected. Variations in the geometry of the fuel grains will affect chamber pressure, which could lead to an advantage

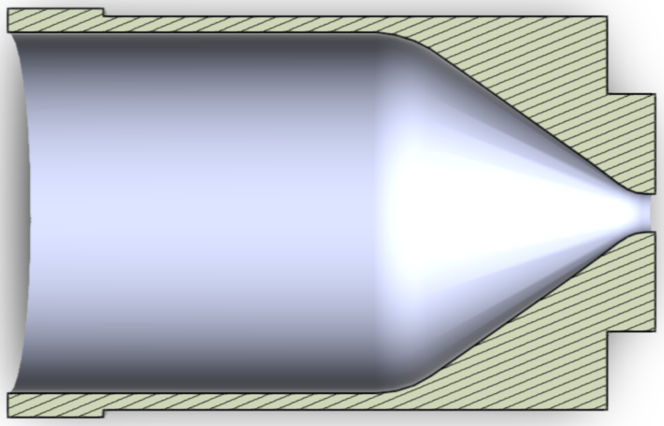

Figure 3.3: Cross sectional view of the converging graphite nozzle used in the Hybrid Rocket test facility.

with the nozzle design for that specific chamber pressure generated, improving its performance and skewing the results of this study.

An integrated post-combustion chamber reduced complexity and allowed for a seamless transition from the post-combustion chamber to the converging nozzle. This portion, made of the same material as the nozzle, can survive the high temperatures produced by combustion. The post-combustion chamber, located downstream of the fuel grain and before the nozzle, improves the mixing of fuel and oxidiser. It accomplishes this by taking advantage of the greater distance between the end of the fuel grain and the nozzle's entrance, allowing the mixture to mix and combust any uncombusted fuel particles. At the flame zone, hybrid combustion processes tend to be fuel-rich. These qualities need mixing downstream of the grain, as well as the potential requirement to inject extra oxidiser at the aft end due to throttling (which is not prefered); an appropriate combustion volume must be provided prior to expansion out of the nozzle to avoid this (Markle et al., 2003) . The use of paraffin wax as the fuel grain material further demonstrates the need for more combustion volume - where droplet entrainment mass flow is significantly greater than mass flow resulting from direct gasification, leaving a significant amount of unburned material ejected from the nozzle (Whitmore et al., 2015) . Understanding and employing more strategies to encourage improved mixing will ultimately improve combustion efficiency in the long run.

3.3 Hybrid Rocket Engine Platform

The test facility must be lifted to be in line with the cavity in order to access the exhaust vent placed in the LTRAC combustion lab, as explained earlier in this chapter. This section of the facility was designed with a modular design philosophy in mind, allowing for the installation of various equip-

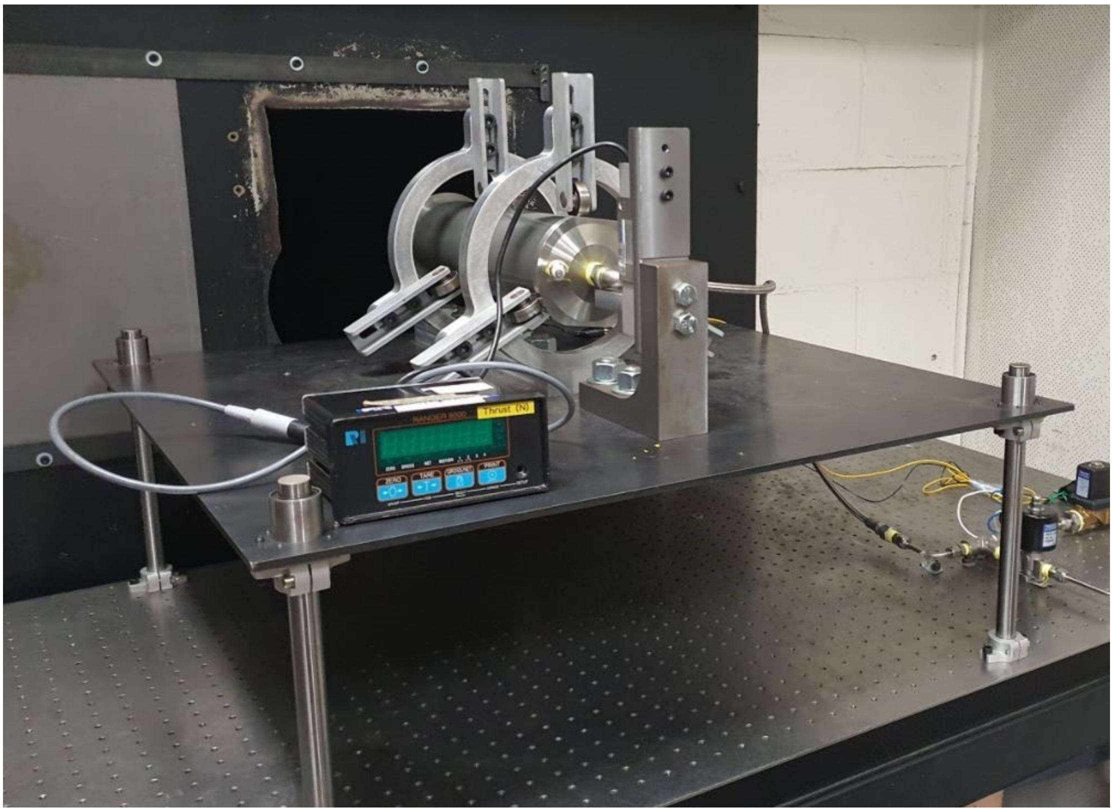

Figure 3.4: Photographed image of the linear bearing platform. Also captured in this image are the radial bearing mounts.

ment and conducting various experiments. To do so, a mild steel platform with four linear bearing steel shafts is fitted, allowing the platform to be changed to the desired height (figure 3.4). Both the steel shafts and the mild steel platform contribute to the structural integrity and rigidity of the structure.

Two radial bearing mounts are mounted on top of the platform. Each mount contains three bearings (figure 3.4) designed to be at equidistant angles to aid engine alignment. The ability of roller bearings to reduce radial vibration during static fires while ensuring that the thrust generated by the engine is focused axially along the load cell is a benefit of using them in this way. For the load cell to measure the thrust produced by the engine, it must be able to move freely in the flow direction. Like the linear bearing platform, the radial bearing mounts can be modified to fit various combustion chamber diameters ranging from 35 to 120 mm.

3.4 Ignition System

Ignition is performed using commercially available electric matches (e-match) wrapped in steel wool around the fore-end of the fuel grain (available from rocketry retailers). A bridgewire and a pyrogen are the two components of an e-match. The bridgewire is a heating element encased in the pyrogen, a quantity of easily lit pyrotechnic initiator compound. Applying 12 V over the e-match wire is all it takes to start the engine. The ignition flame burns the steel wool, spreading throughout the fuel grain port (figure 3.5). The e-match wire typically burns through, separates from the fuel grain, and exits the combustion chamber shortly after oxidiser flow begins.

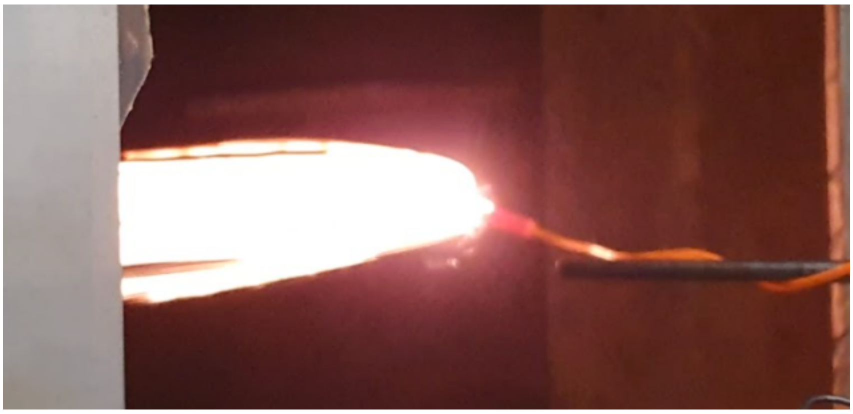

Figure 3.5: Electric match igniting bundle of steel wool. Depicting the development of the ignition flame that takes place within the port of the fuel grain.

Each ignition charge uses steel wool that is precisely weighed to 1.5 grams to assure dependability and consistency. The steel wool is spread out to maximise its surface area, allowing the fuel grain port to burn evenly. A standard configuration was developed by iteratively testing a precise quantity of steel wool across a range of ABS, Paraffin, and ABS-Paraffin fuel grains.

3.5 Pneumatics System

Figure 3.2 represents the complete pneumatics system for oxidiser and nitrogen purge flow and control, with pictures of the facility shown in figure 3.6. The system consists of two gas lines that connect to a single header and the combustion chamber's injector. The pneumatics system on the optical table is made of stainless steel 1/4 inch pipework, with retaining holds bolted in place to maintain system rigidity. The 1/4 inch stainless steel braided hoses connecting the gas cylinders to this system provide the inputs. The primary header line runs directly from a mass flow meter to the combustion chamber's injector piece.

- Oxygen Gas (0_2) (5-10bar): main oxidiser feed (capable of 5-18 g/s) controlled via pneumatic solenoid valve actuation. The gas cylinder is equipped with a derivative-based (PID) pressure feedback regulator system (Cigweld Comet Oxy 5000 regulator) to control the pressure, and in turn the mass flow rate of oxidiser.

- Nitrogen Gas (N_2) (5bar): combustion chamber purge controlled via pneumatic solenoid valve actuation. The gas cylinder is equipped with a (PID) regulator system (BOC 8000 Single Stage Nitrogen Regulator).

To isolate the mass flows of oxidiser from the nitrogen purge lines, check valves are included after each solenoid valve before the main header line (figure **??**- this ensures that no gases flow back into the wrong line in the off chance of both solenoid valves being actuated simultaneously. With all of this, the pneumatics system can reliably control the flow of gases required for engine operation. We will now look at the controls systems used to control the sequencing of these gas flows for engine start, operation and shutdown.

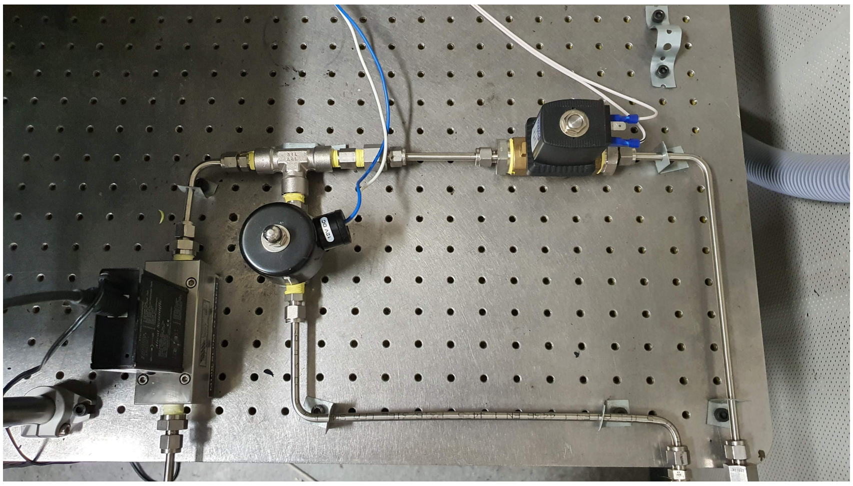

Figure 3.6: Image taken of the pneumatic system installed on top of the optical table. Pictured (from left to right) is the Alicat Flow Meter, oxidiser solenoid valve, nitrogen purge solenoid valve and accompanying check valves.

3.6 Instrumentation

A Kulite WCTV-312M-17BARA pressure transducer is used to measure the pressure at the post-combustion chamber during combustion. This allows for the calculation of parameters such as combustion efficiencies and thrust coefficients. Pressure taps were manufactured on the flat surfaces of the aft closure to allow for sufficient sealing via a gasket when the pressure sensor is threaded. The pressure tap penetrates through the stainless steel housing and the post-combustion chamber graphite insert allowing the sensor to sit flush with the chamber wall. This high-temperature pressure transducer is rated to withstand up to 1366K - and was sufficient to withstand static fires for this study. The sensor sends signals through a x100 signal conditioner amplifying the signal from 0-100mV to 0-10V - minimising static interference, which was projected to be in the order of around 20mV. These sensors have been calibrated when purchased from Kulite, with a manufacturer stated accuracy of ±0.5 % of the maximum full-scale output (FSO) - equating to a ±0.085 bar variance in the pressure data measured from the instrument. The inlet pressure sensor was calibrated via a hydraulic sensor calibration unit which is able to apply pressure onto the sensor via a combination of weights with a known mass. From this, a curve was developed and offset appropriately in software. In this case, the pressure sensor from the suppliers was relatively accurate and was seen to be within the manufacturers stated tolerance of ±0.5 % of the maximum FSO.

At the inlet of the combustion chamber injector, a Firstrate Co. FST800 pressure sensor rated to 21bar is installed to measure the inlet pressure entering the combustion chamber. The sensor had a manufacturer stated accuracy of ±0.5% of the FSO, with a thermal sensitivty shift of ±0.02% FSO/°C with signal outputs between 0-5 VDC. An injector piece was manufactured (figure 3.7) to minimise flow disruption of the oxidiser flow into the combustion chamber. The piece is designed with a smooth transition to minimise flow recirculation and the hose connection orientated to avoid sharp corners, where the flow may separate. The inlet pressure transducer sends signals through a separate signal conditioner connected to an Arduino Uno module, amplifying the signal from 0-5V to 0-15V and run via in-house Arduino code.

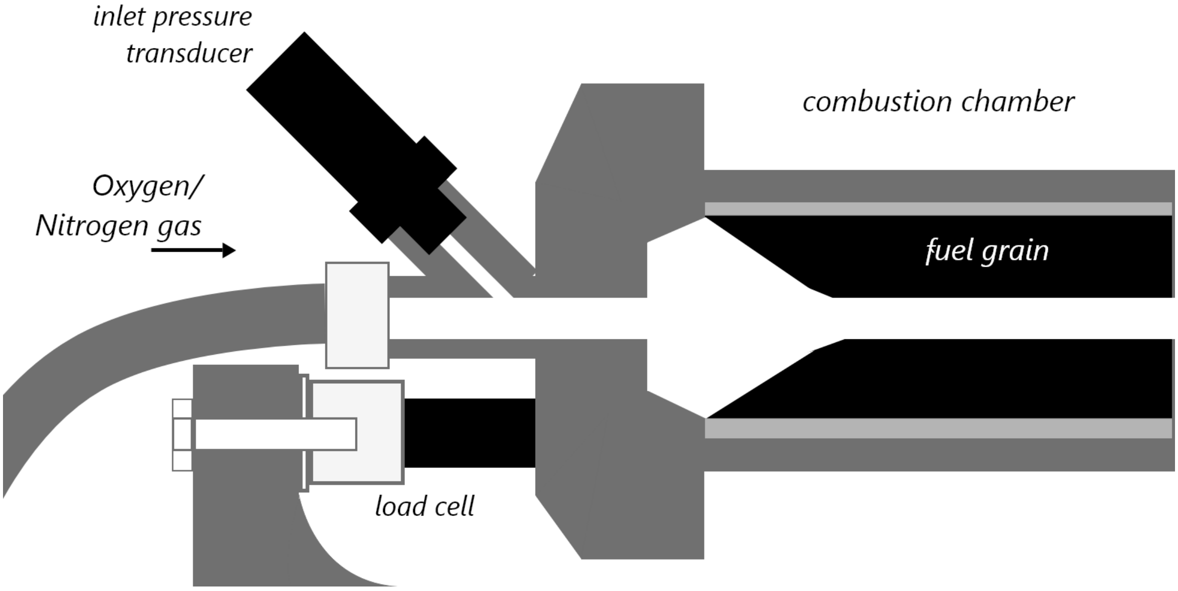

Figure 3.7: Schematic of injector side of the combustion chamber. Housing the injector port, inlet pressure transducer and load cell.

Upstream of the inlet pressure transducer is an Alicat Scientific M-Series 0-100SLPM mass flow meter to provide real-time mass flow rate measurements of the oxidiser entering the combustion chamber. A more detailed overview of how this flow meter works can be found in Appendix A. The standard litre per minute (SLM or SLPM) is a unit of volumetric flow rate of a gas at standard temperature and pressure (STP), which is most widely used in the United States, whereas the normal litre per minute is used in Europe (NLPM). When utilising SLPM, the standard conditions for temperature and pressure are assumed to be zero degrees Celsius, which differs from the "room" temperature reference for the NLPM standard due to changes in ambient temperatures and pressures during data collecting.

$$1LPM = 1SLPM * \frac{T_{gas}}{273.15K} * \frac{14.5046psi}{P_{gas}} \tag{3.3}$$

The mass flow meters have a manufactured stated accuracy of ±0.8% of the reading and ±0.2% of the FSO. The Alicat mass flow meters have in-built temperature and pressure sensors that it uses to determine the mass flow of the oxidiser. The temperature measurement from this instrument was used to measure the daily temperature of the oxidiser during the test campaign, which varied between 19°C to 21°C.

The load cell installed to measure thrust was a Tedea Huntleigh wired led single point load cell, rated to 30kg. The instrument is made from an aluminium construction with a single point platform size of 400x400mm. The mounting configuration for the load cell can be seen in figure 3.7, where an offset plate was machined to allow for the strain gauge to activate and bolted onto the load cell mount. The instrument is connected to a Ranger5000 digital indicator using a 24 bit Sigma Delta A/D Converter. The rated output of the load cell is 2.0 mV/V with a rated tolerance of 0.2 mV/V. The Ranger5000 is connected to the facilities main PC via an RS-232 serial communication protocol and run via an LTRAC developed Python script. The sample rate, when combined with the Ranger5000 and the Python script, reached 10 samples/second. The load cell was rated to have an accuracy of ±0.05% of the rated maximum output (in this case, 30kg) and was calibrated directly using the same weights in the inlet pressure sensor calibration process. The Ranger5000 digital indicator had a built-in digital calibration setting. Zero calibration and span calibration routines were performed before applying linearisation since both the zero and span calibration points are used in the linearisation scale base. The process involved the input of up to five linearisation points using a known mass - once completed, the linearisation was set for the rest of the experimental campaign.

3.7 Data Acquisition

Data is acquired from the test facility using a National Instruments USB-6341 DAQ (Data Acquisition System) for sampling the combustion chamber pressure and oxidiser mass flow rate from the instrumentation mentioned earlier in this chapter. The USB-6341 offers analog input (16 AI at 16bit and 500 kS/s) and output (2 AO at 900 kS/s), digital I/O (24 multifunctional DIO), and four 32-bit counters. The 500 kS/s is aggregated across all active analog input signals, i.e. the sampling rate is reduced to 250 kS/s when two devices are actively taking measurements. For the purposes of this study, 250kS/s is more than enough to attain combustion chamber characteristic behaviours at operating pressures between 5-10 bar.

DAQExpress virtual instruments were also used to acquire the data over the duration of the burn. The NI-DAQmx driver configuration can be seen in figure 3.8. The data is captured and displayed on the virtual instrument graphical interface, where the data is then exported and processed. The process of is quite simple since the only instrument inputting any signals into the DAQ is from the combustion chamber pressure transducer. The process flows by first initiating the recording the pressure data, which is then shortly followed by a signal sent to the electrical ignition match to start combustion. After a 0.5 second delay, the oxidiser solenoid is actuated and is kept open for the 10 second burn. The length of the burn is primary governed by the length of time the oxidiser solenoid is held open. The signal to the valve is then shut, causing the valve to close. After a 1 second delay, the nitrogen solenoid is then actuated for another 10 seconds to purge the chamber after the hot fire. After which, all solenoids are shut down and program ends.

3.8 Control Systems

The gas valves are all controlled via a USB-6341 National Instruments Data Acquisition Device (DAQ) and using the DAQExpress software (National Instruments) visual interface (VI). DAQExpress communicates with a 4-channel relay module connected to the oxidiser solenoid valve, the nitrogen solenoid valve and the e-match. The relay module outputs 12V to the elements connected to each relay and is supplied a separate power supply (12V, 8A) to run each relay. The control inputs for each relay is wired to digital output signals on the DAQ - where 'high' and 'low' signal states are controlled via software.

A sequence of digital output signals is developed using the virtual instrument (figure 3.8). This gives complete control over the timing of each step, from ignition to oxidizer flow to purge. During the validation of the facility, the timing between ignition and oxidiser flow was iteratively established, and

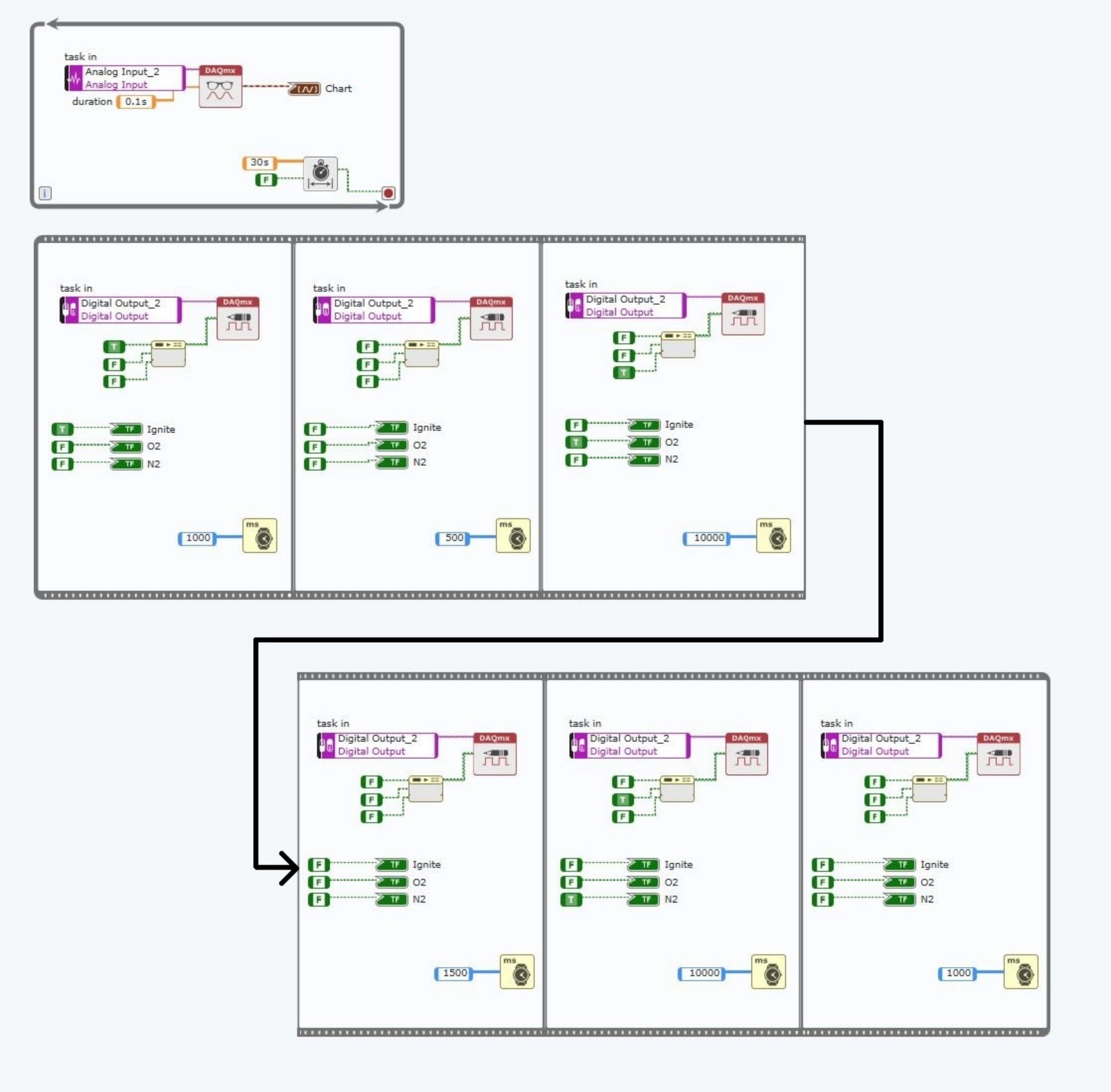
task in
Analog Input_2
Analog Input
DAQmx
duration
0.1s
Chart
30s
F
task in
Digital Output_2
Digital Output
DAQmx
T
F
F
T
F
F
Ignite
O2
N2
1000
ms
task in
Digital Output_2
Digital Output
DAQmx
F
F
F
F
F
F
Ignite
O2
N2
500
ms
task in
Digital Output_2
Digital Output
DAQmx
F
F
T
F
T
F
Ignite
O2
N2
10000
ms
task in
Digital Output_2
Digital Output
DAQmx
F
F
F
F
F
F
Ignite
O2
N2
1500
ms
task in
Digital Output_2
Digital Output
DAQmx
F
T
F
F
F
T
Ignite
O2
N2
10000
ms
task in
Digital Output_2
Digital Output
DAQmx
F
F
F
F
F
F
Ignite
O2
N2
1000
ms

Figure 3.8: DAQExpress (National Instruments) Virtual Instrument coding diagram. The diagram outlines the process conducted for each test fire in this study. Beginning with ignition, a small delay, oxidiser solenoid actuation and then purge solenoid actuation.

it was discovered that a delay of 500ms was sufficient to allow the e-match to burn the steel wool. If the delay is too short, the oxidiser will blow out the ignition flame before it has a chance to propagate; if the wait is too long, the steel wool will burn out completely before the oxidiser can propagate and sustain the flame.

All valves are normally closed, and a manual emergency stop button is installed between the power supply and relay module - once pressed, all power is cut to the relays, forcing the solenoid valves to close. In the case of an emergency, this button will halt the supply of gas into the combustion chamber. Once the situation is cleared and the oxidiser solenoid valve is closed via the software, the emergency stop button can be de-activated, and the nitrogen purge will be ready to flow. The reason behind closing the nitrogen purge in the case of an emergency is to avoid any flashback going into the gas cylinder; high pressures through the 1/4 inch stain steel pipework can prove a significant hazard.

The exact sequence can be modified from test to test, depending on the requirement. In this case, all experiments were run under the same configuration. Figure 3.8 outlines the flow of processes from ignition to data processing.

3.9 Exhaust Plume Stability

The exhaust plume can give some insight into the combustion stability within the chamber. A Daheng Imaging Mercury high-speed optical colour video camera is used to capture high frame rate imaging of the exhaust plume at the exit of the nozzle. The focused distance of the camera is 1500 mm (Z_D = 1500mm) away from the core of the exhaust flame, the focal length is 25mm (f = 25mm), and the camera's pixel size (d_{px}) is $3.45e^{-3}$mm (3.45 micrometres). The sensor has a maximum size of 2048 x 1536 pixels. The required field of view to adequately capture the exhaust plume yielded 400mm x 100mm and the required camera distance away from the exhaust plume was 1.5m. The camera is connected to a PC via USB3.0 and captured via MATLab's image acquisition tool. Within this tool, the camera's field of view was inputted. The bright exhaust flame was filtered down to only show the core of the flame by reducing the f value of the camera to 8 and the exposure time down to the minimum achievable, 20μm. With this configuration, the camera was able to record at a stable 180 frames per second (FPS).

Initial tests yielded the images of the core flame displayed in figure 3.10. The plume has a complicated structure that can be split into three regions: near field, transition region, and far field (Dash and Wolf, 1984) . The plume structure scheme is depicted in Figure 3.9, and we can see a rough schematic of the plume scheme overlaid on an image taken from plume footage once combustion has stabilised (figure 3.10). The near field can be seen at the engine's nozzle exit, where the flow from inside the nozzle dominates the plume structure. In the transition zone, however, mixing with the atmosphere increases while core flow decreases and loses its influence on plume structure. While the mixing with the ambient environment takes full impact, the core flow has evaporated in the far-field and no longer plays a function.

The plume structure did not appear to be affected by the fuel grains employed in the preliminary testing; however, the flame emission varied substantially. The core flow from the nozzle exit can be separated into two components, according to Simmons (2000) , the inviscid inner core and the viscous outer core (mixing layer). It is hypothesised that no chemical reactions take place within the inviscid core (Simmons, 2000) . It can also be observed in this diagram that the mixing layer thickness grows as the distance from the nozzle outlet increases.

In contrast to the mixing layer, the flow in the inviscid core is non-reacting. The viscid flow in the mixing layer surrounds the core flow. The reactions are triggered by mingling with the surround-

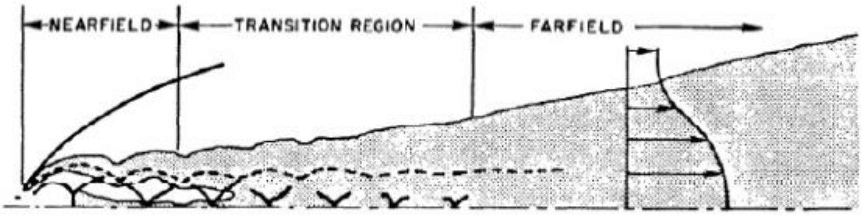

Figure 3.9: Schematic of the exhaust plume structure depicting the three regions: near field, transition region and far field (Dash and Wolf, 1984)

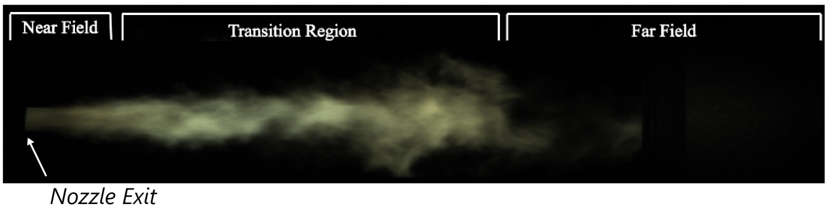

Figure 3.10: Exhaust plume structure overlay over exhaust plume image captured in this study.

ing environment, according to (Simmons, 2000) .

Afterburning is an additional series of processes in the viscous mixing layer. Afterburning, on the other hand, is dependent on altitude. Only when the oxygen concentration is high enough can the chemical process that causes afterburning to occur. Afterburning causes increased temperatures in the mixing zone, which results in infrared emissions that can be seen (Dao et al., 1997) .

Focussing on the near field, the effects of the outer viscous mixing layer dominate the inner inviscid core with a converging nozzle - this is due to the fact that without the diverging section to accelerate the flow further, the ambient environment will overwhelm the flow core much sooner and resulting in a shorter relative near field length. This viscous outer layer is where reactions with the surrounding environment take place. After-burning is a set of reactions that can take place within the viscous outer layer. As the plume continues to extend and converge towards the free-stream condition, this process of after-burning reduces, resulting in less mixing, lower temperatures, and hence fading of observed emissions. Further from this point, the plume has completely blended with the surrounding environment and has diffused throughout the atmosphere.

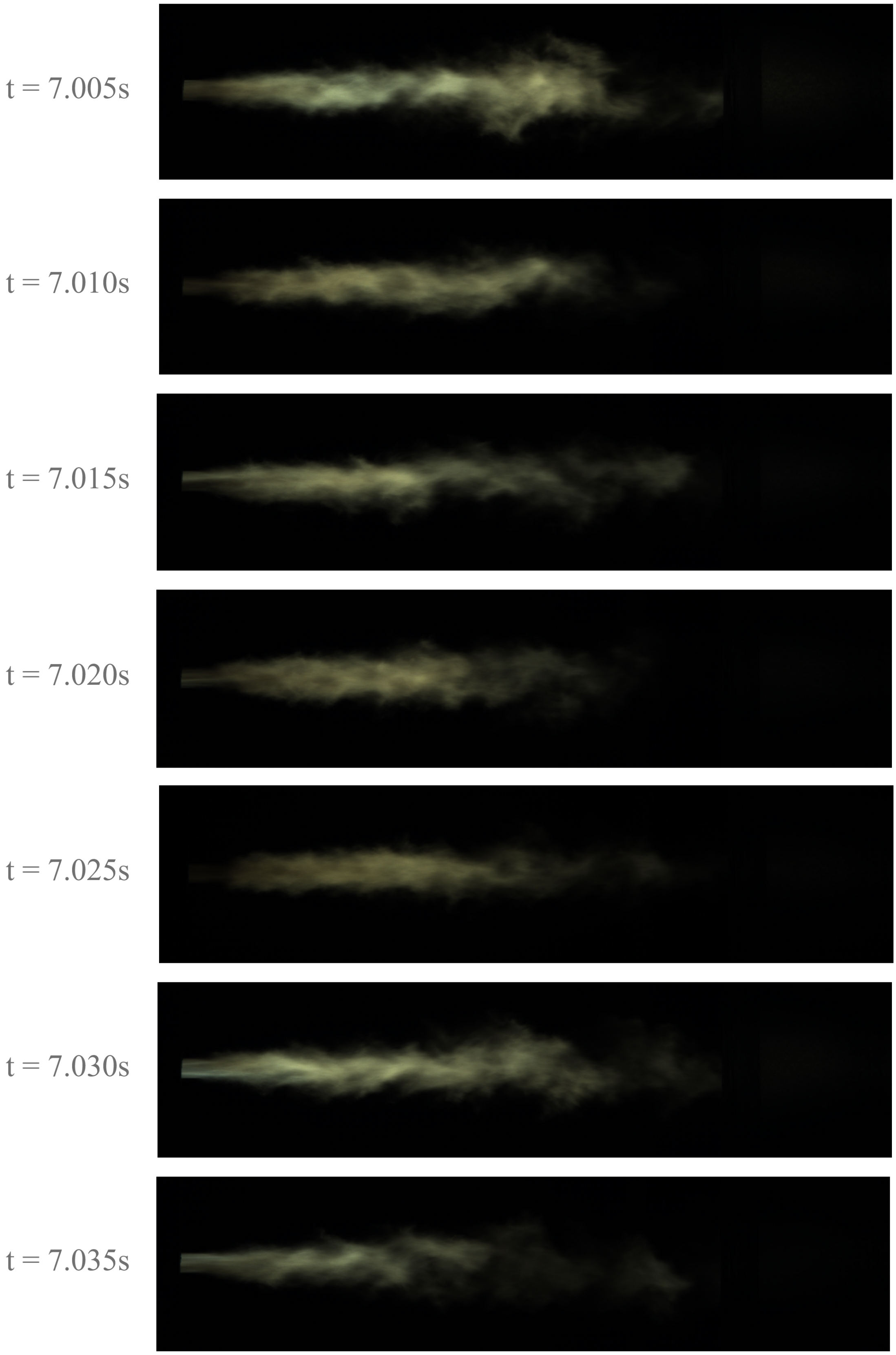

t = 7.005s

t = 7.010s

t = 7.015s

t = 7.020s

t = 7.025s

t = 7.030s

t = 7.035s

Figure 3.11: Exhaust plume frame captures of baseline a ABS fuel grain at $\dot{m}_{ox}$ = 15.3 g/s from t = 7 seconds relative to ignition start at t = 0 seconds. Basic white balance corrections were applied from sample testings prior to static test fire.

Chapter 4

Methodology

The experimental and analytical methodologies used to investigate the proposed 3D printed ABS-paraffin fuel grains influence on engine performance will be covered in this chapter. Performance metrics such as combustion efficiency and specific impulse are calculated using data collected and recorded at the test facility specified in Chapter 3. Performance parameters allow us to construct a more comprehensive understanding of the performance of these ABS-paraffin fuel grains in comparison to baseline ABS and paraffin fuel grains, theoretical results, and literature.

This chapter is divided into four sections: theoretical performance predictions using Chemical Equilibrium Analysis (CEA), the design of the fuel grains used in the experimental campaign - with a particular emphasis on the design and manufacture of the ABS-paraffin fuel grains, regression rate inference from static fire testing, and performance metrics such as combustion chamber pressure, thrust, and combustion efficiency.

4.1 3D Printed ABS - Paraffin Fuel Grains

As discussed earlier in Chapter 2 on liquid layer dynamics, combustion can be defined as dominated by wave-like structures (Petrarolo et al., 2018) . The fuel viscosity and oxidiser mass flow determine the most excited frequencies and wavelengths that characterise the dynamic structure of the liquid layer. The physical behaviour of the liquid layer on a flat paraffin slab is described by these observations, which show convergence towards shorter wavelengths for higher oxidiser mass fluxes. On the other hand, these dynamics can be used to help develop a performance-enhancing ABS-Paraffin fuel grain, with the ABS three-dimensional structure constructed to target the precise wavelengths experienced at the specified oxidiser mass flow rate. By amplifying the liquid layer wavelength and accelerating droplet entrainment through the primary break-up stage and into the secondary break-up stage, the structure beneath the liquid layer, when properly matched to the oxidiser mass flow, can induce more significant Kelvin-Helmholtz instabilities. A method to achieve this could be through modifying the solid structure below the liquid layer, i.e. the fuel grain surface.

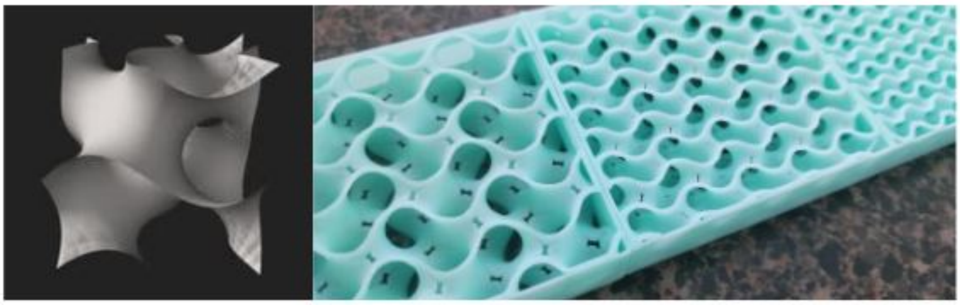

Figure 4.1: (Left): Single gyroid unit cell. (Right): 3D printed gyroid samples at different infill percentages.

4.1.1 3D Printed ABS Gyroid Infill Structure

A practical method to achieve this fuel grain design is to 3D print internal wave-like structures as a shell and then pour paraffin into the grain. 3D printing slicing software, a program used to instil algorithms for the 3D printer to follow layer-by-layer, automatically converts 3D volumes to hollow ones. Interior structures, such as internal walls, can partially fill the hollow item to provide additional robustness. The density of these structures is known as infill density, and it is one of the parameters that must be submitted to the slicer; these structures range from lattice to gyroid structures, each with its benefits and optimal use case.

For this study, the gyroid infill structure has been chosen as the wave-like structure embedded in the paraffin to amplify entrainment. The gyroid is an open cell that is simple to print and is a triply periodic minimal surface, which means it is a surface that minimises its area locally (Schoen, 1970) . Because of its triply periodic structure has a uniform geometry, which reduces anisotropy in mechanical properties and prevents stress concentrations or non-uniform density along the exposed surface of the fuel grains. The gyroid surface can be described as (Wohlgemuth et al., 2001) :

$$sin(\frac{2\pi x}{L})cos(\frac{2\pi y}{L}) + sin(\frac{2\pi y}{L})cos(\frac{2\pi z}{L}) + sin(\frac{2}{L})cos(\frac{2\pi x}{L}) = 0 \tag{4.1}$$

Where L is the cubic unit cell edge length, the gyroid cell formed due to this expression can be seen in figure 4.1. The solid lattice is created by associating a thickness d with the gyroid surface. The thickness of the gyroids surface is governed by the printer's nozzle diameter and layer thickness determined in the slicer settings, which was 0.4mm and 1 layer thickness, respectively.

3D printers have a significant advantage over the more traditional manfucatures methods seen in fuel grain production, such as casting or machining, and it is its ability to produce complex 3d geometries with intricate and controllable cavities, where the traditional methods of manufacture are limited. 3D printers are capable of printing a wide range of materials, the vast majority of which are thermoplastics and typically come in the form of filament spools. These filament spools are essentially lengthy strands of plastic, and for this study, a high-grade filament with more consistent and uniform thicknesses over the entire length of the spool is used. Of these materials, Acrylonitrile Butadiene Styrene (ABS) has a number of mechanical features that make it a viable candidate for hybrid rocket fuel. ABS may be moulded into various geometries utilising modern additive manufacturing and fast prototyping processes, allowing intricate high-surface-area flow paths to be embedded inside the fuel grain. Since ABS regresses at a slower rate than that of paraffin wax, the resulting surface layer would comprise of small ABS protrusions - these protrusions can then act as vortex generators to aid in the break-up of droplets entrained from the paraffin liquid layer.

Finally, ABS has a high tensile yield strength (40 MPa) and structural modulus (2.3 GPa). This yield strength is equivalent to around 38% of aluminium. ABS seeding material's relative strength and insulating qualities allow the fuel grain to take a large percentage of the combustion chamber pressure load, reducing the wall thickness requirements in any design consideration. ABS gyroid structures have been used in the literature as a reinforcing or armoured fuel grain concept (Bisin et al., 2019) , with the emphasis on overcoming paraffin's brittle quality rather than its impact on thermodynamic performance during combustion.

4.1.2 Fuel Grain Paraffin Casting

The ABS-paraffin fuel grains are made by pouring molten paraffin into a 3D printed ABS shell. The cooling process is the primary source of concern when manufacturing paraffin fuel grains (Piscitelli et al., 2018) . Because paraffin shrinks as it cools, some method of reducing shrinkage and void formation is required. With this in mind, the casting process is relatively straightforward. ABS shells are 3D printed in bulk prior to casting for more efficient manufacture. The complete procedure is given in the safe work instructions (specified in Appendix B); however, a brief outline of the process will be described here.

KunLun fully refined paraffin wax 58/60 was purchased in the form of large slabs. When melting the paraffin, a controlled hot plate is employed to ensure the paraffin does not boil and to maintain a molten temperature below that of the glass transition temperature of ABS. By doing so, we ensure that the ABS shell does not deform when the paraffin is poured. Once fully melted, the paraffin is poured carefully into the ABS shells and shaken lightly by oscillating the fuel grain during the initial phase of the pour to ensure the molten wax filled the ABS shell completely and reduce bubbles. To further prevent voids throughout the fuel grain, the grain is cooled in a temperature-controlled incubator to slow the cooling process at least twice as slow than room temperature cooling, in order to observe any statistically significant difference in the reduction of void formation (Chala et al., 2015) - Chapter 4 will discuss the results of void formation in greater detail.

4.2 Experimental Campaign

The hypothesis lies in the ability to amplify the liquid layer wavelength by matching the frequency experienced for the given oxidiser mass flow rate. This should increase the liquid layer wave amplitude, and following from Ishii and Grolmes (1975) inception criteria for entrainment, a rolling wave should be promoted. With this type of entrainment mechanism, the turbulent gas flow is expected to shear the tops of large amplitude roll waves away from the wave crests (figure 2.3). Against the retaining force of the liquid surface tension, the drag force acting on the wave tops deforms the interface into small droplets and entrained into the core gas flow (Ishii and Grolmes (1975) . The increase in entrainment

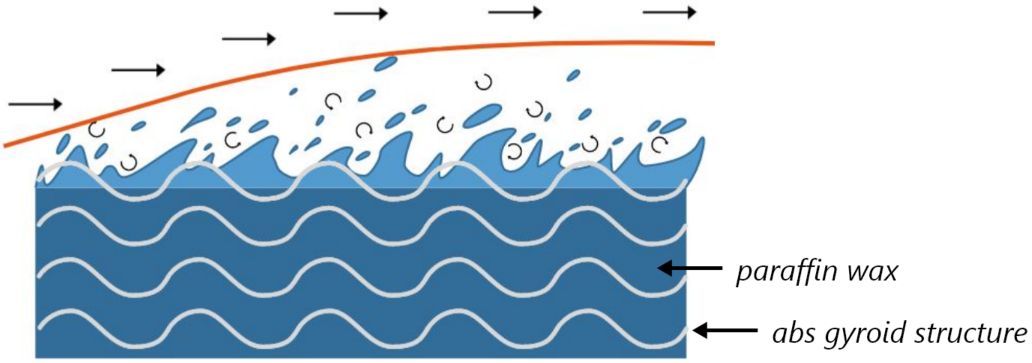

Figure 4.2: Conceptual schematic of the effect of the ABS gyroid infill structure to amplify liquid layer instabilities.

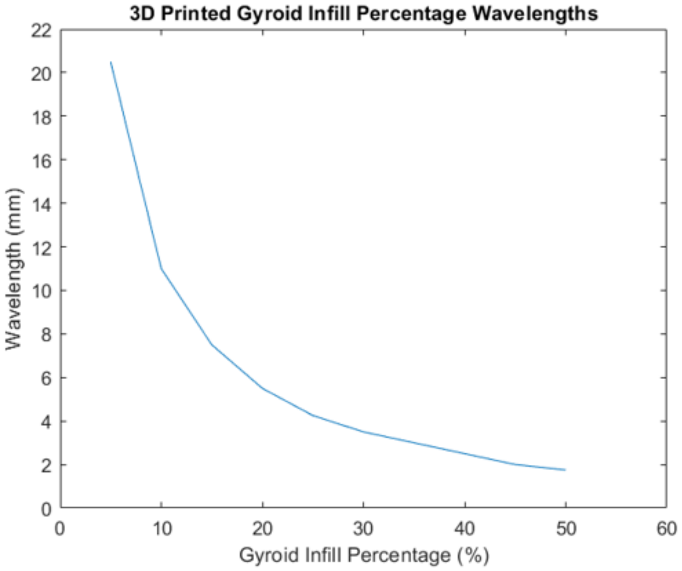

Figure 4.3: Gyroid wavelengths over a range of infill percentages.

resulting from amplifying the liquid layer wavelength should see improvements to regression rate, combustion efficiency and the thrust produced from the engine. A conceptual schematic can be seen in figure 4.2.

The experimental campaign comprises three different fuels grains, pure paraffin wax, pure ABS, and ABS-paraffin, tested at three different oxidiser mass flow rates each, 7.7 g/s (5 bar oxidiser feed pressure), 10.7 g/s (7 bar oxidiser feed pressure) and 15.3 g/s (10 bar oxidiser feed pressure). The concept behind this campaign is to assess the performance of the ABS-paraffin fuel grain at a designed mass flow rate, in this case at 10.7 g/s. The process for each fire will follow the flow of processes as outlined in Chapter 3 (figure 3.8). From figure 2.8, it is suggested that at an oxidiser mass flow rate of 10 g/s, we should observe liquid layer wavelengths of around 3.75 - 3.5mm. Figure 4.3 was compiled by measuring a series of sample prints with varying infill percentages from 5-50% and shows that an infill percentage of 28% will produce gyroids with a wavelength to match this. As a result, we should observe contrasting performance outputs at 'sub-optimal' oxidiser mass flow rates for this fuel grain. When the oxidiser mass flow rate is less than 10 g/s, the liquid layer instability wavelength is larger than the structural wavelength of the gyroid infill; when the oxidiser mass flow rate is greater than 10 g/s, the liquid layer instability wavelength is smaller than the gyroid wavelength.

4.3 Chemical Equilibrium Analysis: CEA

A preliminary chemical equilibrium study is used to assess the theoretical performance of ABS-Paraffin fuel grains compared to base paraffin and base ABS formulations. The chamber properties and performance characteristics for a range of formulations ranging from pure paraffin (0% ABS infill) to pure ABS (100% ABS infill) are determined using NASA's chemical equilibrium code CEA (Chemical Equilibrium with Applications) more straightforward (McBride, 1994) .

Chemical equilibrium is commonly defined by two formulations: equilibrium constants or free energy minimisation. Zeleznik and Gordon (1968) compare the two formulations in their reports and shows that the two formulations reduce to the same number of iteration equations. On the other hand, the minimisation-of-free-energy method allows each species to be treated individually without describing a set of reactions in advance, as is required with equilibrium constants. As a result, the CEA program employs the minimisation-of-free-energy concept, as described in Chapter 3 of this thesis.

The technique for this computation is based on the premise that both liquid and solid phases are all pure. As a result, there is a chance to encounter a phase transition between solid and liquid (melting points) or between two stable solid phases, such as the case for paraffin wax fuels. Because three phases of the same species, one gaseous and two condensed, coexist at such transitions, they are known as triple points. The vapour pressure and temperature of such triple points are fixed, regardless of the relative proportions of each phase. The program may create equilibrium compositions with one or two phases of a species and with or without the gas phase. When the temperature is allocated, there are no questions about which of a species' two or more phases should be regarded. When the temperature is a variable, as it is in combustion or rocket problems, various options must be explored. Two possibilities arise if the program considers a liquid phase and the temperature at convergence is below the melting point, T_m.

4.3.1 CEA Parameters

4.3.1.1 Conservation Equations

A variety of assumptions are made while calculating theoretical rocket performance. Theoretical performance can vary depending on which assumptions are employed for propellant and operational conditions. It assumes one-dimensional flow and applies the conservation of energy and momentum equations. Within the combustion chamber, the program assumes complete combustion, homogeneous mixing of propellants and isentropic expansion through the nozzle.

4.3.1.2 Specific Impulse

Specific impulse is typically defined as the force produced per unit of both oxidiser and fuel mass flow rates (i.e. the total mass flow a the exit of the nozzle) used to produce that force (equation 5.4) -

essentially, how efficient the engine can produce thrust.

$$I_{sp} = \frac{F}{\dot{m}} = \frac{(P_e - P_a)A_e}{\dot{m}} \tag{4.2}$$

Where F is the thrust produced, $\dot{m}$ is the mass flow rate, P_e and P_a is the pressure at the exit and the ambient pressure respectively, and A_e is the exit area.

When the exit pressure is equal to the ambient pressure, the expression used in CAE is described as:

$$I_{sp} = \frac{u_e}{g_e} \tag{4.3}$$

Where in this case, the velocity of the gas at the exit is denoted u_e and the acceleration due to Earth's gravity is g_e . In most cases, this method of calculation wont be used in cases where the thrust and mass flow rate are easily attainable and instead should be used as a theoretical indication.

4.3.1.3 Characteristic Velocity

The characteristic velocity (c*) is a measure of the combustion performance of a rocket engine independent of nozzle performance and can be defined as:

$$c^* = \frac{P_c A_t g_c}{\dot{m}} \tag{4.4}$$

Where P_c is the combustion chamber pressure and A_t is the nozzle throat area and assumes the flow is choked at the nozzle. CAE computes the theoretical c* ($c*_{theoretical}$) and is typically higher than the actual c* ($c*_{actual}$).

4.3.1.4 Thrust Coefficient

The thrust coefficient, C_F, measures how much the nozzle amplifies the thrust and describes chamber pressure and throat area. The thrust per unit combustion chamber pressure and nozzle throat area are the factors to consider.

$$C_F = \frac{F}{P_c A_t} \tag{4.5}$$

Where P_c is the combustion chamber pressure and the same assumptions for a choked flow apply here at the nozzle throat. Taking into account expressions for characteristic velocity and specific impulse, CAE computes the C_F with the expression:

$$C_F = \frac{u_e}{c^*} \tag{4.6}$$

Where the u_e is the exhaust velocity and c* is the characteristic velocity.

4.4 Regression Rate Inference

The most significant feature of hybrid rocket fuels is their regression rate, and a comprehensive characterisation of that quantity as a function of all the major operational factors of the hybrid motor is

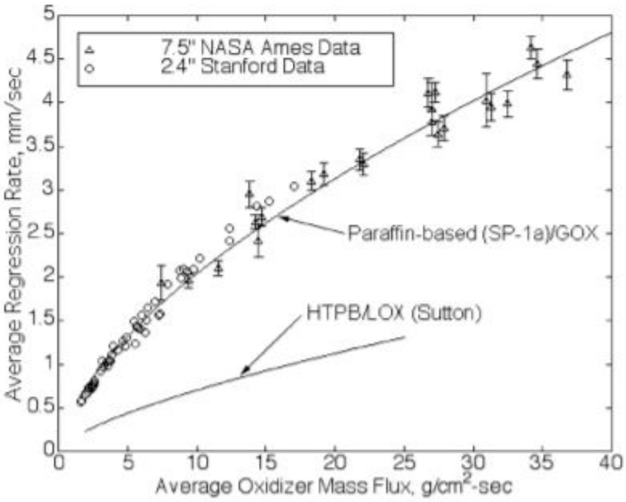

Figure 4.4: Regression rate vs oxidiser mass flux data for paraffin based fuels. (Karabeyoglu et al., 2003)

critical for the successful design of a practical system.

Karabeyoglu et al. (2003) explored the regression rate of paraffin wax with gaseous oxygen and produced a data set of average regression rate as a function of average oxidiser mass flux, seen in figure 4.4. They further noted that a low mass flux is desired to reduce the extent of O/F shift over the burn duration, discussed earlier in Chapter 2, improving the I_{sp} of the system (Karabeyoglu et al., 2003) . In comparison, the regression rate for HTPB with liquid oxygen is also plotted in figure 4.4.

The space-time averaged regression rate for a specific test can be calculated by using the initial port diameter measurements and consumed fuel mass. In the calculations, the following relationships are used:

$$\dot{r}_f = \frac{d_{vc} - d_i}{2t_b} \tag{4.7}$$

$$d_f = \left[{d_i}^2 + \frac{4\Delta M_f}{\pi \rho_f L_g} \right]^{0.5} \tag{4.8}$$

Here, d_{vc} is the diameter of the fuel port after the burn, once thrust is terminated, d_i is the initial diameter, d_f is the final diameter after the burn time, denoted t_b. ΔM_f denotes the total mass of the fuel burned, calculated as the difference between two weight measurements taken before and after the test, and L_g denotes the length of the fuel grain. The regression rate, in terms of mm/s can then be found by taking the difference in diameter divided by the total burn time. The density of paraffin wax and ABS is taken from manufacturers chemical data sheets and the overall density for the ABS-paraffin fuel grains is based on the percentage infill of ABS relative to paraffin wax.

The regression rate can also be expressed as kg/s, representing the mass flow rate of fuel (equation 5.11) by taking the difference in mass from its initial state, prior to hot fire, and the final mass, after hot fire, over the total burn time. This allows for the calculation of the total mass flow rate within the combustion chamber as well as being an indicative measure for the rate of droplet entrainment and evaporation.

$$\dot{m}_f = \Delta M_f = \frac{(m_{initial} - m_{final})}{t_b} \tag{4.9}$$

This expression for regression rate will be used in the calculation of performance parameters discussed in the next section of this chapter.

4.5 Performance Parameter Analysis

4.5.1 Combustion Efficiency

The performance of any rocket engine system is comprised of various components that add up within the system, such as optimal nozzle and injector design, managing combustion temperature and pressure etc. However, those metrics are synonymous with all rocket systems; what differentiates a hybrid rocket engine and all other engines is its combustion process. In order to adequately assess the performance of different fuel grain configurations, we look at measuring the combustion efficiency - a parameter that looks at how efficiently the fuel is able to add energy into the

The combustion efficiency (also referred to as characteristic velocity efficiency) is but a ratio of the actual recorded characteristic velocity over the theoretical characteristic velocity, as expressed in equation 5.6. The primary assumption here is that CEA assumes that the concentration of reactants and products is invariant with time, and therefore no observable properties change. Once that is computed, the actual characteristic velocity can be found through measurements of combustion chamber pressure at the post-combustion chamber region and the nozzle throat area, and the average mass flow rates accounted for indirectly through measurements pre and post-burn. The two are then used to find the combustion efficiency, i.e. how close the actual engine performs relative to its theoretical potential.

$$\eta_{c^*} = \frac{c^*_{actual}}{c^*_{theoretical}} \tag{4.10}$$

In the case of hybrid rocket engines and regression rate measurements, there is no single industry standard practised to determine the combustion efficiency of a hybrid rocket engine. The approach to measuring the characteristic velocity can lead to erroneous results dependant on the specific location of the combustion chamber pressure measurement. Therefore, the combustion efficiency should be used as simply an indication relative to the fuel grains tested under the same conditions. However, in the case of this study, combustion efficiency is used as a suitable base characteristic to determine the effectiveness of the fuel grains tested in comparison to conventional fuel grain designs where a higher-performing fuel grain design should exhibit higher combustion efficiencies in practice, all under the same conditions, for example, the same chamber pressure measurement location, ignition system and oxidiser inlet conditions.

4.5.2 Thrust Coefficient

The thrust coefficient is a significant parameter when it comes to determining the increase in thrust due to the expansion of the gas in the nozzle as opposed to the forces of combustion chamber pressure acting over the nozzle throat area alone. As stated earlier in Chapter 3, a converging nozzle is used to avoid biased results - since each fuel grain is expected to produce different chamber pressures, where, if aligned, a particular fuel grain may produce higher levels of thrust due to its compatibility with the nozzle and therefore skewing the results in that grains favour. The converging nozzle will also considerably lower the actual thrust produced by the engine since the exhaust gases do not accelerate past Mach 1 after the nozzle throat. So, in essence, the thrust coefficient allows calculating a theoretical thrust produced for a rocket engine with a well-designed converging-diverging nozzle from the data collected in this study.

It is more straightforward for static test firing experiments to redefine equation 5.7 with the following:

$$C_F = \frac{F}{p_c A_t} \tag{4.11}$$

The robustness of the graphite nozzle minimises any change to the throat area over the burn. Therefore, the throat area is a constant. Calculating the thrust coefficient with real-time thrust and combustion chamber data will allow us to compare and contrast the thrust performance for each fuel grain over the duration of the burn.

Chapter 5

Results and Discussion

By analysing the performance of pure paraffin, pure ABS and gyroid ABS-Paraffin fuel grain formulations, this project seeks to compare the performance output of each grain in terms of thrust and pressure to see if the gyroid structure can enhance regression rate by exciting the KHI in the liquid layer for liquefying fuel grains. Specific impulse and thrust coefficients are employed as non-dimensional parameters to better compare the results of this study with literature and other experimental data-sets.

The following chapter investigates these phenomena by evaluating the earlier mentioned performance metrics for the three fuel formulations across different oxidiser mass fluxes. Chapter 6 hypothesises that for a targeted mass flow rate, the gyroid infill pattern can excite the frequencies exhibited by the Kelvin-Helmholtz instability, surmounting to improved fuel regression (Petrarolo et al., 2018). Although the mechanism cannot be observed directly with the facility developed, this chapter examines the effect of the gyroid infill captured in the performance data. If more fuel is instantaneously burnt, it should be reflected in more thrust, and higher chamber pressures (Cantwell et al., 1978).

5.1 Presentation of Results

5.1.1 Preliminary CEA Analysis

The I_{sp} and thrust coefficients were calculated using CEA for fuel grain formulations ranging from pure paraffin (100% paraffin wax) to pure ABS (0% paraffin wax and 100% ABS) with progressive increases in ABS density (i.e. the percentage of ABS present, with the remainder being made up of paraffin wax). The density of ABS in these fuel grains are controlled via its print infill percentage - in this case, it represents the percentage of ABS in the grain relative to the amount of paraffin. In a pure chemical sense, these scenarios were able to create a relative image of the performance of the fuel grain based on ABS infill percentage. While we cannot directly model the performance of these grains, we can see that changing the ABS and paraffin content of the fuel does not affect the engine's performance when looking at equilibrium combustion (figure 5.1). As the ABS infill percentage increases, there is a modest increase in combustion temperature and, as a result, thrust coefficient. In contrast, as the ABS infill percentage increases, the characteristic velocity and specific impulse decrease slightly. This shows that ABS can generate higher combustion chamber temperatures to heat and expand the gas, but paraffin

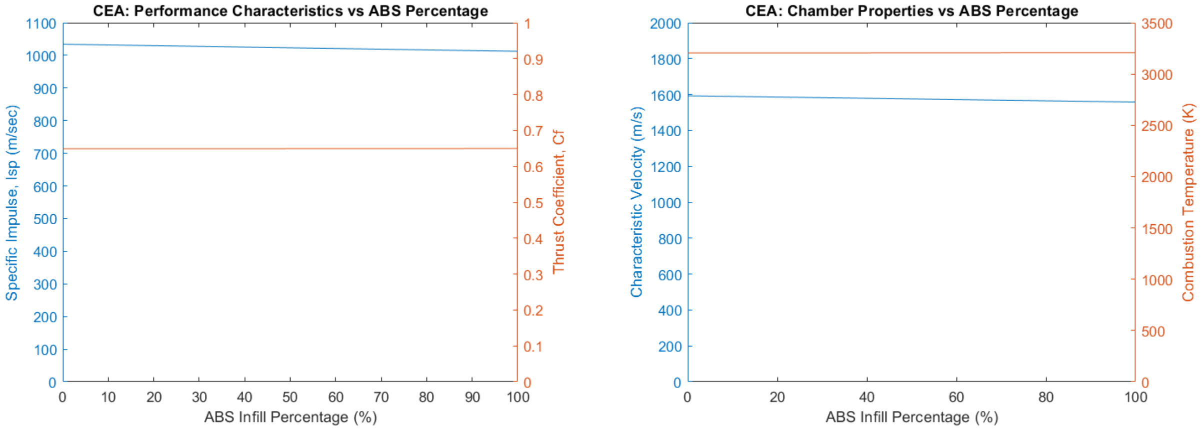

Figure 5.1: Using CEA: (Left) Performance Characteristics vs ABS infill percentage. (Right): Combustion Chamber Properties vs ABS infill percentage.

can provide more efficient combustion by generating higher pressures per unit of fuel mass expended. Despite these findings, the proportional importance of these differences is negligible for the purposes of this study, and the results of the experimental campaigns show that the discrepancies are primarily attributable to the mechanisms of boundary layer combustion for liquefying and non-liquefying fuels.

5.1.2 Repeatability of Fuel Grain Manufacture

For the pure paraffin and ABS-paraffin fuel grains, the production procedure comprises pouring molten paraffin wax into a 3D printed ABS fuel grain shell as discussed in Chapter 4. As evidenced in CT scans (figure 5.2) and post-fire cross-sections of the ABS-paraffin fuel grains (figure 5.13), the ABS-paraffin fuel grains had minimal voids, especially at higher percentage infills (10% and above) where there is more surface area for the paraffin to attach onto during solidification. On the other hand, pure paraffin fuel grains require more attention after the molten paraffin has been set to avoid voids and fissures; in this case, the fuel grains were shaken slightly during the pour and cooled overnight in an incubator to reduce the temperature gradient during the cooling process.

We can see from table 5.1, pure paraffin fuel grains exhibited maximum deviations of up to 1.72%, a significant improvement from the 15% observed preliminary grain manufacture tests - where none of the above mentioned processes were employed. ABS fuel grains saw a maximum deviation of 0.36%, and the ABS-paraffin fuel grain had a maximum deviation of 0.39%. The quality of pure ABS and ABS-paraffin fuel grains, in particular, is reliant on the repeatability and accuracy of the 3D printer. As a result, the variance in fuel grain manufacture can vary depending on the quality of the 3D printer used and the ABS filament grade. Similar to the pure paraffin instance, where paraffin waxes can shrink by up to 17% depending on the grade of paraffin wax used, notwithstanding the techniques taken to minimise the development of voids and fissures (Karabeyoglu et al., 2003) . It is safe to claim that the criteria for repeated and dependable tests have been met since all fuel grains were reported to be within ±2% of their average recorded mass.

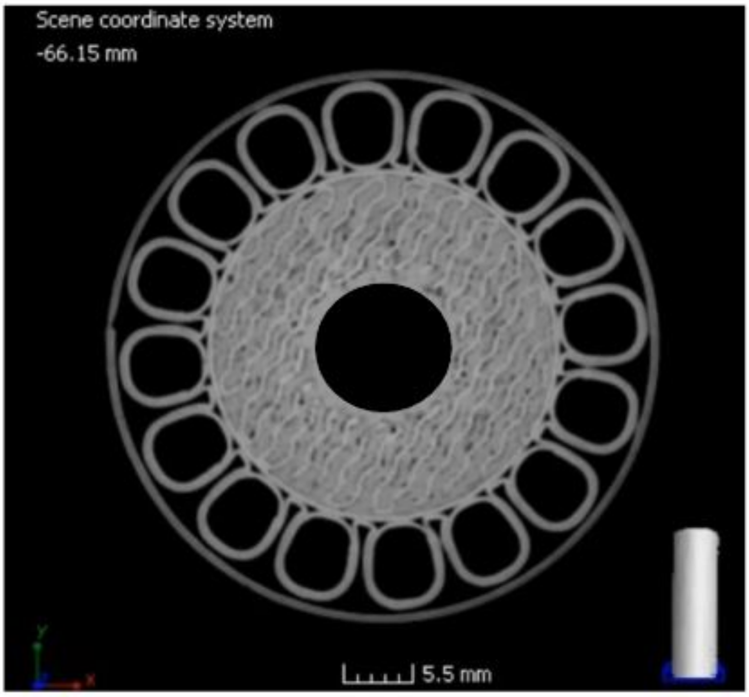

Figure 5.2: CT scan of ABS-paraffin fuel grain cross section normal to the axis of the fuel port. The ABS gyroid structure can be seen as lighter compared to the paraffin wax.

Fuel	$m_{initial}$ (g)	σ_{mass} (%)
Paraffin Wax	818.4	-1.15
Paraffin Wax	837.5	1.15
Paraffin Wax	813.9	-1.69
ABS	1049.1	0.23
ABS	1044.1	-0.23
ABS	1042.7	-0.37
Gyroid ABS-Paraffin	860.5	-0.31
Gyroid ABS-Paraffin	865.9	0.31
Gyroid ABS-Paraffin	865.3	0.24

Table 5.1: Table of fuel grain manufacturing data comprising a sample of each fuel grain tested to show initial mass measured and the deviation from the average for that fuel grain formulation. A complete table of data can be found in Appendix C.

5.2 Repeatability of Hot Fire Tests

The experimental campaign consisted of two key phases: reliability hot fires, and experimental hot fires. The former comprises a series of static test fires with the same fuel grain to establish the degree of error present with the test facility developed for this study. The fuel grains used was a set of baseline ABS fuel grains tested at 10.7 g/cm^2s and 15.3 g/cm^2s oxidiser mass fluxes - with three hot fire tests conducted at each mass flux. The chamber and thrust results for a total burn time of 10 seconds can be found in figure 5.3, where ignition occurs at t=0. In these tests, the oxidiser mass flux was controlled by the upstream pressure from the pressure regulator. Each test was conducted steady ambient temperatures, ranging from 20.5-21 degrees Celsius.

Chamber pressure data show consistent patterns over the three ABS fuel grain tests. Because of the oscillations present in the data, the data was windowed to make the profiles more visible throughout each test, otherwise the raw data will overlap. Although there appear to be some notable slight discrepancies with the pressure gradient midway through the burn, as evident in the first ABS test at 15.3 g/cm^2s ((a) of figure 5.3), the raw data was within ±2% of the baseline average of the three tests. This could indicate that the time it takes to ignite the fuel port entirely is dependent on the installment of steel wool with the e-match, which was discussed in the previous chapter when addressing the ignition system. Because the steel wool mass measurements were within ±5%, these findings could indicate that the ignition charge utilised in the first test contributed to the variance. The thrust data was the most erratic, with oscillations in the data profile that were inconsistent. The average thrust measured for each tested instance was largely similar when the test cases were compared across the two mass fluxes, demonstrating a consistent increase in maximum thrust at the higher mass flow rate compared to the lower mass flow rate.

5.3 Comparison of Measured Performance Metrics

5.3.1 Combustion Chamber Pressure

We first evaluate the pressure data acquired for the pure paraffin and pure ABS fuel grains to validate the experiment and compare the results of baseline paraffin and baseline ABS with those found in the literature. Figure 5.4 depicts the real-time pressure profiles for the two baseline fuel compositions. In theory, the higher regressing pure paraffin fuel grain should perform better than the slower regressing ABS fuel grain (Marxman, 1964) . However, the results appear to contradict this, with ABS fuel grains beating paraffin by a large margin at low oxidiser mass fluxes - and it is only at 15.3 g/cm^2s that we can witness more comparable performance between these two fuel compositions. Despite contradicting the assumption of greater regression rates implying better performance, these findings are expected to be demonstrated in real applications where the efficiency with which the entrained droplets vaporise and supply energy to the system is significant. This follows the suggestion that Whitmore et al (2015) outlined in his critique of liquefying fuel grains, in which he indicates significant unburned material ejecting from the engine exhaust - leading to the suggestion that combustion efficiencies in paraffin-based fuel grains are inherently lower (combustion efficiencies will be explored in greater detail later in this chapter).

Between those in this study and the profiles seen in Wang et al (2020) , we can observe a similar trend at the beginning of the burn - where there is a slight drop in chamber pressure in the first few seconds. Figure 5.5 showcases the key peaks present in the data from a sample of the experimental data, with the intent to provide a clearer view of the phenomenon seen in the large majority of test runs. This particular phenomenon was not discussed in significant detail in the literature, however, it could be

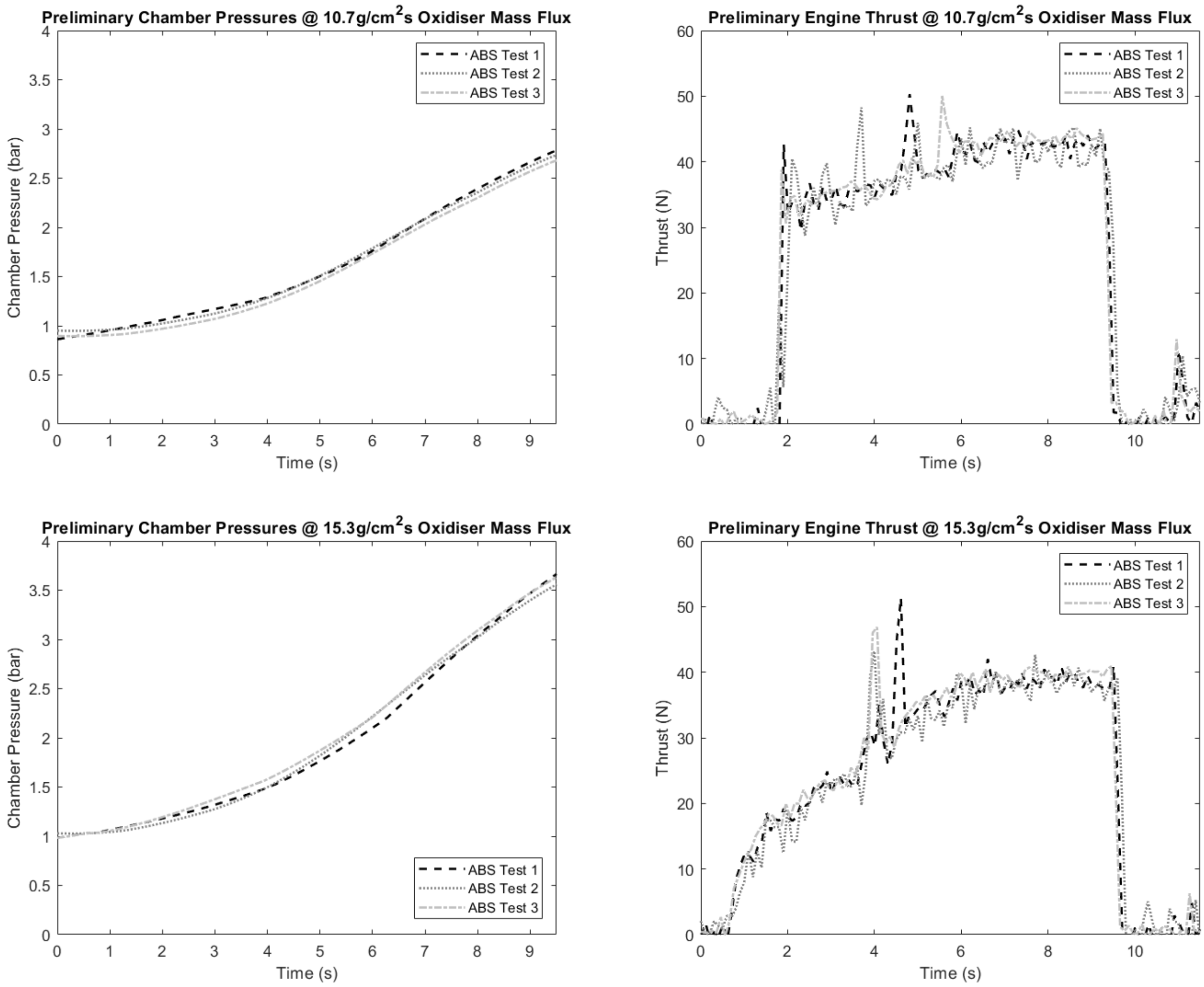

(a) Preliminary Chamber Pressure Data

(a) Preliminary Engine Thrust Data

Figure 5.3: Preliminary measurement data of (a) chamber pressure and (b) engine thrust at 15.3 g/cm^2s (@ 7bar oxidiser inlet pressure) and 10.7 g/cm^2s (@ 10bar oxidiser inlet pressure) oxidiser mass fluxes. Note that the pressure fluctuations in the chamber have been windowed to make the variance in the pressure profiles more visible.

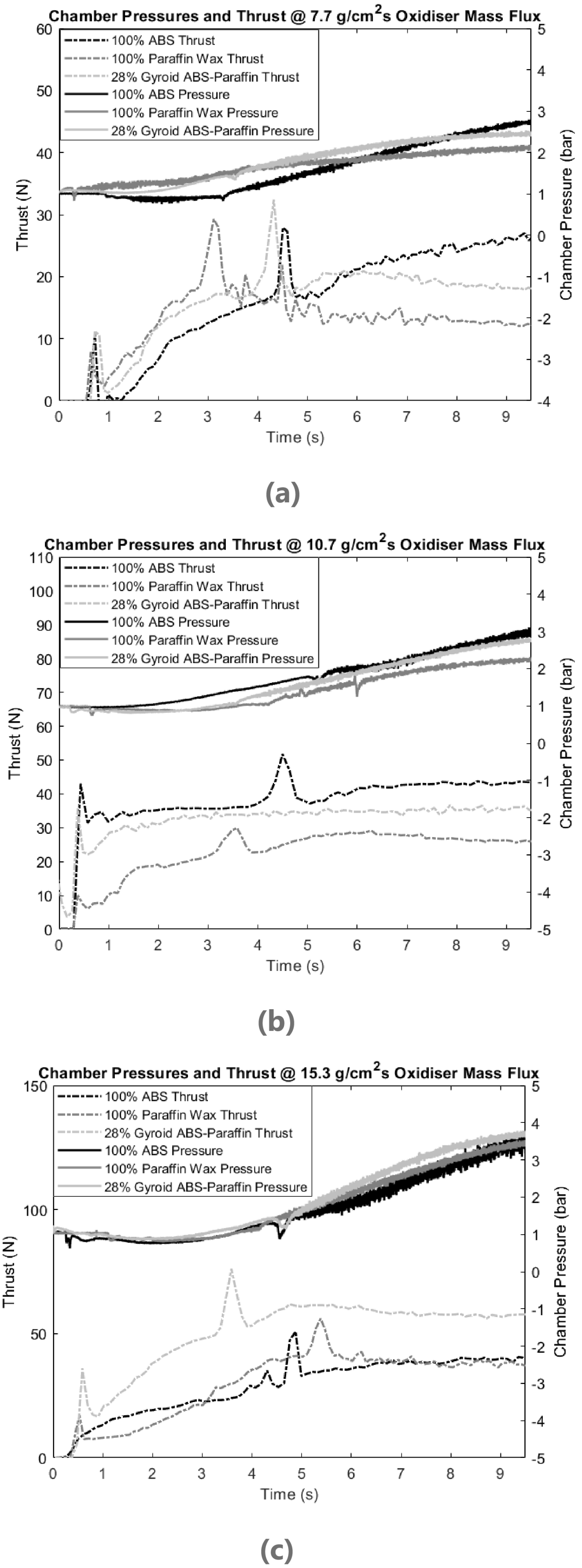

Figure 5.4: Chamber Pressure and Thrust profiles for baseline ABS, Paraffin and Gyroid fuel grains over t_{burn}=10s, where ignition occurs at t=0s. (a) 7.7g/cm^2s @ 5bar oxidiser inlet pressure (b) 10.7g/cm^2s @ 7bar oxidiser inlet pressure (c) 15.3g/cm^2s @ 10bar oxidiser inlet pressure

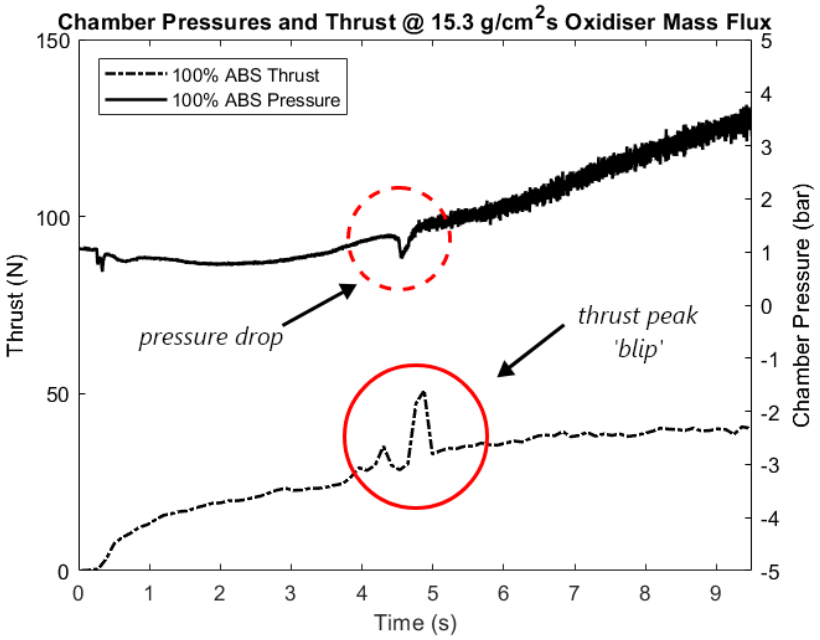

Figure 5.5: A single sample from the experimental campaign of a baseline ABS fuel grain pressure and thrust profile at 15.3 g/cm^2s oxidiser mass flux. Highlighting key features present in a large majority of the fuel grains.

suggested that the cause of this slight drop is due to the ignition process in association with the scale of the engine. This pressure drop could represent the length of time it takes to fully burn the entire length of the fuel port after ignition. If we recall the conservation of energy as discussed in Chapter 2, a drop in pressure could be attributed to an acceleration in the absence of combustion, where for a brief moment, the combustion process is 'flamed out'. The conditions which would cause this to occur is still not completely clear with the data and observations obtained from this study.

When observing the pressure profiles across all three mass fluxes, there exists some inconsistency. For example, in figure 5.4 (a) we see a dip in pressure for the ABS and gyroid fuel grain, but not an elongated dip for the pure paraffin case, instead, we observe a short downward spike. This suggests that despite the consistent ignition of the e-match and steel wool, what fuel grain is used also plays a significant role in the initial behaviour of the burn. From the data collected it is difficult to confidently decipher what could be the cause of this, however it suggests that pure paraffin propagates the flame significantly faster than fuels that include ABS during the ignition phase. The nature of paraffin liquefying and the relatively low temperatures that are needed to do so could be the cause of what is being exhibited here. However, at higher mass fluxes, as seen in the 10.7 and 15.3 g/cm^2s cases, we no longer see that behaviour - leaning towards the notion that in the low mass flow rate case, the O/F ratio is in chaotic flux after ignition due to the low rate of oxidiser - however, further investigations may need to be required to confidently determine the cause of this behaviour.

The sharp pressure drop is then followed by a change in pressure gradient and a change in the magnitude of pressure oscillations measured by the sensor. When compared to the chamber pressure profiles in the literature (Wang et al., 2020; Wu et al., 2018; Whitmore et al., 2015) , it seems this

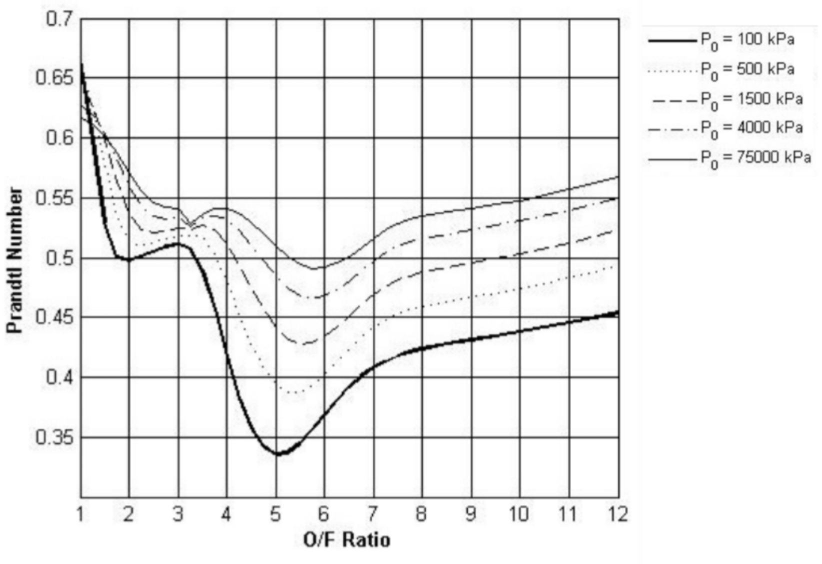

Figure 5.6: Theoretical Prandtl number over varying O/F ratios for a paraffin based fuel. (Eilers and Whitmore, 2008)

particular phenomenon is isolated to this study. Most exhibit trends of a sharp spike in pressure after ignition, and then a relatively constant pressure curve is exhibited thereafter. It may be argued that this is owing to the test facility's relatively larger scale compared to the literature, where significant fluctuations in O/F ratios could result in a more significant instantaneous pressure differential. This could signal that the engine had switched from an oxidiser-rich to a fuel-rich combustion mode. Similar behaviour was seen by Whitmore and Merkley (2019) , who observed a fuel-rich regressive burn pattern. Unfortunately, there is insufficient data to confidently determine the cause of this decline.

We can consult dimensionless variables relevant to understanding the internal mechanics taking place within the combustion chamber to further analyse the likely reason for this pressure drop. Because the mixture of fuel and oxidiser in hybrid rocket engines is constantly changing, the profile over a variety of O/F ratios is of special importance. The Prandtl number, one of the main thermodynamic parameters of importance in hybrid rocket performance, exhibits peaks across the O/F spectrum (figure 5.6, potentially indicating a correlation between this peak in Prandtl Number and the pressure decrease noted in the data.

The propellant mixture ratio and chamber pressure have a significant impact on the mean gaseous products within the chamber of the hybrid rocket. Over the engine's operating range, a 50–100% variance in turbulent Prandtl number can be seen (Eilers and Whitmore, 2008) . In a viscous flow environment, the Prandtl number is a measure of the relative importance of skin friction and heat transfer. The Prandtl number for laminar flow-fields can range from virtually zero to more than 1000. Its value is limited to less than unity for turbulent flow-fields. For ordinary pipe flows, the turbulent Prandtl number is approximately constant and ranges from approximately 0.5 to 1.0 depending on the working fluid (Crawford and Kays, 1993) . When observing figure 5.6, we see that there is an optimal mixture ratio, within the vicinity of 6-7. However, most notable is the inflection points seen in the Prandtl number. Eilers and Whitmore (2008) suggest that the cause of this is a result of the highly fuel-rich mixture ratios forming complex molecules in the combustion products. When analysing figure 5.6 as O/F decreases, we move from oxidiser-rich (high O/F ratio), where the exhaust product is almost pure oxidiser, to fuel-rich (low O/F ratio), as the fuel port expands and the surface area of available fuel increases, shifting to a more fuel-rich mixture. We can see a sharp drop in pressure in figure 5.4 follows a similar behaviour seen in the Prandtl number, where there is a sharp drop at around an O/F ratio of 4, and then begins to increase once more. This behaviour suggests a shift in the ratio of the momentum and thermal boundary layers. A fluid with a low Prandtl number has a low kinematic viscosity or a high thermal diffusivity. With the data available in this study, it is difficult to determine which of the two behaviours we are seeing here; however, it can be assumed that in boundary layer combustion, at constant oxidiser mass fluxes, the thermal diffusivity of the fuel increases at that point for a brief moment during combustion, at which point the ratio is tipped past that point of exceptionally high thermal diffusivity. This could imply that the oxidiser-to-fuel ratio at this facility is heavily skewed in favour of fuel.

With the baseline cases validated, we can explore the results of the novel gyroid fuel grain experimented in this study. Focusing on the chamber pressure produced during combustion, we can see clear performance improvements over the baseline paraffin wax fuel grain over the three oxidiser mass fluxes (figure 5.4). At the highest mass flow rate tested, we can observe the novel fuel grain outperforming both the paraffin and ABS based fuel grains. It can be said that the novel fuel grain is able to burn more fuel at any given time when compared to the baseline paraffin fuel grain, with it having both the liquefying nature of the paraffin wax with the steady burn of the ABS gyroid structure. The idea of the ABS structures acting as flow disputers on the liquid layer could potentially be seen in the results seen here, however, its connection to the Kelvin-Helmholtz instability (Petrarolo et al., 2018) is challenging to determine with these pressure measurements. When looking at the chamber pressure at the gyroid fuel grains designed oxidiser mass flow rate, we can see the performance improving in general and reaching higher pressures (with an increase of 0.4bar as opposed to the pure ABS increase of only 0.25 bar and the minimal increase of 0.06 bar for the pure paraffin fuel grain), however that can be explained by the increase in oxidiser pressure entering the chamber. So with chamber pressure alone, it is difficult to determine if the gyroid fuel grain is amplifying the KHI at its designed oxidiser mass flow rate. However, we can confirm an improvement in pressure output with the gyroid fuel grain over the baseline paraffin case.

The maximum pressure for the 14.33 g/cm^2s experiments in Wang et al's study reached around 1.07 MPa (Wang et al., 2020) , almost 10 times the pressures reached in the 15.3 g/cm^2s experiments ran in this study. The pressures used in the oxidiser lines were not disclosed in the article, however, it suggests pressures greater than 10bar. For the purposes of this study, the magnitude of performance is not of particular concern and instead focusing on a fair comparison between the different fuel grains tested, however, it does suggest that the facility could be improved further to increase performance to compare closer to what was exhibited in Wang et al's (2020) study - installing higher pressure rated equipment to allow for greater oxidiser pressures for example.

5.3.2 Engine Thrust

As noted earlier in Chapter 3, the use of a converging nozzle does not produce a lot of thrust, but it does seek to reduce any bias in the results when comparing each test case. Figure 5.4 depicts the average thrust profile for each example at various oxidiser mass fluxes. Similar to the earlier discussed chamber pressure, we can see comparable behaviour amongst the three examples at varying mass fluxes. The ultimate thrust produced depends on the mass flow rate, with higher mass fluxes producing higher amounts of thrust - this is to be expected regardless of fuel. The gyroid fuel grain continues to outperform the baseline paraffin wax fuel grain, and we detect a similar shift in chamber pressure. At the maximum mass flow rate tested, the gyroid fuel grain produces more thrust than the two baseline paraffin and ABS fuel grains, with the paraffin also becoming similar to the ABS fuel grain. This emphasises the importance of larger mass fluxes in order to fully benefit from the liquefying characteristic of paraffin-based fuel grains. The profile of the thrust profiles yields similar results to those found in the literature, where a straight cylindrical port demonstrates steady expansion until the end of the burn. However, when reading contemporary literature that has shown thrust profiles (Whitmore et al., 2015; Lee and Tsai, 2009; McCulley, 2012) , the vast majority reveal profiles that conflict with Hill and Petersons (1992) thrust profile for a cylindrical port. This could be attributed to the relative scales used in each experiment. At smaller diameters, the thrust profile tends to burn for a short period of time, resulting in virtually instantaneous ignition of the whole port of the grain and a negligible difference in surface area of the entire burn. In contrast to large-scale engines with greater diameters, where the shift in O/F ratio is more pronounced, resulting in a progressive increase in thrust over time for a cylindrical port.

A steep peak in thrust is a major feature evident in these thrust profiles (figure 5.4). When we compare the timing of these peaks to the pressure profiles in the combustion chamber, we notice a strong association between these peaks and the pressure drops seen in figure 5.5. The timing of these peaks appears to vary depending on the fuel grain, however, they generally occur between 3-5 seconds. The thrust peaks could be caused by a large pressure differential within the chamber. The thrust is measured by making direct contact between the engine fore-closure and the single-point load cell. A brief drop in pressure could have resulted in a momentum shift prior to the spike. The spike we see here could be the consequence of the entire engine body's momentum carrying through and impacting the load cell. It is difficult to pinpoint the exact source of this surge in thrust because no accounts of this event have been found in literature since the writing of this thesis.

Overall, at all mass fluxes, the gyroid fuel grain surpasses the baseline paraffin fuel grain in terms of chamber pressure and thrust, and when the oxidiser mass flow rate reaches 15.3 g/cm^2s, the gyroid fuel grain begins to outperform the ABS fuel grain as well. To determine why this is the case, we must delve deeper into the data acquired in this study to determine the source of this performance improvement and whether the study's premise can be confirmed.

5.3.3 Regression Rate

This study measured the average regression rate across the whole burn by weighing the fuel grain before and after each static test fire. Figure 5.7 shows the resulting data. For starters, there is a

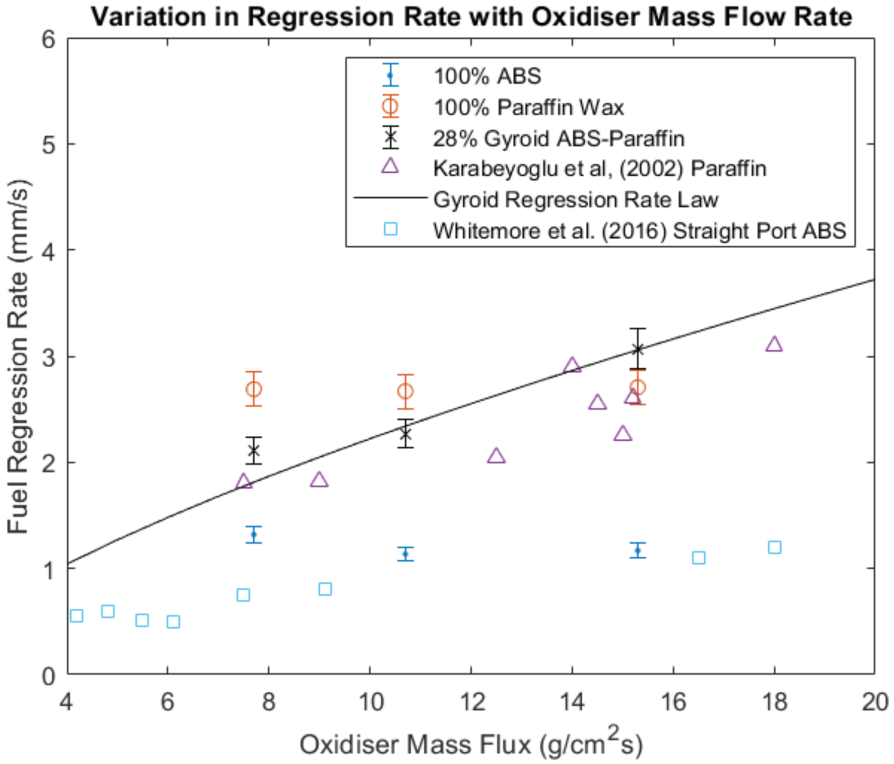

Figure 5.7: Measured average regression rates for baseline ABS, paraffin and gyroid fuel grains over various oxidiser mass fluxes tested. Curve fit expressions for the gyroid fuel grain results in a Marxman regression rate expression of $\dot{r} = 0.488\ {G_0}^{0.69}$. For comparison, regression rate data for ABS (Whitmore et al. (2016) and paraffin wax (Karabeyoglu et al. 2002) are plotted.

significant difference between the baseline pure paraffin fuel grain and the baseline ABS fuel grain. Across the multiple oxidiser mass fluxes, both fuel grains displayed comparable regression rates, with the paraffin fuel grain averaging at around 6.6 mm/s and the ABS fuel grain falling slightly from 3.2 mm/s to 2.6 mm/s. This somewhat contradicts the notion that regression rate scales with oxidiser mass flux (Marxman, 1964) , however, from literature for paraffin-based fuels (Lee and Tsai, 2008; Lee and Potapkin, 2002) and for ABS based fuel grains (Whitmore et al., 2015), we see that the gradient throughout oxidiser mass fluxes is minimal as well. The magnitude of the error associated with each data point indicates that the data is rather consistent, and it is a recurring feature in most experimental literature. When we compare the regression values, we notice comparable results to the literature as seen in figure 5.7, despite the relative variations in scale and operation - implying that the regression rate is more highly influenced by the fuel formulation. Overall, we observe what we would expect from the two baseline fuel grains; but, when we look at the gyroid fuel grain, we begin to notice some unique characteristics.

The regression rate of the gyroid fuel grain exhibits a stronger dependence on oxidiser mass flow rate as opposed to the two baseline cases. If we notion back to the physical phenomena occurring at the liquid layer and its relation to the Kelvin-Helmholtz Instability (Petrarolo et al., 2018) , oxidiser mass fluxes can induce discrete wavelengths in the unstable liquid layer. For the base paraffin case, it suggests a minimal impact on the regression rate, however, when an ABS perturbating gyroid structure is introduced, we see behaviour where the regression rates scale with increasing levels of oxidiser mass flow rate. This could potentially lead to confirming the hypothesis that the perturbating structures, which regress at a slower rate than the paraffin wax, affects the mass flow rate of fuel ejecting from the liquid layer at the surface of the fuel grain.

At oxidiser mass fluxes of 7.7 g/cm^2s and 10.7 g/cm^2s, the gyroid fuel grains outperforms the ABS baseline fuel grain but regresses slower when compared to the paraffin case - until 15.3 g/cm^2s, where we see the gyroid fuel grain reach more comparable levels of regression rate to the baseline paraffin fuel grain. At 7.7 g/cm^2s, the cause for its matching regression rate to ABS could be representative of the wavelength induced by the low mass flow rate to be too large for the gyroid structures wavelength, leading to a cancellation of wave peaks and stabilising the liquid layer. This behaviour was expected since the gyroid structure was targeting a smaller wavelength at 10.7 g/cm^2s. What was interesting to observe was that at 10.7 g/cm^2s, we see an improvement in the gyroid fuel grains regression rate, but it is not enough to outperform the baseline paraffin as expected, instead, begins to show signs of improvement over the baseline at oxidiser mass fluxes of 15.3 g/cm^2s. This could be explained by one of these potential scenarios: the wavelength of the liquid layer at the prescribed mass flow rate for the paraffin used in this study is higher than what was found in Petrarolo et al's (2018) study ; the hypothesis of matching the wavelengths proved disadvantageous, and instead, a gyroid wavelength offset to the liquid layer wavelength produces greater instabilities and liquid layer breakup; or, the gyroid structure is not dependant on the wavelength of the liquid layer, and instead is entirely reliant on a high enough mass flux to amplify liquid layer instabilities.

To confidently obtain an accurate conclusion to this phenomenon, it will require more in-depth research, with an experiment focusing on visualising or obtaining quantitative data on the liquid layer

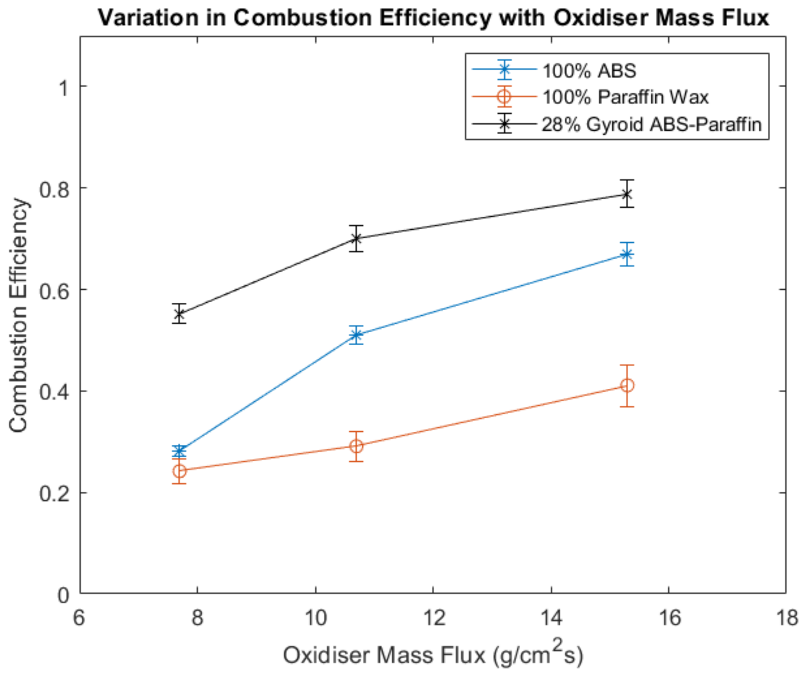

Figure 5.8: Calculated average combustion efficiency for baseline ABS, paraffin wax and gyroid fuel grains across varying oxidiser mass fluxes tested.

dynamics as a result of the gyroid perturbating structure. However, what it does show, is that the regression rate becomes dependent on mass flow rate, as opposed to the two baseline cases where minimal changes to regression rates were observed - possibly suggesting that there is an interaction between the wavelength induced by the flow of oxidiser and the wavelength of the gyroid structure.

5.4 Comparison of Calculated Performance Metrics

5.4.1 Combustion Efficiency

When comparing the regression rate data to the performance output of the engine, higher regression rates are expected to lead to higher levels of thrust and pressure produced. However, we see contrasting results to this expectation - where we see ABS outperforming paraffin wax, despite having half the rate of regression. This leads to the notion that the performance of a fuel grain is not strictly governed by how quickly the fuel can leave its solid surface, but by how efficiently it converts the fuel into energy within the system. The combustion efficiency of an engine can provide some insight into this behaviour. This element is critical in observing the positive effects of the unique gyroid fuel grain presented in this study and to assist in inferring information about the interaction between the liquid layer, the ABS gyroid structure, and boundary layer combustion.

Figure 5.8 shows the calculated average combustion efficiencies (Equation 4.10) for each fuel grain over the range of oxidiser mass fluxes tested. We can observe a clear distinction between the efficiencies for the two baseline fuel grains - where the ABS formulation exhibits more efficient combustion than the pure paraffin formulation. The combustion efficiency of the paraffin wax sample averaged at around 24% at 7.7 g/cm^2s and reached efficiencies of 41% at 15.3 g/cm^2s. The ABS fuel grain, on

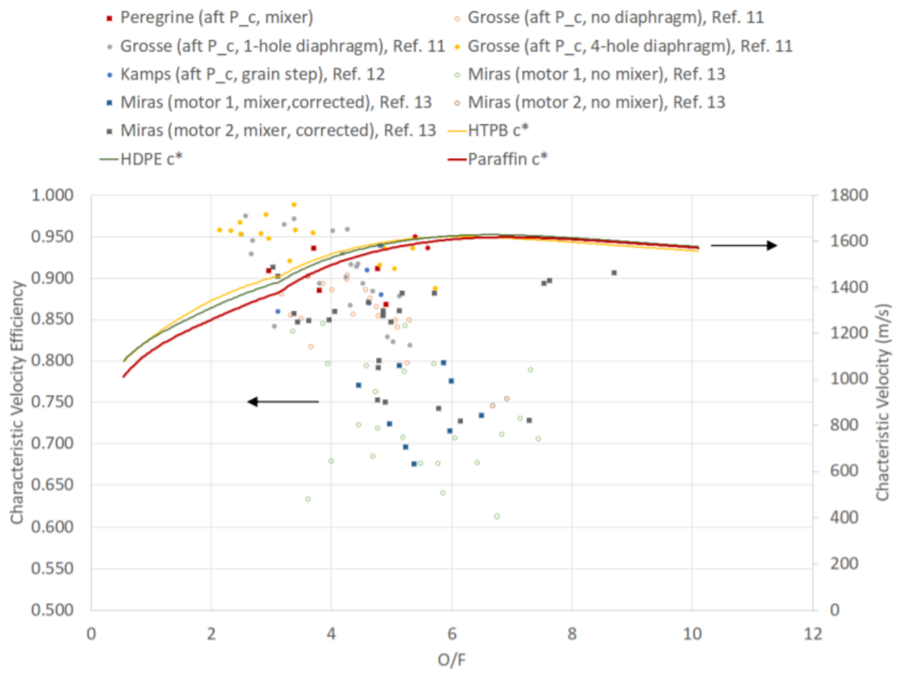

Figure 5.9: Various combustion efficiencies recorded in past literature for paraffin wax, HTPB, HDPE and a selection of enhanced fuel grains over a range of oxidiser mass fluxes (Zilliac et al., 2020) .

the other hand, started with comparable efficiencies to the baseline paraffin at 28% at 7.7 g/cm^2s and then reached 67% at 15.5 g/cm^2s. These values do differ significantly from literature - when hybrid rocket engines are built with a specific mission in mind, they can reach combustion efficiencies between 83-91% (Makle et al., 2003) . The discrepancy could be attributed to the relatively low oxidiser mass fluxes used in this study, where the O/F ratios may not be at their optimal point. Despite this, the data collected here shows how higher chamber pressures and thrust are achieved by not only the rate of regression but also the efficiency of combustion as seen with the ABS fuel grain outputting higher levels of thrust and pressure despite having lower regression rates than the paraffin fuel grain.

The findings in figure 5.9 demonstrate that fuel grains with a mechanism to induce higher levels of turbulence in the boundary layer combustion, boosted combustion efficiency by about 11% on average. According to diffusion flame combustion theory (Zilliac et al., 2020) , the large scale flow structures formed by these devices raise the level of mixing down to the molecular scale, resulting in the 11% efficiency boost. One disadvantage of some mixing device configurations is that they boost fuel regression rate locally, potentially increasing the risk of a case burn through during a full-duration burn. Irreversible losses are also linked with mixing devices, which must be appropriately accounted for in order to determine whether they create a net characteristic velocity advantage. Often the combustion efficiency will fall throughout the burn, much like in the case of the Mars Ascent Hybrid Vehicle (Karp et al., 2016) , i.e. as the O/F ratio decreases. In the case of this study, this could also be represented by the injection of lower mass fluxes - where the O/F ratio is further left of the curve. Zilliac et al (2020) suggest there could be two possible interactions at play here: 1) the falling chamber pressure from lower levels of propellant mixing is caused by geometric changes as the fuel port opens up, which could then be in part offset by, and 2) a minimal increase in diffusion rate as the pressure falls, where diffusion rates are said to vary with pressure and the rate of combustion varies with the square of that pressure (Ray and Glassman, 1983) . Thus, the combustion efficiency is expected to decrease as chamber pressure falls - as evident in the data gathered in this study (figure 5.8).

The results of hybrid engine simulations can also provide some further insight to correlate the results of this study. By observing several past attempts to simulate the boundary layer combustion within a hybrid rocket engine using computational fluid dynamics (CFD), they can provide a peek at some aspects of combustion that cannot be easily measured and present some indications into the factors that influence combustion efficiency. The findings of Messineo et al's (2016) axisymmetric unsteady Reynolds-Averaged Navier Stokes (URANS) with chemical reaction simulation of an H2O2/HDPE engine show vortices that form near the leading edge of the fuel grain and develop as they are convected downstream are of particular importance. As expected, the flame sheet is found in the boundary layer, separating the oxidizer-rich flow along the engine centerline from the fuel-rich zones. In this situation, the computed combustion efficiency is 0.926 (Messineo et al., 2016) . In a computational experiment, a jet was added at the aft end of the fuel grain, suppressing the vortical flow in the post-combustion chamber, resulting in a fall in efficiency to 0.894. The impact of large-scale structures in turbulent shear flow and the consequential mixing on combustion efficiency is clearly demonstrated by these results. The simulations in this section demonstrate the relationship between fuel and oxidizer mixing, chemical kinetics, and combustion efficiency. In a spatially and temporally changing process, large eddies produce smaller eddies. At the molecular level, stirring alone does not result in mixing. Diffusion, which is caused by the shearing of the mean flow field in the presence of viscosity, drives mixing (Durand et al., 2019) . Because Reynolds numbers are so high, it's evident that molecular diffusion is overshadowed by diffusion caused by turbulence in the fuel port's wall-bounded shear flow and the post-combustion chamber's free shear layer. As a result, the diffusion-flame combustion processes in hybrid systems are inextricably linked to fuel and oxidizer transport through bulk flow turning and turbulence (Zilliac et al., 2020) .

These findings may shed light on the process behind the gyroid fuel gain's improved combustion efficiency above baseline paraffin and ABS fuel grains, as evidenced in the study's findings. This could signify that the gyroid structures can increase shearing of the mean flow field through induced turbulence, resulting in more mixing in the diffusion flame. Although this experiment cannot prove it, it does imply that there is an effect on the level of mixing that occurs throughout the boundary layer combustion process. The hypothesis was that at the targeted oxidiser mass flow rate of 10.7 g/cm^2s, we would see enhanced performance. Instead, with higher mass fluxes, we detect an increasing trend in performance. Higher mass fluxes tests are recommended to truly understand the degree of this effect. Unfortunately, due to the facility's safety restrictions, these mass fluxes were not tested, but they are strongly encouraged for future research into this type of fuel grain design. In terms of combustion efficiency, the gyroid fuel grain surpasses the baseline paraffin and ABS fuel grains. The design philosophy of gyroid fuel grains is to increase the rate of mixing of the flow within the boundary layer combustion process by manipulating the flow without disrupting the delicate balance between heat transfer to the fuel grain and fuel production, which is critical to obtaining uniform and repeatable regression rates (Zilliac et al., 2020) . The influence of these dynamics may be extrapolated from the improved combustion efficiency shown in the results (figure 5.8) and the insights gained from analysing hybrid combustion models.

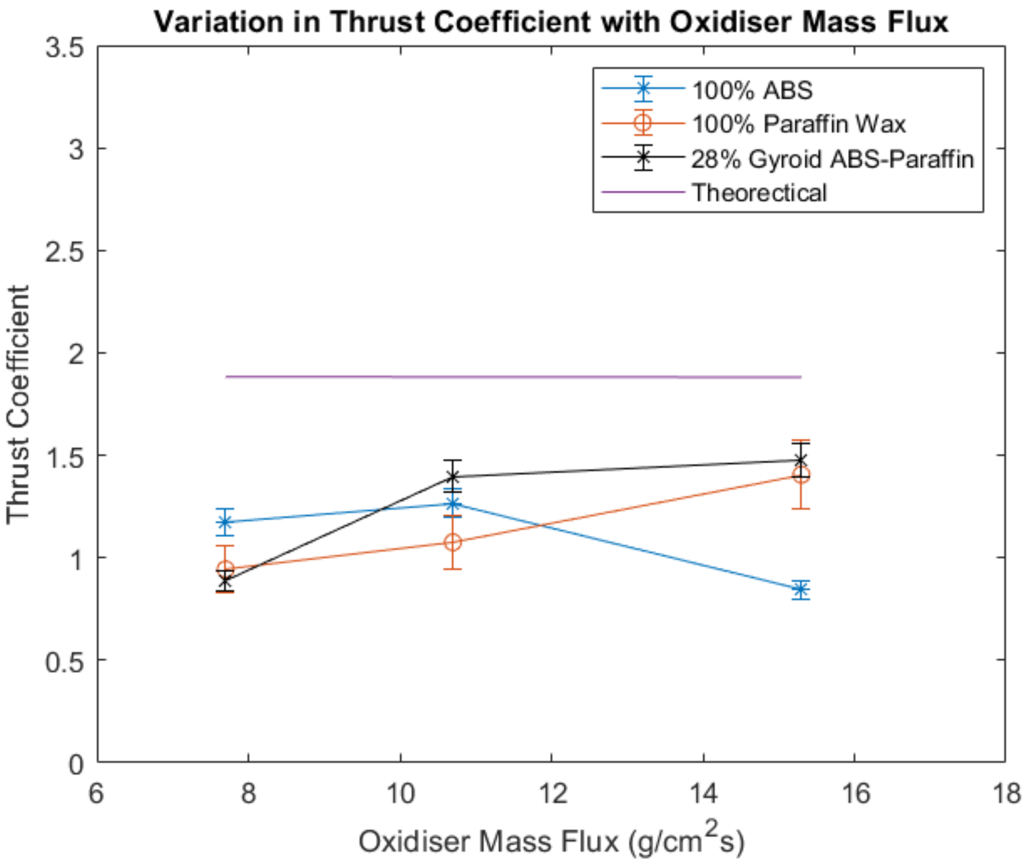

Figure 5.10: Calculated average thrust coefficient, for baseline ABS, paraffin wax and gyroid fuel grains across varying oxidiser mass fluxes tested.

5.4.2 Thrust Coefficient

The thrust coefficient can provide some insight into the potential performance of each fuel grain and the levels of thrust it could reach if it weren't for the restrictions imposed in this study. The raw thrust levels obtained in these experiments give a glimpse of how much thrust is produced given the design of the nozzle - however, the performance is quite different when we take into account the thrust coefficient. Figure 5.10 displays the thrust coefficients (see equation 4.11) for each fuel grain across the different oxidizer mass fluxes tested.

The data suggests the two paraffin-based fuel grains perform better at higher mass fluxes as opposed to the baseline ABS fuel grain. The higher thrust coefficient at 10.7 g/cm^2s suggests that the difference in thrust recorded between the baseline ABS and the gyroid fuel grains is closer than what was measured after applying the thrust coefficient and the gap grows even larger at 15.3 g/cm^2s of oxidizer mass flow. Of interest is the significant coefficients seen for the baseline paraffin and gyroid fuel grains at the higher mass flow rate - the thrust should theoretically be of the order of 50% greater than what was recorded in the static fire tests, if the nozzle was optimised.

5.4.3 Specific Impulse

The specific impulse is another important statistic for analysing the effectiveness of any rocket propulsion system since it is directly related to the variation in the amount of movement per unit weight

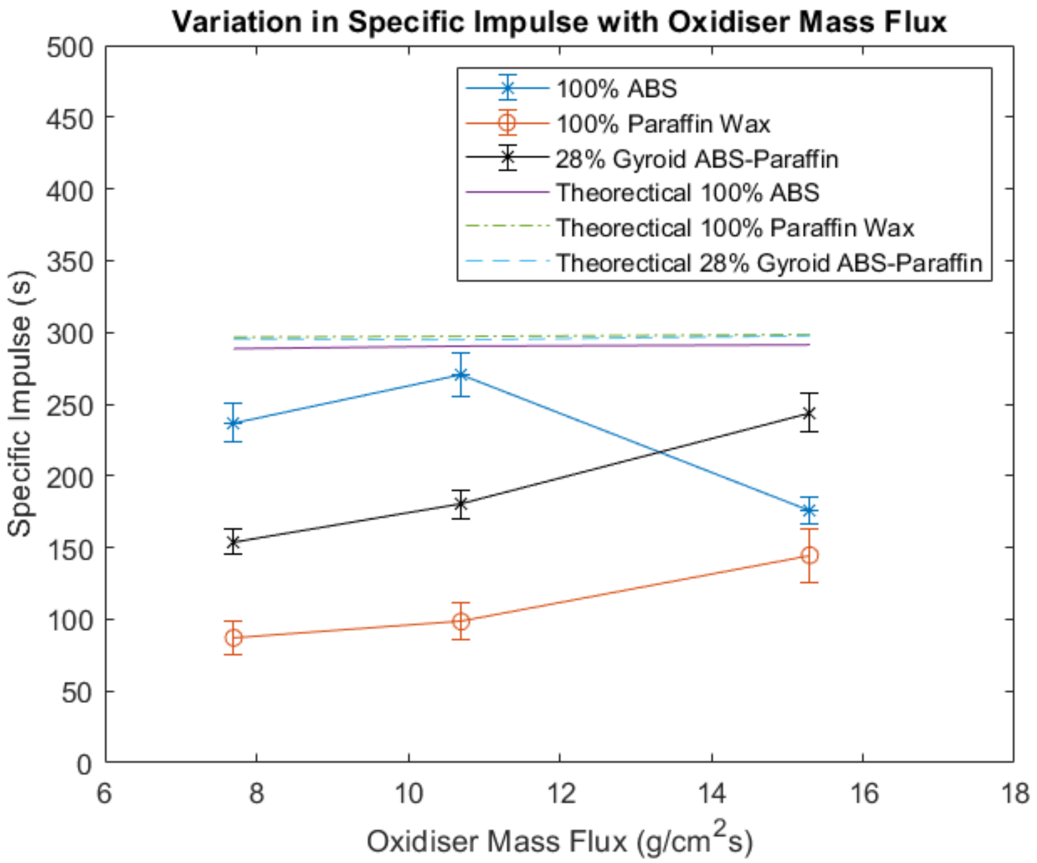

Figure 5.11: Calculated average specific impulse (Isp), for baseline ABS, paraffin wax and gyroid fuel grains across varying oxidiser mass fluxes tested. Referenced against theoretical values obtained through CEA.

of the propellant (Sutton and Biblarz, 2016) . The greater the I_{sp} value, the less propellant the engine requires to operate at a given total impulse, and thus the better the performance. The average specific impulse for the data set acquired in this investigation has been calculated (Equation 4.2), and figure 5.11 exhibits the results for each fuel formulation over the oxidiser mass fluxes examined, as well as the CEA theoretical values for reference.

A comparison of the I_{sp} of the two baseline fuel grains reveals similar behaviours to their relative performance in combustion chamber pressure - the ABS fuel grain outperforms the paraffin fuel grain at lower mass fluxes, but at greater mass fluxes, the results become more equivalent. These findings support the assumption that higher mass fluxes are required for paraffin fuel grains to work efficiently. When this data is compared to the literature, the results are equivalent to the literature for paraffin wax (Lee and Tsai, 2008; Bouziane et al., 2018) . In other operating circumstances, the main reasons for poor performance could be incomplete combustion, pressure losses throughout system components and within the chamber, heat loss, and inherent combustion instabilities (Karabeyoglu et al., 2002; Lee et al., 2020) . The fuel grain shell geometry for each fuel grain used in this study was designed with the intent to minimise the pressure losses due to re-circulation at the aft end of the fuel grain. Figure 5.12 showcases the the flow path for a typical fuel grain in contrast with the geometry used for this project. The closer the experimental values are to their theoretical equivalent, the more it suggests complete combustion because pressure and heat losses are more in tune with the design of the chamber and

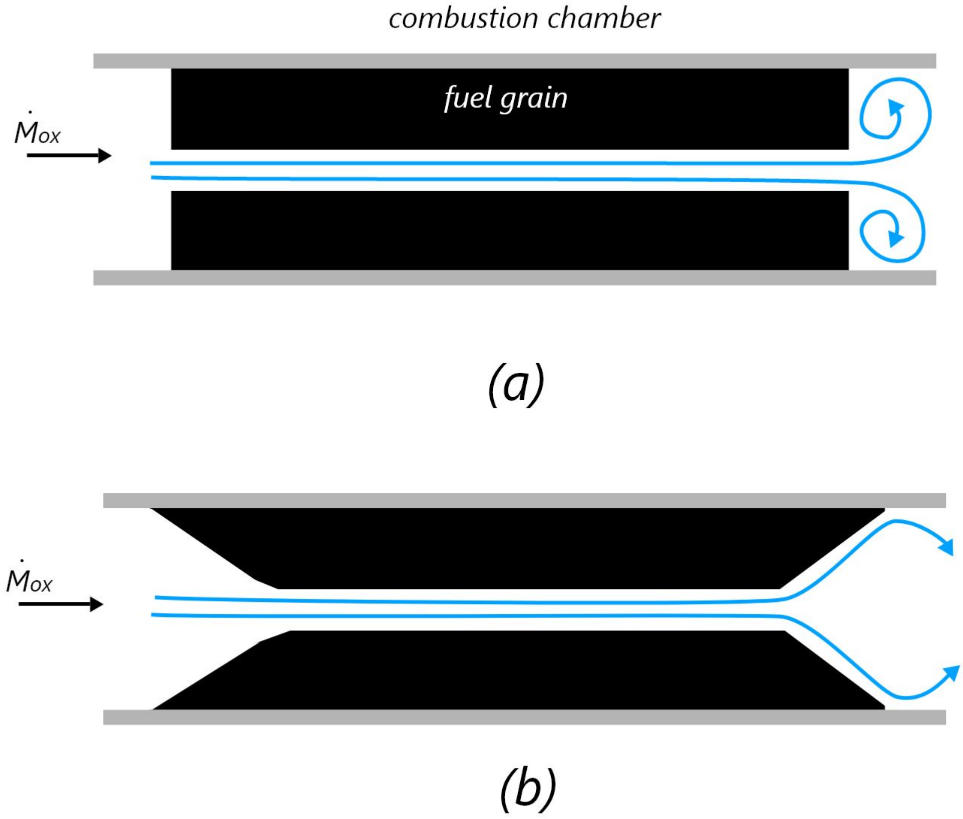

Figure 5.12: Simplified schematic of the flow path of the oxidiser at the aft end for (a) typical fuel grain and (b) the fuel grain shell geometry used in this study.

oxidiser feed as opposed to the performance of the fuel grain - which could imply that incomplete combustion and combustion instability are the main factors contributing to lower than expected values.

Following this notion, if we observe how the gyroid fuel grain behaves with increasing oxidiser mass flow rate, it behaves more like the paraffin fuel grain than the ABS baseline - suggesting that despite having a mixture of the two fuels in its formulation, the performance increases here suggests a biased contribution due to the liquefying nature of paraffin as opposed to the efficiency of ABS fuels. We see that the gyroid fuel grain continues to outperform the paraffin fuel grain across parameters and signals more efficient performance than the ABS at higher mass flows. When comparing the gyroid fuel grain with other attempts at enhancing the performance of paraffin-based fuel grains such as in Wang et al's helical ABS structure embedded in paraffin (Wang et al., 2020) , the results were comparable at the higher mass flow rate tested in this study, where the highest average specific impulse reached for the gyroid was 243 seconds and Wang et al's (2020) novel fuel grain reached 242 seconds. So very similar in performance between the two grains which is interesting given the differences in the ABS structures at play. It is important to note, however, that in Wang et al's experiments, they operated at higher oxidiser mass fluxes and oxidiser gas pressures. It would be of interest to see how the gyroid fuel grain compares when the same oxidiser mass flow rate is used. It was suggested that the combustion efficiency was principally raised because gas travelling through the nested helical structure generated vortices between neighbouring blade protrusions, similar to how the regression rate was improved. These, in turn, increased heat and matter exchanges between the main flow zone and the inner surface of the fuel grain. As a result, the mixing of the oxidizer and fuel was more efficient, and the burning period was increased, increasing the likelihood of chemical reactions in the combustion chamber (Wang et al., 2020) .

The differences of these studies seem to be a difference of macro and micro-targeted enhancements - where Wang et al's (2020) fuel grain focused on the large scale vortices generated by helical structure, the gyroid fuel grain targeted the smaller scale wavelengths produced by the oxidizer mass flow over the liquid layer and exciting those frequencies to break up the liquid layer further. Both were conducted with closed chamber hot-fire tests, so the exact mechanics at play cannot be confidently determined with these results alone. Despite this, this presents a promising method to increase the efficiency and performance of paraffin fuel grains strictly by altering the geometry of the fuel grain.

5.5 Post-Hot Fire Fuel Grain Analysis

After static test fires, the gyroid fuel grains were subject to a cross sectional cut to reveal the nature of the port structure post-combustion. Figure 5.13 displays a cut in the center line along the axis of the fuel port of a gyroid fuel grain at each tested mass flux. Initially, we can observe the regression rate difference at the higher oxidiser mass flux with a visually larger port diameter, and that is to be expected, while at 7.7 and 10.7 g/cm^2s oxidiser mass fluxes, the grains had similar resulting port sizes at the end of the burn. We can also see the aft end of the fuel grain regressing significantly more than the fore end. This could be the result of the greater levels of mixing further down the fuel port but it also suggests that very little to no combustion actually occurs at that fore end converging section of the fuel grain and could be a demonstration of the developing boundary layer at the leading edge of the grain. At that point, the boundary layer is still quite thin relative to the diameter of the port and that majority of the vaporised fuel doesn't mix until further down the boundary layer as it fully develops. Residue of combustion is seen in the fore end of the grains after each static test fire, but relative to the aft end, it could purely be due to the ignition of the steel wool.

If we take a closer look at the surface of the fuel grain port, we observe some larger scaled surface roughness features of the fuel grain in the outline shown in figure 5.13 - a result of the melting and deformation of the ABS gyroid structure when subject to a purge after the burn, but we can see that the paraffin wax is also greatly influenced by the ABS structure. Figure 5.14 shows a closer capture of the gyroid fuel grain, to better showcase the ABS structure with the paraffin wax after a burn, as the black ABS used in the experimental fuel grains doesn't provide a sufficiently clear view. In this figure, we are observing a gyroid fuel grain printed with red ABS filament and if we analyse the structure of the paraffin wax we can see a clear sinusoidal wave pattern, very similar to what was seen in Petrarolo et al's (2018) observation with the KHI represented in the flame front. What we see here suggests the hypotheses raised by Petrarolo et al - where the flame front is a good indication of the dynamics of the liquid layer at the surface of the fuel grain, is in fact correct to some degree. Although, it cannot be confirmed if the structure is identical and instead it simply shows a similar trend, but with different wavelengths in the liquid layer as opposed to the flame front. In figure 5.14, the wavelength pattern

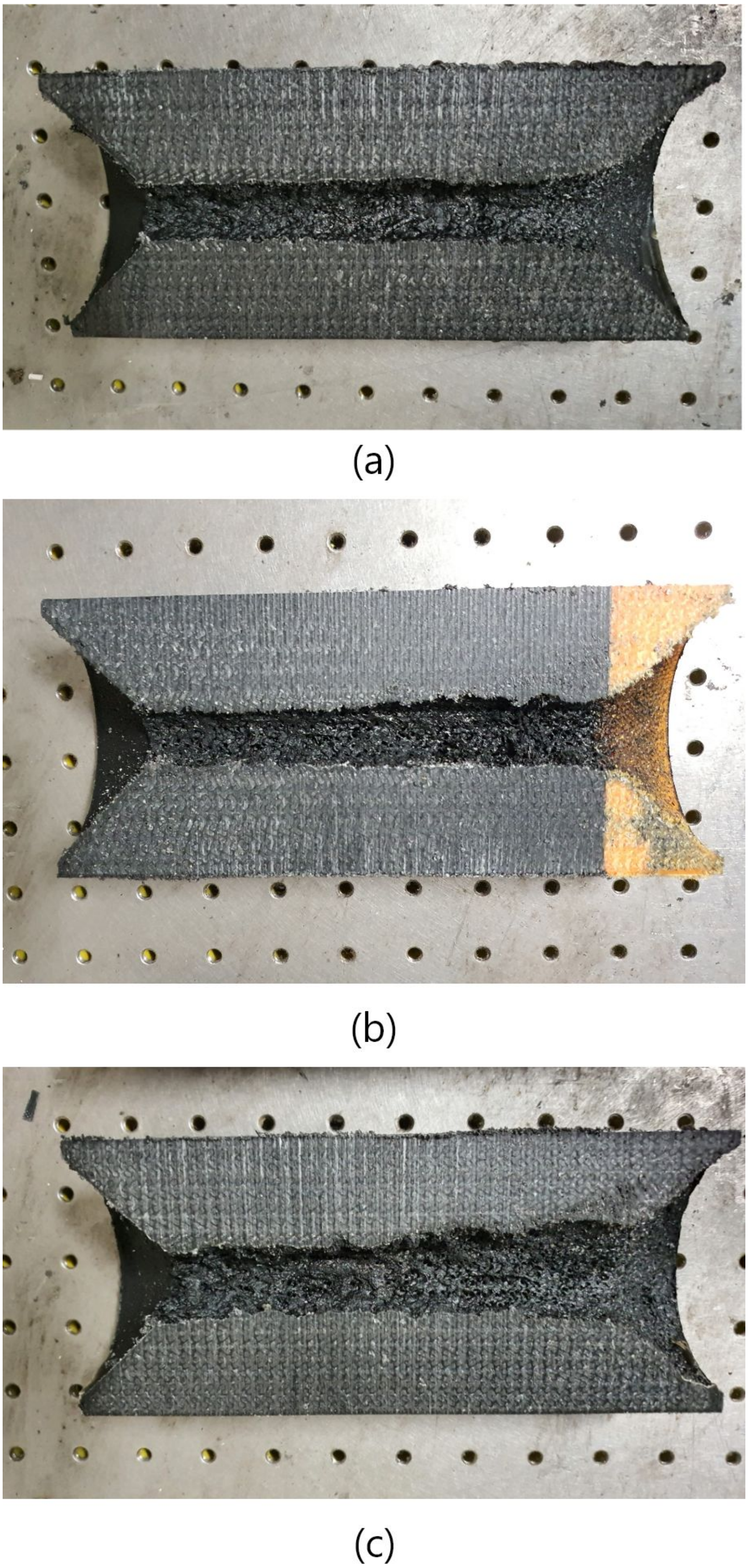

(a)

(b)

(c)

Figure 5.13: Cross section cuts of gyroid fuel grains post fire at (a) 7.7 g/cm^2s , (b) 10.7 g/cm^2s and (c) 15.3 g/cm^2s oxidiser mass flux. The images are orientated such that the oxidiser flow is from left to right.

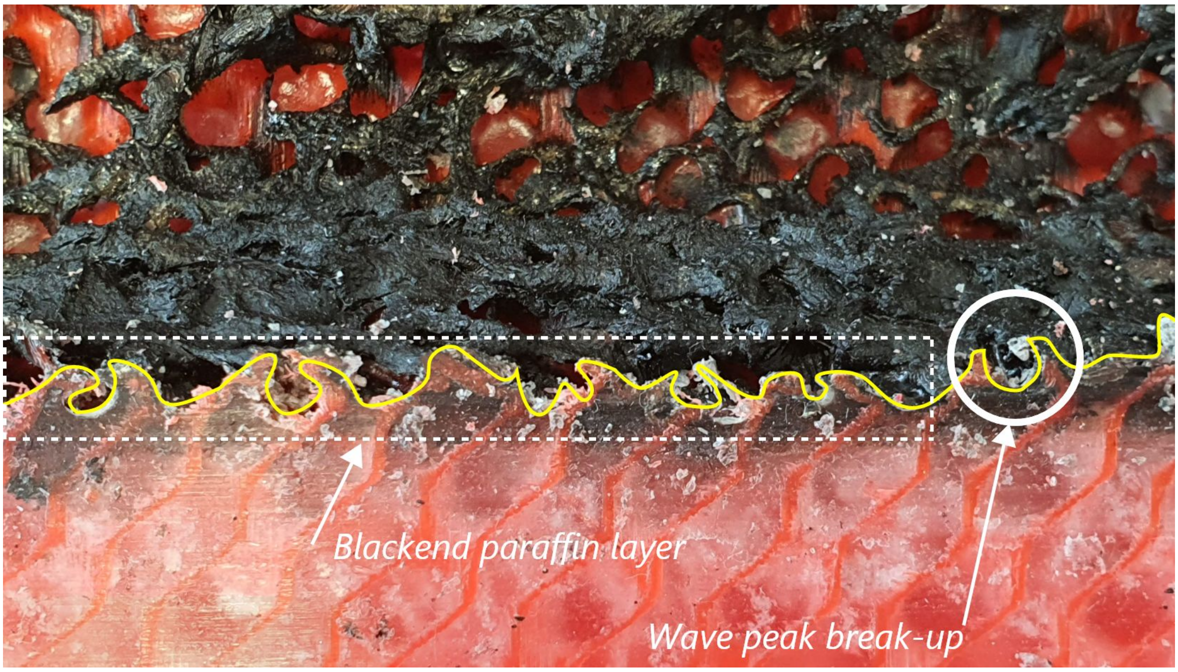

Figure 5.14: Close up capture of a 28% gyroid fuel grain after a 10 second, 10.7 g/cm^2s oxidiser mass flux hot fire. Outlined in yellow is a simplified sketch of the paraffin profile. The blackened paraffin layer and the break-up at the wave peak are also highlighted in the figure.

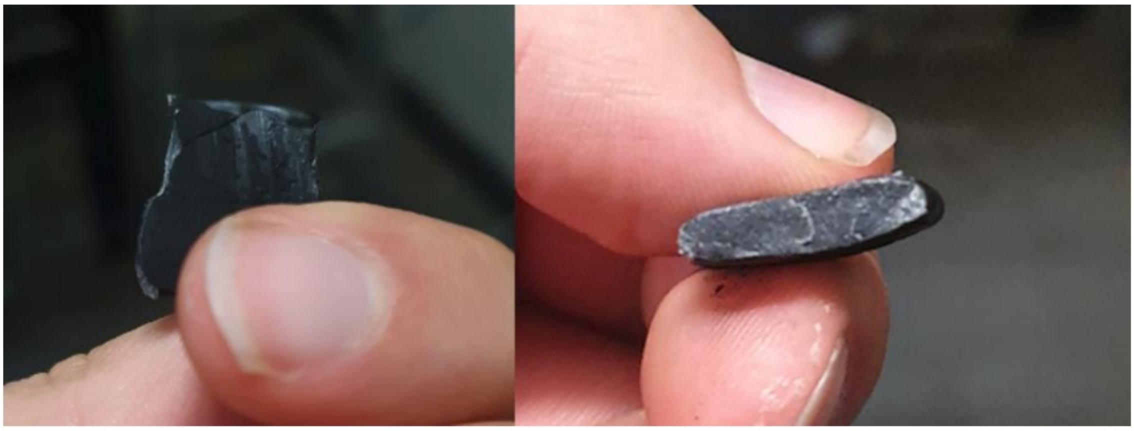

Figure 5.15: Hardened paraffin wax sample post gyroid fuel grain hot fire.

of the paraffin wax along the fuel port suggests a consistent wavelength that follows the wavelength of the gyroid structure, but with a small break up wave at the peak of each wave, seen in the circled section of the figure. This is a rather interesting observation that reinforces the hypotheses raised in this study, whereby targeting specific mass fluxes with the corresponding wavelength, we can see an amplification, or disruption, to the wave structures and further promoting greater rate of droplet entrainment and droplet break-up.

After each test fire, some residual molten paraffin wax is sampled and inspected, seen in figure 5.15. The blackened sample piece, when broken, shows that there must be a considerable amount of carbon infusion in the molten paraffin wax. When cross referenced with the images of the grains presented earlier (figure 5.14), we see at the top layer of the paraffin wax, there exists a thin blackened layer. From these observations, it suggests that the carbon produced from the burning of the ABS structure is infusing with the paraffin liquid layer. This unexpected bi-product could provide some potentially significant implications for using ABS fuel structures with paraffin wax, The samples resemble a product similar to those that have been intentionally prepared with some form of black pigmentation. If using an ABS-paraffin fuel grain allows for passive pigmentation, then this could supersede the requirement of elaborate rotary equipment. However, more testing is required to confidently conclude these findings.

5.6 Summary

To summarise the findings from the results gathered in this study - we first observed consistent hot fires across the same fuel grain under the same oxidiser mass flow conditions to provide repeatability measures prior to the experimental phase of the campaign. Pure ABS and paraffin were the baseline fuel grains to compare and contrast against the results from existing literature, as well as a benchmark for the gyroid fuel grain developed for this study. The baseline fuel grains behaved as expected, where as at low mass fluxes ABS outperformed paraffin wax in terms of thrust and chamber pressure. However, at the higher mass flux of 15.3 g/cm^2s, baseline paraffin began to output comparable results to that of the ABS (figure 5.4). Both grains saw improvements in combustion efficiency with higher mass fluxes, however, the ABS was consistently more efficient than the baseline paraffin (figure 5.8). The discrepancy showcases the paraffin wax fuel grains dependency on relatively higher mass fluxes to achieve higher combustion efficiencies (Karabeyoglu et al., 2005) , where a portion of the droplets entrained have not fully combusted. Contrastingly, ABS begins to drop in terms of efficiency at the higher mass flux and suggesting a greater blocking effect and hindering the regression of the fuel, thus the consequential slight drop in regression rate as well (figure 5.7).

The results gathered from the gyroid fuel grain was particularly interesting, with aspects of the data reinforcing the hypothesis of targetted wavelengths produced at the corresponding mass flux, while other factors suggesting performance improvement purely due to higher mass fluxes. All in all, we observe higher performance metrics for the gyroid fuel grain over the baseline paraffin fuel grain across the board and similar is seen when compared to ABS in terms of efficiencies (figures 5.8 and 5.11). However ABS produced higher chamber pressures and thrust output at lower mass fluxes, evident with its comparison against baseline paraffin. When compared to other performance enhancing fuel grain designs from literature (Wang et al., 2020) , the gyroid fuel grain performs consistently and further reinforces the positive effect of turbulence inducing mechanisms on improving regression rates. The higher combustion efficiencies and thrust coefficients further promote the notion that the gyroid structure is capable of ensuring the entrained droplets are being combusted relative to the baseline paraffin fuel grains. Upon inspection of the gyroid fuel grains after hot fire - clear wave-like structures can be seen at the surface (figure 5.14). The structures seem to resemble something similar to the flame fronts observed in Petrarolo et al. (2018) study on the KHI seen in the liquid layer. Wave break-up patterns were seen at the peak of the gyroid sinusoidal structure - suggesting the gyroid structures are able to break up the liquid layer wave dynamics to promote more droplet entrainment. A thin blackened layer is observed at the top surface of the fuel grain after a hot fire, and could be a result of the carbon produced from ABS combustion infusing with the paraffin liquid layer. The implication of this self-pigmenting method could supersede existing methods required to produce even, blackened paraffin wax fuel grains.

Chapter 6

Conclusions

This thesis presents an experimental investigation of the impact of ABS gyroid infill structures on the performance liquefying solid fuel grains in Hybrid Rocket Engine systems. The study explores the effect of inducing liquid layer instabilities by excite particular wavelengths from Kelvin-Helmholtz Instabilities to improve regression rates. This investigation required the construction of a lab-scaled hybrid rocket engine test facility, capable of hot firing different fuel grains and collecting performance data to compare and contrast the effectiveness of this novel fuel grain design.

The new facility is intended to not only service the gyroid fuel grain investigation undertaken here, but to also be utilized in a wide range of other future experiments. Hence, the design requirements for the new facility are based on modularity and equipped with critical instrumentation with a wide operating range. The design process, along with some of the key practical considerations involved in the construction of the facility is discussed in Chapter 3. The system level considerations for a closed combustion chamber hybrid rocket engine are presented, before a component level design of the specific facility is explored. A specific focus in this investigation was the design and manufacture of fuel grain structures that allow for consecutive hot fires with minimal down time. A key aspect to achieve this is the use of 3D printed shells, used for both baseline ABS and paraffin fuel grains, as well as the gyroid fuel grain. 3D printing allowed for rapid prototyping and for more optimised structures to minimise the adverse effects of recirculation, typically seen in more traditional fuel grain designs. The manufacturing process is outlined in Chapter 4, and detailed work instructions can be seen in Appendix B. Given the laboratory scale of the facility, for safety and usability, an automated control system was developed and implemented (Chapter 3). The control system proved capable of maintaining the flow of oxidiser for discrete intervals, with a nitrogen purge enabled after hot fire and for emergency stop procedures. The system was developed with VI sequencing to allow for different hot fire configurations. For the experimental campaign, the process sequence started with the ignition of an e-match with steel wool, then the actuation of the oxidiser solenoid valve, followed by the purging of the chamber with nitrogen. With the facility constructed and operational, the thesis shifts to a study of the performance of baseline and gyroid fuel grains.

To study the effect of surface topology on the performance of liquefying fuel grains, the chamber pressure, thrust and regression rate are measured for each fuel grain hot fire. These metrics are then used in key calculations to better compare the performance between each fuel grain, by analysing the trends in combustion efficiency (η_b), specific impulse (I_{sp}) and the thrust coefficient (C_F). The results for the baseline cases were comparable to what was seen in the literature, with paraffin wax fuel grains exhibiting, on average, double the regression rate when compared to the baseline ABS fuel grains. However, it was seen that ABS fuel grains were more efficient than paraffin (ABS combustion efficiencies reached 60%, where paraffin fuel grains only reached 38%) - i.e. is capable of producing higher chamber pressures and thrust at lower regression rates (also can be portrayed as the mass flow rate of fuel) and this also seen in the values for I_{sp} (with ABS reaching 275s and paraffin wax reaching 130s). Despite this, we see a trend where paraffin based fuel grains performed significantly better at higher mass fluxes, and was seen to either be comparable or even outperform baseline ABS - reinforcing the notion of paraffin wax requiring higher mass fluxes to be effective (Whitmore et al. 2016).

The performance of the gyroid fuel grain outperformed the baseline paraffin wax consistently and exhibited the highest efficiencies out of the three fuel formulations tested in this investigation, reaching 80% combustion efficiency and 240s of specific impulse. The thrust coefficients calculated also suggests that the effectiveness of the gyroid fuel grain could theoretically be almost 1.5 times greater than the values obtained in this investigation. Upon closer inspection of the gyroid fuel grains after hot fire, we observe structures of the paraffin wax at the surface resembling close to the wave-like structures in KHIs. The wavelengths follow closely with the gyroid structure, with small break-up waves at each peak. This was a rather interesting observation and the implications from this could suggest that the improved performance seen in the data could be attributed to the improved entrainment and break-up of droplets from the liquid layer due to this gyroid structure. However, these potential implications to prove the hypothesis of this study requires further investigation to confidently conclude the exact nature of these performance increases seen with the gyroid fuel grain. Despite this, the results of this investigation suggest that there are performance improvements to be had with these gyroid fuel grains. Apart from this, uniform carbon deposits from the burning of ABS were seen in hardened paraffin samples after hot fires, with the implication of passive carbon impregnation, potentially superseding the need for elaborate rotary equipment. Although there requires further investigation to adequately prove the effectiveness of gyroid fuel grains, the notion that fuel grains should be utilising 3D printing technologies still stands and is greatly reinforced from this investigation.

The idea of this investigation was to provide an entry into a deeper investigation with 3D printing fuel grains that take advantage of the wave-like nature of the liquid layer and targeting wavelengths produced at specific oxidiser mass fluxes. It is suggested that future research into this be focused on observing the dynamic behaviour of the liquid layer when coupled with the gyroid structure to adequately conclude the effectiveness of this novel fuel grain design and to allow for more quantitative analysis to aid in modelling. Ultimately, this could promote the emergence of utilising 3D printed fuel grains to achieve mission specific thrust profiles, with rapid manufacturing turnarounds.

Bibliography

Barrere, M., Jaumotte, A., De Veubeke, B., & Vandenkerckhove, J. (1960). *Rocket Propulsion*. Elsevi Publishing Company.

Bisin, R., Paravan, C., Alberti, S., & Galfetti, L. (2019). An Innovative Strategy for Paraffin-based Fuels Reinforcement: Part I, Mechanical and Pre-Burning Characterization, 14 pages.

Blom, H., Yeh, R., Wojnarowski, R., & Ling, M. (2006). Detection of degradation of ABS materials via DSC. *Thermochimica Acta - THERMOCHIM ACTA*, *442*, 64–66.

Boronowsky, K. (2011). Non-homogeneous Hybrid Rocket Fuel for Enhanced Regression Rates Utilizing Partial Entrainment.

Bouziane, M., De Morais Bertoldi, A. E., Milova, P., Hendrick, P., & Lefebvre, M. (2018). Development and Testing of a Lab-scale Test-bench for Hybrid Rocket Engines. *2018 SpaceOps Conference*.

Brodkey, R. S. (1967). The Phenomena of Fluid Motions. *Addison-Wesley, Reading, Mass*, 112–115, 489, 560–565.

Brown, G. L., & Roshko, A. (1974). On density effects and large structure in turbulent mixing layers. *J. Fluid Mech.*, *64*(4), 775–816.

Brown, T., & Lydon, M. C. (2005). Testing of Paraffin-Based Hybrid Rocket Fuel Using Hydrogen Peroxide Oxidizer. *Colorado Space Grant Consortium*.

Cantwell, B., Altman, D., & Dimotakis, P. (1978). Structure and entrainment in the plane of symmetry of a turbulent spot. *J. Fluid Mech.*, *87*(04), 641.

Chala, G., Sulaiman, S., Japper-Jaafar, A., & Kamil, W. (2015). Effects of Cooling Regime on the Formation of Voids in Statically Cooled Waxy Crude Oil. *International Journal of Multiphase Flow*, *77*.

Chandler, A., Jens, E., Cantwell, B., & Hubbard, G. S. (2012). Visualization of the Liquid Layer Combustion of Paraffin Fuel for Hybrid Rocket Applications. *48th AIAA/ASME/SAE/ASEE Joint Propulsion Conference &amp; Exhibit*.

Connell, T., Young, G., Beckett, K., & Gonzalez, D. R. (2019). Enhanced Solid Fuel Regression in a Hybrid Rocket Employing Additively Manufactured Fuels Exhibiting Novel Grain Port Geometries. *AIAA Scitech 2019 Forum*.

Craik, A. D. D. (1966). Wind-generated waves in thin liquid films. *Journal of Fluid Mechanics*, *26*(2), 369–392.

Crawford, M. E., & Kays, W. M. (1993). *Convective Heat and Mass Transfer*. McGraw–Hill.

Dao, P. D., Parley, R., Soletsky, P., & Gelbwachs, J. (1997). Lidar measurements of the stratospheric exhaust plume of launch vehicles. *Conference on Lasers and Electro-Optics*.

De Luca, L. T., Shimada, T., Sinditskii, V. P., & Calabro, M. (2017). *Chemical Rocket Propulsion: A Comprehensive Survey of Energetic Materials* (Vol. 1). Springer.

Durand, J. E., Lestrade, J.-Y., & Anthoine, J. (2019). Fuel Regression Modelling for Hybrid Rocket CFD Simulations, 18 pages.

Dyer, J., Doran, E., Dunn, Z., Lohner, K., Bayart, C., Sadhwani, A., Zilliac, G., Cantwel, B., & Karabeyoglu, A. (2007). Design and Development of a 100km Nitrous Oxide/Paraffin Hybrid Rocket Vehicle. *43rd AIAA/ASME/SAE/ASEE Joint Propulsion Conference &amp; Exhibit*.

Eilers, S. D., & Whitmore, S. (2008). Correlation of Hybrid Rocket Propellant Regression Measurements with Enthalpy-Balance Model Predictions. *Journal of Spacecraft and Rockets*, *45*(5), 1010–1020.

Francois, J. M. (1988). Empirical Formulas to Evaluate the Friction Coefficient in Non-Newtonian Lubrication. *Journal of Tribology*, *110*(2), 380–382.

Funada, T., & Joseph, D. (2001). Viscous potential flow analysis of Kelvin–Helmholtz instability in a channel. *Journal of Fluid Mechanics*, *445*, 263–283.

Gater, R., & L'Ecuyer, M. (1970). A fundamental investigation of the phenomena that characterize liquid-film cooling. *International Journal of Heat and Mass Transfer*, *13*(12), 1925–1939.

Hewitt, G. F., & Hall-Taylor, N. S. (1970). Annular Two-Phase Flow. *Pergamon Press, N. Y.*, 136–149.

Heydari, M. M., & Ghadiri Massoom, N. (2017). Experimental Study of the Swirling Oxidizer Flow in HTPB/N $_2$ O Hybrid Rocket Motor. *International Journal of Aerospace Engineering*, *2017*, 1–10.

Hill, P., & Peterson, C. (1992). *Mechanics and Thermodynamics of Propulsion* (2nd ed.). Pearson.

Hinze, J. O. (1955). Fundamentals of the Hydrodynamic Mechanism of Splitting in Dispersion Process. *AlChE J.*, *1*, 289.

Hurst, A. M., & VanDeWeert, J. (2013). An Experimental and Theoretical Investigation of Wave Propagation in Teflon and Nylon Tubing With Methods to Prevent Aliasing in Pressure Scanners. *Proceedings of ASME Turbo Expo 2013: Turbine Technical Conference and Exposition*, 8.

Ishii, M., & Grolmes, M. A. (1975). Inception criteria for droplet entrainment in two-phase concurrent film flow. *AIChE J.*, *21*(2), 308–318.

Jens, E. T., Miller, V. A., Mechentel, F. S., Cantwell, B. J., & Hubbard, G. S. (2014). Visualisation of Combustion in a Turbulent Boundary Layer Over a Melting Fuel. *Australasian Fluid Mechanics Conference*, *19*, 4.

Kanazaki, M., Ariyairt, A., Chiba, K., Kitagawa, K., & Shimada, T. (2015). Conceptual Design of Single-stage Rocket Using Hybrid Rocket byMeans of Genetic Algorithm. *Procedia Engineering*, *99*, 198–207.

Karabeyoglu, A., Cantwell, B. [B.J.], & Altman, D. (2001). Development and testing of paraffin-based hybrid rocket fuels. *37th Joint Propulsion Conference and Exhibit*.

Karabeyoglu, A., Cantwell, B. [Brian], & Stevens, J. (2005). Evaluation of the Homologous Series of Normal Alkanes as Hybrid Rocket Fuels.

Karabeyoglu, A., Zilliac, G., Cantwell, B., De Zilwa, S., & Castellucci, P. (2003). Scale-up Tests of High Regression Rate Liquefying Hybrid Rocket Fuels. *41st Aerospace Sciences Meeting and Exhibit*.

Karabeyoglu, M. A., Altman, D., & Cantwell, B. J. (2002). Combustion of Liquefying Hybrid Propellants: Part 1, General Theory. *Journal of Propulsion and Power*, *18*(3), 610–620.

Karabeyoglu, M. A., & Cantwell, B. [B.J.]. (2002). Combustion of Liquefying Hybrid Propellants: Part 2, Stability of Liquid Films. *Journal of Propulsion and Power*, *18*(3), 621–630.

Karp, A. C., Nakazono, B., Benito Manrique, J., Shotwell, R., Vaughan, D., & Story, G. T. (2016). A Hybrid Mars Ascent Vehicle Concept for Low Temperature Storage and Operation. *52nd AIAA/SAE/ASEE Joint Propulsion Conference*.

Kobald, M., Verri, I., & Schlechtriem, S. (2015). Theoretical and Experimental Analysis of Liquid Layer Instabilities in Hybrid Rocket Engines. *CEAS Space Journal*, *7*, 11–22.

Lee, J., De Morais Bertoldi, A. E., Andrianov, A., Borges, R. A., Veras, C. A. G., Battistini, S., Morita, T., & Hendrick, P. (2020). Role of Precombustion Chamber Design in Feed-System Coupled Instabilities of Hybrid Rockets. *Journal of Propulsion and Power*, *36*(6), 796–805.

Lee, T.-S., & Potapkin, A. (2002). The Performance of a Hybrid Rocket with Swirling GOx Injection. *ASTRC/NCKU*, 7.

Lee, T.-S., & Tsai, H.-L. (2008). Combustion Characteristics of a Paraffin-Based Fuel Hybrid Rocket. *9th Asia-Pacific International Symposium on Combustion and Energy Utilization*, 9.

Lee, T.-S., & Tsai, H.-L. (2009). Fuel Regression Rate in a Paraffin-HTPB Nitrous Oxide Hybrid Rocket. *7th Asia-Pacific Conference on Combustion*, 5.

Makle, A., Zaye, A.-N., Abdalla, H., & EI-Senbawi, M. (2003). Effect of Post-Combustion on Combustion Efficiency in Hybrid Rocket Motors. *International Conference on Aerospace Sciences and Aviation Technology*, *10*(ASAT CONFERENCE), 1–14.

Marxman, G., & Gilbert, M. (1963). Turbulent boundary layer combustion in the hybrid rocket. *Symposium (International) on Combustion*, *9*(1), 371–383.

Marxman, G., Wooldridge, C., & Muzzy, R. (1964). Fundamentals of Hybrid Boundary-Layer Combustion. *Progress in Astronautics and Rocketry*, *15*, 485–522.

Marxman, G. A. (1965). Combustion in the turbulent boundary layer on a vaporizing surface. *Symposium (International) on Combustion*, *10*(1), 1337–1349.

McBride, J. (1994). Sanford Gordon and Associates Cleveland, Ohio, 64.

McCulley, J. M. (2012). Design and Testing of Digitally Manufactured Paraffin Acrylonitrile-Butadiene-Styrene Hybrid Rocket Motors, 82.

McDougall, C. C., Hill, C. D., Heinrichs, C. J., & Johansen, C. T. (2019). Spectroscopic Techniques for Measuring Regression Rates of Liquefying Hybrid Rocket Fuels, 9.

Mechentel, F. S., & Cantwell, B. J. (2018). Small-scale Gaseous Oxygen Hybrid Rocket Testing Facility Upgrades for Regression Rate and Combustion Efficiency Studies. *2018 Joint Propulsion Conference*.

Messineo, J., Lestrade, J.-Y., Hijlkema, J., & Anthoine, J. (2016). 3D miles simulation of a hybrid rocket with SWIRL injection, 12.

Nayfeh, A. H., & Saric, W. S. (1971). Non-linear Kelvin–Helmholtz instability. *Journal of Fluid Mechanics*, *46*(2), 209–231.

Newitt, D. M., Dombrowsk, N., & Knelman, F. H. (1954). Liquid Entraninment: I, The Mechanism of Drop Formation from Gas or Vapor Bubbles. *Trans. Inst. Chem. Eng*, *32*(244).

PCB-Group. (2014). *Load Cell Handbook: A Technical Overview and Selection Guide*. PCB Load; Torque Group.

Pelletier, N. (2009). Etude des Phenomenes de Combustion dans un Propulseur Hybride. Modelisation et Analyse Experimentale de la Regression des Combustibles Liquefiables. *Institut Superieur de L'Aeronatique et de L'Espace*, *Ph.D. thesis*,

Petrarolo, A., Kobald, M., & Schlechtriem, S. (2018). Understanding Kelvin–Helmholtz instability in paraffin-based hybrid rocket fuels. *Exp Fluids*, *59*(4), 62.

Petrarolo, A., Kobald, M., & Schlechtriem, S. (2019). Optical analysis of the liquid layer combustion of paraffin-based hybrid rocket fuels. *Acta Astronautica*, *158*, 313–322.

Piscitelli, F., Saccone, G., Gianvito, A., Cosentino, G., & Mazzola, L. (2018). Characterization and manufacturing of a paraffin wax as fuel for hybrid rockets. *Propulsion and Power Research*, *7*(3), 218–230.

Porrmann, D., May, S., Božić, O., & Lancelle, D. (2013). Regression rate models versus experimental results for hybrid rocket engines based on H2O2 and HTPB/AL. *Proceedings of the International Astronautical Congress, IAC*, *9*.

Ray, S., & Glassman, I. (1983). The Detailed Processes Involved in Flame Spread over Solid Fuels. *Combustion Science and Technology*, *32*(1), 33–48.

Schlichting, H. (1955). *Boundary Layer Theory*. McGraw–Hill.

Schoen, A. (1970). Infinite Periodic Minimal Surface Without Self-Intersections. *NASA Technical Note TN D-5541*.

Sevik, M., & Park, S. (1973). The Splitting of Drops and Bubbles by Turbulent Fluid Flow. *J. Fluid Eng*, *53*.

Sigma, A. (2021). Archive of Paraffin Wax Optical Characterisation. *Online Chemical Archives*.

Simmons, F. S. (2000). *Rocket Exhaust Plume Phenomenology*. Aerospace Press.

Sisi, S., & Gany, A. (2015). Combustion of Plain and Reinforced Paraffin with Nitrous Oxide. *International Journal of Energetic Materials and Chemical Propulsion*, *14*.

Sleicher, C. A., Jr. (1972). Maximum Stable Droplet Size in Turbulent Flow. *AlChE J.*, *8*(471).

Sorge, A. R., & Carmicino, C. (2002). Non-Intrusive Regression Rate Measurements in a Hybrid Rocket, 14.

Sutton, G., & Biblarz, O. (2016). *Rocket propulsion elements*. John Wiley & Sons.

Tanner, L. H. (1980). The surface tension effect on the flow of liquid down vertical or inclined surfaces. *J. Phys. D: Appl. Phys.*, *13*(9), 1633–1641.

Thomas, J., Stahl, J., Tykol, A., Rodriguez, F., & Petersen, E. L. (2017). Hybrid Rocket Studies Using HTPB/Paraffin Fuel Blends in Gaseous Oxygen Flow, 13 pages.

Toson, E., & Karabeyoglu, A. (2015). Design and Optimization of Hybrid Propulsion Systems for In-Space Application.

van Rossum, J. J. (1959). Experimental Investigation of Horizontal Liquid Films. *Chem. Eng. Sci.,* 11, 35.

Wang, Z., Lin, X., Li, F., & Yu, X. (2020). Combustion performance of a novel hybrid rocket fuel grain with a nested helical structure. *Aerospace Science and Technology*, *97*, 105613.

Weinstein, A., & Gany, A. (2011). Investigation of paraffin-based fuels in hybrid combustors. *International Journal of Energetic Materials and Chemical Propulsion*, *10*, 277–296.

Whitmore, S., Inkley, N. R., Merkley, D. P., & Judson, M. I. (2015). Development of a Power-Efficient, Restart-Capable Arc Ignitor for Hybrid Rockets. *Journal of Propulsion and Power*, *31*(6), 1739–1749.

Whitmore, S., & Merkley, S. (2019). Radiation Heating Effects on Oxidizer-to-Fuel Ratio of Additively Manufactured Hybrid Rocket Fuels. *Journal of Propulsion and Power*, *35*(4), 863–878.

Whitmore, S., Peterson, Z. W., & Eilers, S. D. (2013). Comparing Hydroxyl Terminated Polybutadiene and Acrylonitrile Butadiene Styrene as Hybrid Rocket Fuels. *Journal of Propulsion and Power*, *29*, 582–592.

Whitmore, S. A., Walker, S. D., Merkley, D. P., & Sobbi, M. (2015). High Regression Rate Hybrid Rocket Fuel Grains with Helical Port Structures. *Journal of Propulsion and Power*, *31*(6), 1727–1738.

Wohlgemuth, M., Yufa, N., Hoffman, J., & Thomas, E. L. (2001). Triply Periodic Bicontinuous Cubic Microdomain Morphologies by Symmetries. *Macromolecules*, *34*(17), 6083–6089.

Wu, Y., Yu, X., Lin, X., Li, S., Wei, X., Zhu, C., & Wu, L. (2018). Experimental investigation of fuel composition and mix-enhancer effects on the performance of paraffin-based hybrid rocket motors. *Aerospace Science and Technology*, *82-83*, 620–627.

Zeleznik, F. J., & Gordon, S. D. (1968). Calculation of Complex Chemical Equilibria. *Industrial & Engineering Chemistry*, *60*, 27–57.

Zilliac, G., & Karabeyoglu, M. (2006). Hybrid Rocket Fuel Regression Rate Data and Modeling. *42nd AIAA/ASME/SAE/ASEE Joint Propulsion Conference &amp; Exhibit*.

Zilliac, G., Story, G. T., Karp, A. C., Jens, E. T., & Wittinghill, G. (2020). Combustion Efficiency in Single Port Hybrid Rocket Engines. *AIAA Propulsion and Energy 2020 Forum*.

Appendix A

Alicat Flow Meter Process Overview

The operating principles of these flow meters are based on accurate volumetric flow measurement. The volumetric flow rate is calculated by putting a pressure drop over a particular internal restriction called a Laminar Flow Element (LFE) and measuring the difference in pressure across it. The limitation is meant to cause gas molecules to proceed in parallel routes over the entire length of the tube, resulting in laminar (streamline) flow throughout the device's operating range. Unlike other flow metres, the connection between pressure drop and flow in laminar flow metres is linear. The Poiseuille Equation is the underlying principle of operation for these flow meters represented in Equation 3.7.

$$Q = \frac{(P_1 - P_2)\pi r^4}{8\eta L} \tag{A.1}$$

Because π, r, and L are all constants, Equation 1 can be rewritten as follows:

$$Q = K(\frac{\Delta P}{\eta}) \tag{A.2}$$

K is a constant factor dictated by the restriction's geometry. In a simplified version, Equation 2 depicts the linear relationship between volumetric flow rate, Q, differential pressure, ΔP, and absolute viscosity, η.

The gas being measured must be selected in order to obtain an accurate volumetric flow rate (see Gas Select Mode, Appendix C). This is significant because the flow rate is calculated using the viscosity of the gas at the measured temperature. If the gas being measured is not the one chosen, an incorrect value for the viscosity of the gas will be utilised in the flow calculation, and the resulting output will be inaccurate in direct proportion to the viscosity difference between the two gases.

The viscosity of the gas, and consequently its composition, can significantly impact the meter's accuracy. Water vapour, odorant additives, and other factors that affect gas viscosity will directly affect accuracy. Because natural gas contains small and varying amounts of other gases such as butane and propane, which result in a viscosity that is somewhat different from pure methane, selecting methane and measuring natural gas, for example, will yield a fairly decent reading. However, it is not highly accurate (errors are typically 0.6 per cent). Because absolute viscosity fluctuates very little with pressure (within these meters' operational limits), a genuine volumetric value does not require a pressure correction. The viscosity of a gas is affected by its temperature. As a result, the flow meter makes internal adjustments to compensate for the change.

Appendix B

Paraffin Wax Fuel Grain Manufacture Work Instructions

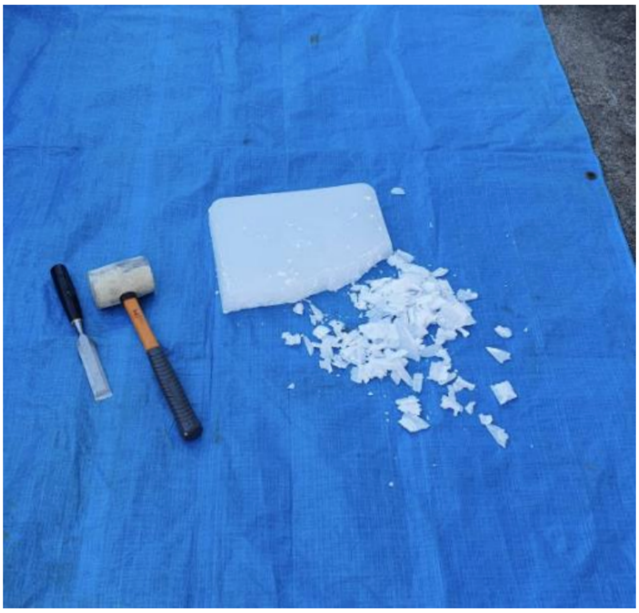

Figure B.1: Image taken of the break-down of paraffin wax slabs in process to achieve smaller more easier to melt portions of wax.

The following will present the procedure for the casting paraffin wax into the pure paraffin ABS shells and for the ABS gyroid fuel grains. The process should follow the appropriate SWI attached to risk 29347, especially when regarding the required safety measures. The paraffin wax used in this study was KunLun fully refined paraffin wax 58/60.

The ABS fuel grain shells were first treated for defects as part of the casting process. If any outside surface faults were discovered, they were fixed with wood glue (which behaves similarly to grain filler in this situation) or something similar. Because the condition of the inner fuel grain port is difficult to assess and molten paraffin may leak into the port, both ends must be sealed to prevent a severe leak. Vacuum bag sealant tape, sometimes known as ’tacky tape,’ is used to do this. Tacky tape is made to

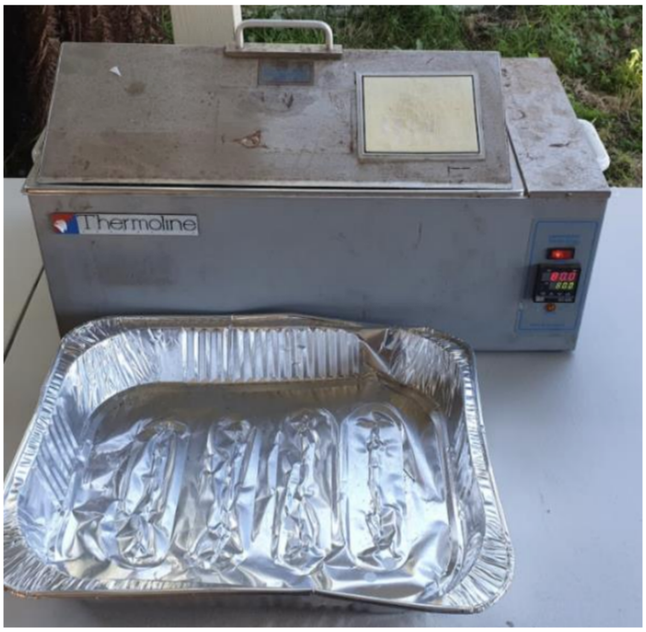

Figure B.2: Water bath preheating stage. The equipment is started prior to use up to 80 degrees Celsius. An important note is to ensure the lid remains enclosed to speed up the rate of heating.

stick to plastics and has excellent adhesive properties at high temperatures.

It's critical to set up the workplace properly before casting the paraffin. This was done outside in a well-ventilated place. This entails erecting two trestle tables with four independent stations: preparation, paraffin melting, paraffin immersion in water, and grain shell filling. The paraffin was obtained in large slabs, and because of this, it was critical to break it down into smaller fragments that could be melted quickly. To avoid over-spill of the wax (which could pose a significant tripping hazard, this is to be done in a separate location and on a tarp (see figure B.1).

The digital water bath was then filled and preheating phase commenced. Because of the large heat capacity of water, preheating the water to 80 degrees is expected to take a considerable amount of time - throughout this study, it took on average 60 mins to reach the set temperature. After preheat, the ABS shells were preheated in an incubator. Wearing suitable PPE and having a fire extinguisher nearby are other important pre-start considerations for this technique.

Overflow jigs were then connected to the grains to account for the substantial volumetric shrinkage of paraffin as it solidifies, allowing them to be overfilled by 25% of their volume (see figure B.3). As long as the grain is adequately sealed, these jigs can be 3D printed (simple pliable cardboard was also effective when wrapped around the top of the grain).

After 1.5-2 litres of paraffin had melted completely, it was placed in a water bath for, on average, 10 minutes to reach its temperature. To prevent water vapour from entering the molten wax, this was done without the lid on (see Figure B.4). The preheated shell was placed first in an insulating chamber, then atop the heat tiles. To accommodate for longer fuel grains, a stand is used to keep the grain from falling over. As seen in Figure B.5, a cardboard box was used to achieve this.

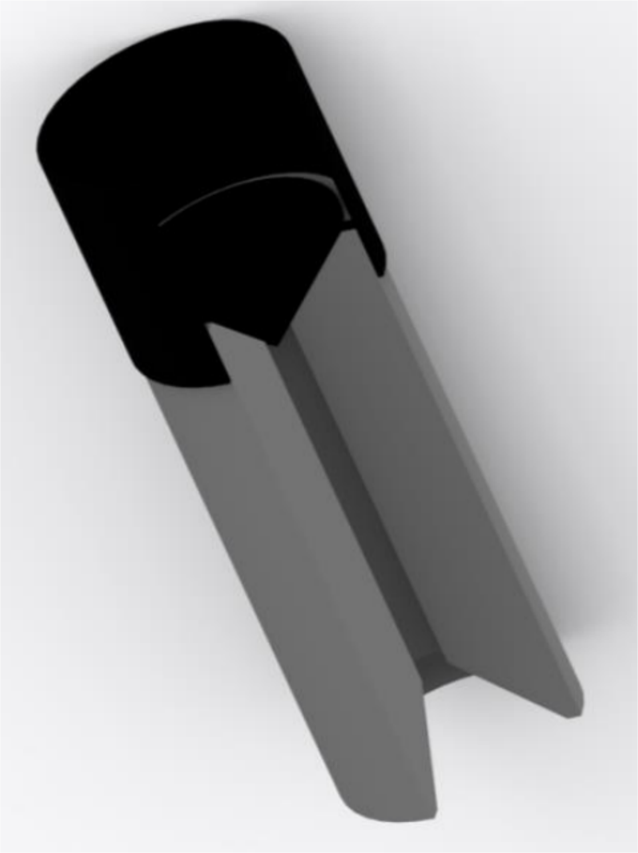

Figure B.3: CAD render of the overflow jig used to accommodate paraffin settlement and shrinkage during the casting and cooling process respectively.

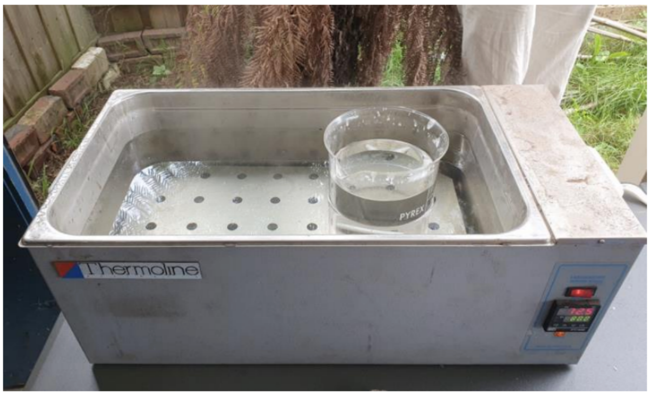

Figure B.4: Image of the paraffin wax heating process. The step utilised the water bath to reach the set temperature needed to melt paraffin. Depicted is the paraffin in its molten state.

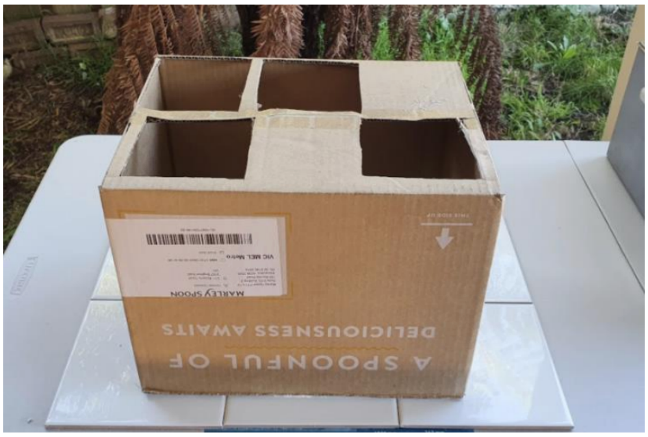

Figure B.5: The cardboard box provides a barrier to shield the fuel grains from the surrounding elements as they cool. The slots on the top of the box is used to help keep the fuel grains standing vertical as they cool.

The molten paraffin was then poured into the overflow jig until it was almost full. After that, the grains were allowed over 24 hours. Any remaining paraffin was either allowed to cool in the beakers or stored in a container lined with baking paper for future use. Insulation chambers were formed from cardboard tube that fit snugly around the fuel grain, then covered with adhesive insulating foam and wrapped in glass fibre blankets.

Appendix C

Fuel Grain Manufacture Data Tables

Fuel	Mass Flux (g/cm^2s)	$m_{initial}$ (g)	m_{final} (g)	$\dot{m}_{fuel}$ (g/s)
Paraffin Wax	7.7	818.4	752.8	6.5
Paraffin Wax	7.7	816.7	749.7	6.6
Paraffin Wax	10.7	837.5	772.8	6.4
Paraffin Wax	10.7	840.0	774.4	6.5
Paraffin Wax	15.3	813.9	747.4	6.6
Paraffin Wax	15.3	811.4	748.5	6.2
ABS	7.7	1049.1	1015.7	3.3
ABS	7.7	1047.0	1012.6	3.4
ABS	10.7	1044.1	1019.4	2.4
ABS	10.7	1042.0	1017.3	2.4
ABS	15.3	1042.7	1016.5	2.6
ABS	15.3	1041.6	1017.5	2.4
Gyroid ABS-Paraffin	7.7	860.5	827.0	3.3
Gyroid ABS-Paraffin	7.7	857.9	825.3	3.2
Gyroid ABS-Paraffin	10.7	865.9	827.0	3.8
Gyroid ABS-Paraffin	10.7	867.6	827.9	3.9
Gyroid ABS-Paraffin	15.3	865.3	794.1	7.1
Gyroid ABS-Paraffin	15.3	866.1	791.7	7.4

Table C.1: Complete register of initial and final mass and fuel mass flow rate data for all tested experimental campaign fuel grains.